Control of multiphoton processes by parametrically shaped ultrashort laser pulses

Dissertation

zur Erlangung des Grades eines
Doktors der Physik

am
Fachbereich Physik
der
Freien Universität Berlin

vorgelegt von
Alexander Patas

Berlin 2016

Erstgutachter: **Prof. Dr. Ludger Wöste**

Zweitgutachter: **Prof. Dr. Karsten Heyne**

Tag der Disputation: **28. Juni 2017**

Contents

Abbreviations

BCH Baker-Campbell-Hausdorff, page 32

CPA Chirped pulse amplification, page 38

CW Continuous wave, page 10

EA Evolutionary algorithm, page 35

FFT Fast Fourier transform, page 33

FROG Frequency resolved optical gating, page 48

FWHM Full width at half maximum, page 11

GD Group delay, page 17

GDD Group delay dispersion, page 8

GO Genetic optimization, page 35

GVD Group velocity dispersion, page 8

HCF Hollow-Core-Fibre, page 34

IP Ionisation potential, page 21

LC Liquid crystal, page 12

OPA Optical parametric amplifier, page 62

OPO Optical parametric oscillator, page 62

PCF Photonic crystal fibres, page 34

PRISM Phase resolved interferometric spectral modulation, page 35

SLM Spatial light modulator, page 12

SPM Self-phase modulation, page 27

SVAE Slowly varying envelope approximation, page 24

TG Transient grating, page 48

TL Transform-limited, page 48

TOD Third-order dispersion, page 17

TPA Two-photon absorbance, page 62

Abstract

This thesis aims to explore the prospects of parametric pulse shaping in multiphoton excitation and laser beam filamentation. Multiple challenges have to be overcome in order to introduce findings of this field of research into applications in medicine or biological imaging. First, experiments will be conducted in which different parametrically phase and polarization shaped laser pulses are tested on their effectiveness for selective excitation of two two-photon fluorophores. Two dyes are mixed in one solution and excited after propagation of the shaped pulses through a hollow-core photonic crystal fibre. Using experiments and simulations, an overview of the limits of this approach is presented as solutions to this problem are subject to a pareto-optimability where achieved contrasts have to be matched against a reduced overall fluorescence intensity.

In addition to a hollow-core fibre, pulses were also transmitted via a recently developed Kagomé fibre which will be beneficial for future high intensity applications. Two perpendicular shaped laser pulses, each optimized for fluorescence of one dye in a combined solution were created and send through this fibre. Anisotropy of the dyes allows for the measurement of a contrast in each polarization direction after the cuvette. This confirms that low dispersion and birefringence enable applications where polarization and phase shaped pulses after propagation through a Kagomé fibre are used in multiphoton fluorescence experiments.

Three-photon excitation in water was demonstrated for the amino acid L-Tryptophan. It was found that phase shaping can be used in a three-photon excitation scheme, although high pulse intensities are seen to result in strong spectral modulations after propagation through the cuvette. For intensities at which three-photon excitation is efficient, nonlinearities will most likely occur during focussing. Evaluation of the nonlinear Schrödinger equation will show that the laser spectrum up to the focus is mainly influenced by self-phase modulation. This spectral change significantly alters the three-photon field which in turn determines the interaction of the shaped pulse with the fluorophore. It will be pointed out how this pulse-shape dependent effect can be used to enhance selectivity in a three-photon excitation experiment by a correct choice of shaped pulses. Tryptophan was used as a model system to demonstrate how autofluorescence of biological tissue is susceptible to this experimental approach.

Further studies strive to understand whether pulse shaping can be used to enhance supercontinuum generation by filamentation in atomic gases. A white-light shaped laser source is used to study the influence of pulse shapes on the laser spectrum after filamentation in Argon and Krypton. Pulses are precompensated using a new approach, such that pulse shaping at the onset of the filament becomes possible. Although nonlinear effects like self-phase modulation and self-steepening are inherently important for the filamentation process, spectral changes due to plasma interaction are found to dominate spectral modulations after filamentation. To further understand this process, a two-dimensional cylindrical variation of the split-step Fourier method is derived and implemented. Nonlinear effects, dispersion, refraction, energy loss by ionisation and plasma defocussing are included in the simulation which results in very good agreement with the experimental findings. It is found that features which predominantly depend on the temporal shape of the laser pulse at the focus can be easily controlled by antisymmetric phase functions that were already applied to selective multiphoton ionisation, although through a distinctly different mechanism. Simulations seem to confirm that the temporal phase acquired due to interaction with the plasma is the main factor determining spectral modulations after the filament. Evolutionary optimizations are used to find more complex shaped pulses that give rise to a series of desired spectral features. These optimizations, which use a newly developed method of parameter-wise mutational parameters, are found to converge towards pulse shapes which tightly match the criteria set by the fitness functions. Results found in this last chapter demonstrate that knowledge of the pulse shape at the onset of a filament is essential for optimal supercontinuum generation via filamentation.

Kurzfassung

2

Das Ziel dieser Arbeit besteht darin, Möglichkeiten der parametrischen Pulsformung, mit besonderem Blick auf die Multiphotonen-Fluoreszenzanregung und Filamentation, durch Laserpulse aufzuzeigen. Zudem werden Verfahren vorgestellt, die für die Anwendung von Pulsformung in medizinischer und biologischer Bildgebung von Vorteil sind.

Hierfür wurden zunächst verschiedene parametrische Phasenfunktionen daraufhin untersucht, ob sie zwei Farbstoffe selektiv, nach Transmission durch eine Hohlkernfaser, zweiphotonisch anregen können. Dies bestätigt, dass geformte Laserpulse für selektive Anregung von Farbstoffen, z.b. in endoskopischen Anwendungen, verwendet werden können. Parametrische Phasenfunktionen werden vorgestellt, die eine Kontrolle der Multiphotonen-Anregung durch Veränderung nur eines Parameters ermöglichen. Simulationen wurden durchgeführt um die Grenzen der Kontrolle des Zweiphotonen-Prozesses aufzuzeigen. Dabei wurde deutlich, dass geformte Pulse, die größere Kontraste zwischen den Fluorsezenzfarbstoffen erreichen, immer mit einer reduzierten Fluoreszenz-Intensität einhergehen.

Zusätzlich zu der Hohlkernfaser wurde eine neuartige Kagomé-Faser untersucht, welche besonders geeignet ist Pulse hoher Intensität ohne den störenden Einfluss von nichtlinearen Effekten zu leiten. Selbst polarisationsgeformte Pulse finden in solch einem Szenario Anwendung. Es wurde gezeigt, dass ein polarisationsgeformter Doppelpuls, nach Transmission durch eine Kagomé-Faser, verwendet werden kann um anistrop fluoreszierende Farbstoffe polarisationsabhängig anzuregen. Hierfür wurden zwei senkrechte phasengeformte Laserpulse erzeugt, die je für die Fluoreszenz eines Farbstoffes optimiert sind. Je nach Orientierung eines Polarisationsfilters ließ sich somit zwischen stärkerer Fluoreszenz des einen oder anderen Farbstoffes wählen.

Weiterhin wurde die Kontrolle der Dreiphotonen-Anregung anhand von der Aminosäure L-Tryptophan in Wasser demonstriert. Auch dieser Prozess kann durch geformte Pulse beeinflusst werden, jedoch zeigt sich schnell, dass bei den hierfür benötigten Intensitäten nichtlineare Effekte einen signifikanten Einfluss auf die Entwicklung des Spektrums in der Küvette haben. Simulationen der Puls-Propagation in der Küvette, welche die Intensitätsentwicklung im Gauß-Fokus berücksichtigen, gaben Aufschluss auf die, hauptsächlich durch Selbstphasenmodulation bestimmten, spektralen Veränderungen. Das sich damit ebenfalls verändernde Dreiphotonen-Spektrum konnte durch Wahl der Pulsform so verändert werden, dass der Kontrast zwischen zwei Farbstoffen noch weiter verbessert werden kann.

In einer dritten Reihe an Experimenten wurde untersucht inwieweit parametrisch geformte Pulse Einfluss auf das Weißlichtspektrum nach einem Filament haben. Pulse wurden mit einer neuartigen Methode zur Phasenbestimmung so vorkompensiert, dass sie zu Beginn des Filaments eine gewünschte Pulsform erreichten. Zweidimensionale, zylindrische Simulationen der Puls-Propagation unter Berücksichtigung von nichtlinearen Effekten, Dispersion, Plasma-Wechselwirkung und Beugung zeigten, dass Selbstphasenmodulation und Selbstaufsteilung zwar essentiell für das Auftreten eines Filaments notwendig sind, die Veränderung des Spektrums aber maßgeblich von der Wechselwirkung des Laserpulses mit dem Plasma und damit durch die Pulsform während des Filaments bestimmt wird. Simulation und Experiment zeigten eine starke Übereinstimmung, was bestätigte, dass die Pulspropagation im Filament maßgeblich durch die im Modell berücksichtigten Faktoren bestimmt ist. Der Einsatz von parametrischen Phasenfunktionen, wie sie bereits zur selektiven Anregung von Mehrphotonenübergängen verwendet wurden, ermöglicht im Experiment bereits eine Kontrolle über das Spektrum nach dem Filament. Evolutionäre Optimierungen werden verwendet um optimale Pulse zu finden, die eine Reihe an komplexen spektralen Features optimieren. Hierfür wurde eine neue Methode zur parameterabhängigen Anpassung des Mutationsparameters verwendet. Die in dieser Arbeit präsentierten Ergebnisse veranschaulichen das Potential parametrischer Pulsformung im Bereich der Laserfilamentation und Mehrphotonen-Fluoreszenzanregung.

Introduction 3

In 1999 Ahmed Zewail (*1946, †2016) was awarded the Nobel Price in chemistry for his achievements in the field of femtochemisty. In his area of research, ultrashort laser pulses, which can be as short as a couple of femtoseconds ($1\,\mathrm{fs} = 10^{-15}\,\mathrm{s}$), are used to study chemical reactions at timescales where the movement of atoms in a molecule becomes relevant. It was at this time, that scientists developed the dream of controlling chemical reactions with the help of coherent light. Different measurement schemes were proposed [1, 2] in which interference between multiple excitation pathways in an electronic system are utilized to influence results of an ionisation or dissociation reaction. As a first experimental implementation of these schemes pump probe experiments were conducted. Here, a first laser pulse is used to prepare a superposition of vibrational states of a quantum system. Then, a second pulse probes the propagated system after an adjustable delay. With the advent of computer-programmable liquid crystal arrays far more complex pulse shaping became viable. Multi-element spatial light modulators were used by Weiner et al. in 1990 to change the spectral phase of a laser pulse [3, 4]. Shortly after, methods for finding optimal pulse shapes for excitation of specific electronic molecular states were proposed by Rabitz et al. in 1992. These involved optimization of the phase delays generated by a spatial light modulator in a computer controlled closed loop experiment. Here, evolutionary strategies were employed to find parameter-sets that can outperform a short (transform-limited) laser pulse [5] in certain experiments. These feedback-optimized phase shaped pulses were shown to be able to steer dissociation reactions [6] or selectively ionise isotopes [7] and thereby came closer to achieving the goal of controlling chemical reactions with phase shaped laser pulses. In 1999, Doron Meshulach and Yaron Silberberg proposed an additional control scheme which would lead to some control over arbitrary multiphoton transitions [8]. They stated that multiphoton transitions can be seen as the result of interference of a continuum of excitation pathways involving one or more virtual levels in between an initial and a final state. They proposed that phase shaped pulses should be able to influence which excitation pathways constructively or destructively interferes. Meshulach and Silberberg demonstrated this in an experiment on atomic Caesium where a phase shaped pulse was tuned such that it would not excite a narrow two-photon transition when compared with an unshaped pulse.

While evolutionary optimizations were very successful in finding optimized pulses, it was difficult to interpret the obtained results. In the long term it was seen as desireable to use parametric pulse shaping rather than high-dimensional, time-consuming optimizations to steer and control quantum systems.

Recent developments in the area of pulse shaping hint to a series of applications in microscopy, endoscopic procedures and even photodynamic therapy. For these applications to emerge, it is essential that the problem of finding a matching pulse shape is reduced to tuning a set or a single relevant parameter. Furthermore, shaped pulses have to be delivered to a required place without being distorted by linear and non-linear effects. Here, hollow-core photonic crystal fibres pose as one way of pulse delivery for most medical applications.

Most of these developments became possible due to the availability of ultrashort laser systems. With the help of Ti:Sa crystals as a gain medium and chirped pulse amplification, previously unrivalled laser intensities could be reached. At these intensities a beam can, even at ambient pressure, experience self-focussing due to nonlinear effects. Self-focussing leads, above a critical power, to a beam collapse and subsequent ionisation of the propagation medium. This process is

called filamentation and can, after some fine tuning be used as a broadband whitelight laser source. It was demonstrated that filaments can occur over the length of some km when plasma defocussing and self-focussing are well balanced [9].

This thesis will explore which parametric phase functions can selectively excite two-photon fluorophores after transmission through a hollow core photonic crystal fibre. For that, a range of parametric phase-functions will be tested on their usefulness in such an approach and parameters will be named which allow for easy control over the selective excitation of two fluorophores. It will be demonstrated that hollow-core fibres can be used in such a setup if linear dispersion is accounted for. In a second set of experiments the effect of nonlinear propagation of pulses destined for three-photon excitation of L-Tryptophan will be studied. Simulations are performed that shed light on the nonlinear spectral modulation which will occur in a focus at these intensities. It will be analysed whether pulse shapes can be used to exploit nonlinear self-phase modulation for increased selectivity when dyes are excited in a cuvette filled with water. Tryptophan will be used as an example that demonstrates autofluorescence of biological tissue will be applicable to this method. In further experiments, the influence of shaped laser pulses on the broadening of a spectrum after a filamentation in high pressure Argon and Krypton will be studied. Simulations will help to point out the mechanism involved when spectral changes occur due to changes in pulse shapes during filamentation. The development of algorithms for enhanced convergence of evolutionary optimizations and for the propagation of ultrashort laser pulses in nonlinear ionising media represent a significant part of this thesis. A separate chapter will be committed towards these methods. As this thesis examines a series of slightly different applications of laser pulse shaping, each chapter will offer a separate introduction recapitulating what was achieved in that concerning field of research.

Theoretical Principles 4

This chapter will briefly introduce a series of theoretical concepts required in this thesis. First the mathematical description of the electromagnetic field will be introduced. Essential concepts for pulse generation as well as the equations governing pulse shaping will be discussed. The interaction of light with optical media, fluorescent molecules and ionizable gases is essential to understand the presented experimental results and will therefore be studied in greater detail. Finally, a short section will be explaining simulation and optimization algorithms used in the course of this thesis.

4.1 Mathematical Description of Ultrashort Laser Pulses

Laser pulses can be fully characterized by their spatial and temporal electrical field. In this chapter, for each polarization a complex electrical field will be defined as it will be particularly beneficial when describing the propagation of laser pulses in optical media later on.

4.1.1 Complex Electrical Field Description

The electrical field of a polarized laser pulse can be written as

$$\mathbf{E}(x,y,z,t) = \begin{pmatrix} E_{\parallel}(x,y,z,t) \\ E_{\perp}(x,y,z,t) \end{pmatrix}, \tag{4.1.1}$$

In order to derive the complex electrical field description in the temporal and spectral domain, for now, the polarization as well as spatial dependence of the electrical field will be neglected, i.e., $\mathbf{E}(x,y,z,t) = E(t)$. Following the description in [10], a spectral field strength is introduced:

$$\tilde{E}(\Omega) = \mathcal{F}\{E(t)\}. \tag{4.1.2}$$

Since $E(t)$ is a real function, one finds that $\tilde{E}(\Omega) = \tilde{E}(-\Omega)$. This is slightly impractical since negative frequencies are undefined. Additionally a complex representation of the electrical field in the time domain would be useful. Hence, a complex electrical field is defined as the Fourier transformation over only the positive frequencies of the spectral field strength:

$$\tilde{E}^{+}(t) = \frac{1}{2\pi}\int_{0}^{\infty} \tilde{E}(\Omega) e^{i\Omega t} d\Omega \tag{4.1.3}$$

For convenience one can use:

$$\tilde{E}^{+}(\Omega) = \begin{cases} \tilde{E}(\Omega) & \text{for} \quad \Omega \geq 0 \\ 0 & \text{for} \quad \Omega < 0 \end{cases} \tag{4.1.4}$$

The relationship between $\tilde{E}^{+}(t)$ and $\tilde{E}^{+}(\Omega)$ is then given by a simple fourier transform:

$$\tilde{E}^{+}(t) = \mathcal{F}\{\tilde{E}^{+}(\Omega)\} = \frac{1}{2\pi}\int_{-\infty}^{\infty} \tilde{E}^{+}(\Omega) e^{i\Omega t} d\Omega \tag{4.1.5}$$

a_0		carrier envelope phase
a_1	linear phase	frequency shift of the spectrum
a_2	linear chirp	broadening of the pulse
b_0		carrier envelope phase
b_1	linear phase	temporal shift of the pulse
b_2	linear chirp	broadening of the pulse
b_3	quadratic chirp	asymmetric broadening of the pulse

Table 4.1: List of the most important spectral-phase taylor coefficients and their influence on the laser pulse.

and

$$\tilde{E}^+(\Omega) = \mathcal{F}^{-1}\{\tilde{E}^+(t)\} = \int_{-\infty}^{\infty} \tilde{E}^+(t) e^{i\Omega t} dt. \tag{4.1.6}$$

In most cases the complex electrical field is rapidly oscillating around a so called carrier frequency ω_l. This suggests that it is reasonable to split the complex electrical field into an amplitude $\mathcal{E}(t)$ and phase $\varphi_0 + \varphi(t) + \omega_l t$, seperating the slowly varying temporal phase $\varphi(t)$ from the fast oscillating term $\omega_l t$:

$$\tilde{E}^+(t) = \frac{1}{2}\mathcal{E}(t) e^{i\varphi_0} e^{i\varphi(t)} e^{i\omega_l t}. \tag{4.1.7}$$

Here, $\mathcal{E}(t)$ is the real electrical field envelope and φ_0 the carrier envelope phase. Another important quantity is the instantaneous frequency, which equals the derivative of the temporal phase, i.e.,

$$\omega_t = \partial\varphi(t)/\partial t + \omega_l. \tag{4.1.8}$$

Usually the temporal and spectral phase are expanded into a taylor series. This helps to understand the effect of different kind of phase functions on a laser pulse.

$$\varphi(\omega) = b_0 + b_1(\omega - \omega_0) + \frac{b_2}{2}(\omega - \omega_0)^2 + \frac{b_3}{6}(\omega - \omega_0)^3 + ..., \tag{4.1.9}$$

$$\varphi(t) = a_0 + a_1(t - t_0) + \frac{a_2}{2}(t - t_0)^2 + \frac{a_3}{6}(t - t_0)^3 + ..., \tag{4.1.10}$$

with $b_i = \partial^i\varphi(\omega)/\partial\omega^i|_{\omega_0}$ and $a_i = \partial^i\varphi(t)/\partial t^i|_{t_0}$. This is especially beneficial because material properties are given in the quantities of the group delay dispersion (GDD) and group velocity dispersion (GVD) which translate into changes of the coefficients of the spectral phase's taylor series. GDD and GVD will be explained in more detail later on. Tab. 4.1 lists the most relevant coefficients of the temporal and spectral taylor series used to described the effect of a phase function on a laser pulse. For very broadband spectra, that are used in parts of this thesis, higher order terms will become relevant. It is noteworthy that even coefficients of both, temporal and spectral taylor series, have an equal effect on the pulse.

4.1.2 Jones Formalism

Although we neglected polarization states in the preceding chapter, it is an essential concept when discussing pulse shaping methods. We will use the widely adapted Jones-formalism to mathematically describe the effects of polarizing optics on a laser beam.
The electrical field vector can be seen as sum of two orthogonal electrical fields:

$$\mathbf{E} = E_\perp \mathbf{e}_\parallel + E_\perp \mathbf{e}_\parallel, \tag{4.1.11}$$

$\begin{pmatrix}1\\0\end{pmatrix}$	linear polarized
$\frac{1}{\sqrt{2}}\begin{pmatrix}1\\1\end{pmatrix}$	linear polarized rotated $45°$
$\frac{1}{\sqrt{2}}\begin{pmatrix}1\\i\end{pmatrix}$	circular polarized (clockwise)
$\frac{1}{\sqrt{2}}\begin{pmatrix}1\\-i\end{pmatrix}$	circular polarized (counter-clockwise)

Table 4.2: Normalized Jones vectors for the most important polarization states

with

$$E_{\parallel} = E_{0\perp} e^{i(\mathbf{k}_z z - \omega t + \varphi_{\perp})} \tag{4.1.12}$$

and

$$E_{\perp} = E_{0\parallel} e^{i(\mathbf{k}_z z - \omega t + \varphi_{\parallel})}. \tag{4.1.13}$$

This notation becomes especially simple when rewriting Eq. 4.1.11.

$$\mathbf{E} = \begin{pmatrix} E_{0\parallel} e^{i\varphi_{\parallel}} \\ E_{0\perp} e^{i\varphi_{\perp}} \end{pmatrix} e^{i(k_z z - \omega t)} \tag{4.1.14}$$

The vector in eq. 4.1.14 is called Jones vector [11]. In Tab. 4.2 the most common normalized Jones vectors are listed. From here on, it is pretty easy to describe the influence of an arbitrary optical device on the polarization of a laser beam with the help of Jones matrices.

$$\mathbf{J_{out}} = \mathbf{M} \cdot \mathbf{J_{in}} = ... \, \mathbf{M_3} \cdot \mathbf{M_2} \cdot \mathbf{M_1} \cdot \mathbf{J_{in}} \tag{4.1.15}$$

Jones matrices can be combined by multiplication to characterise complex optical devices. The most important Jones-matrices stand for the influence of a polarizer:

$$\mathbf{POL}_{\parallel} = \begin{pmatrix} 1 & 0 \\ 0 & 0 \end{pmatrix}, \tag{4.1.16}$$

a retardance plate:

$$\mathbf{RET}(\varphi) = \begin{pmatrix} e^{i\varphi/2} & 0 \\ 0 & e^{-i\varphi/2} \end{pmatrix}, \tag{4.1.17}$$

and a rotation:

$$\mathbf{D}(\Theta) = \begin{pmatrix} \cos(\Theta) & -\sin(\Theta) \\ \sin(\Theta) & \cos(\Theta) \end{pmatrix} \tag{4.1.18}$$

on the Jones vector. By combining these three, every polarizing optical component can be modelled.

4.2 Generation of Ultrashort Laser Pulses

The generation of ultrashort laser pulses is based on interference of a broad spectrum of electromagnetic waves. Ultrashort laser pulses are commonly generated in an oscillator which is a special laser with a broadband laser medium, dispersion management and an intensity dependent gain which allows for mode locking. In modern femtosecond oscillators a Titan doped sapphire

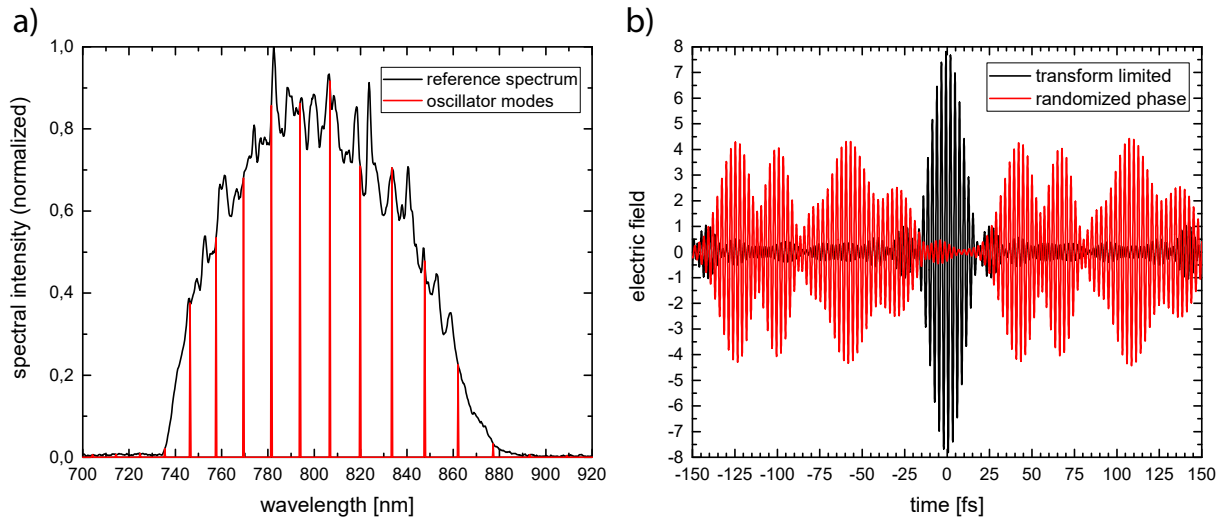

Figure 4.1: Example for laser modes (a) and the resulting interference (b). If the phase dependence is random no clear maxima can be seen (red). (black) shows a transform-limited pulse for which all modes are phase-locked.

crystal (Ti:Sa) is used because of its broadband emission spectrum. This kind of laser was invented by P.F. Moulton in 1982 [12] A laser cavity of length L can sustain longitudinal modes satisfying the equation

$$\frac{m\lambda_m}{2} = \sum_i n_i(\lambda_m)L_i, \tag{4.2.1}$$

or as for the frequencies

$$\nu_m = \frac{mc}{2\sum_i n_i(\nu_m)L_i}. \tag{4.2.2}$$

M is an integer which is called the mode number and n_i is the refractive index of each partial length inside the cavity L_i. $\sum_i n_i(\nu)L_i$ can be substituted with $n(\nu)L$ when assuming L as an effective length of the cavity. From Eq. 4.2.2 the distance of two modes can now be calculated:

$$\delta_\nu = \nu_{m+1} - \nu_m = \frac{c}{2n(\nu_m)L}. \tag{4.2.3}$$

This quantity is also known as the repetition rate of the oscillator f_{rep} which is typically in the order of 50 to $80\,MHz$.

Fig 4.1 (a - red) illustrates how the allowed modes of a very short cavity would look like. Interference of these modes would lead to an electrical field seen in Fig 4.1 (b - red). If all modes are phase locked and their oscillations are constructively interfering at $t = 0$ we receive a transform-limited (TL) pulse (Fig. 4.1 (b - black)).

4.2.1 Mode-Locking

In a laser cavity all allowed modes (see Eq. 4.2.2) compete. Modes with the best gain vs loss ratio will over time use all energy stored in the lasing medium. In this regime an oscillator becomes a classic continuous wave (cw) laser source. In order to move to the pulsed regime, as stated before, the phases of the cavity modes have to be locked. This is achieved by reducing the gain in the low intensity regime, for which it is common to use either active or passive mode-locking. Active mode-locking uses electro- or acoustooptics to introduce losses to the cw-cavity and thereby

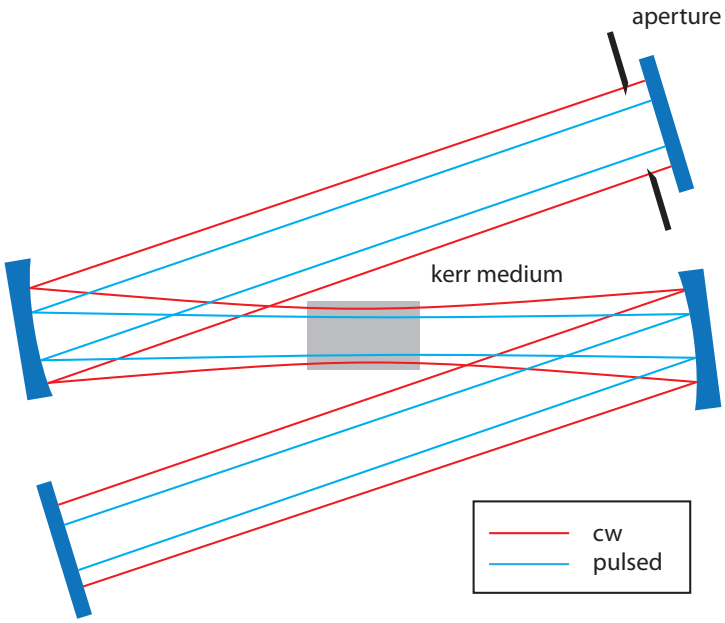

Figure 4.2: Illustration of Kerr-lens mode-locking. Losses are introduced in the cw regime by closing an aperture. Image taken from [13].

discourage cw-lasing. These mechanisms are electronically controlled and therefore cannot result in pulses shorter than picoseconds on their own. Passive mode-locking, on the other hand, relies on a saturable absorber to change the gain of the laser cavity. One common type of saturable absorber exploits the Kerr-lens effect to reduce the gain in the cw regime. In this context it is sensible to introduce the nonlinear refractive index n_2. At high intensities the refractive index becomes intensity dependent:

$$n(I) = n_0 + n_2 I \tag{4.2.4}$$

These nonlinearities predominantly occur in the lasing medium, where the strongly focussed Gaussian beam profile induces a refractive index change which leads to self focussing of the beam. Fig. 4.2 illustrates the effect of this self-focussing on the pulsed regime. Using an aperture one can easily induce losses in the cw regime and thereby reach mode-locking. Another aspect of oscillator operation, which is not demonstrated in Fig. 4.2 is dispersion control. The air, as well as the lasing medium result in pulses being generated to disperse after a number of round-trips. This would again prevent mode-locking. Hence, chirped mirrors or a prism compressor are added to the cavity to account for all introduced dispersion. By tuning the compressor, one can choose at which peak intensity the dispersion of the cavity is compensated. This results in a change in spectral bandwidth corresponding to a different transform limited pulse length. It is important to note that, as an implication by the Fourier-dependence of time and frequency space, the time-bandwidth product has a lower limit:

$$\delta\omega_p \tau_p \geq 2\pi c_B \tag{4.2.5}$$

Here, ω_p is the spectral width and τ_p the pulse width, defined as a full width at half maximum (FWHM) . Limits for the time bandwidth product are dependant on the pulse shape and are listed in Tab. 4.3.

Gaussian pulse	$c_b = 0.441$	Lorentzian pulse	$c_b = 0.142$	sech^2 pulse	$c_b = 0.315$

Table 4.3: Values for the minimum of the time bandwidth product for the most common pulse shapes.

4.2.2 Chirped-Pulse Amplification

Chirped pulse amplification was first introduced in 1985 by D. Strickland and G. Mourou [14]. A seed pulse from the oscillator is stretched by a factor of $\approx$ 10000 [15], amplified and then recompressed using a second grating compressor. Stretching the pulse is necessary to keep intensities below the damage threshold of the Ti:Sa crystal. The lasing medium is usually pumped by a frequency-doubled YLF or Nd:Yag solid state laser. Both, multi-pass and regenerative amplifiers are operated at considerably lower repetition rates to allow for enough pumping of the lasing medium. Common repetition rates are (1-250) kHz resulting in pulse energies of around μJ to mJ

4.3 Laser Pulse Shaping

Laser pulse shaping in closed loop schemes has become the most crucial method in coherent control [16]. Pulse shaping using programmable liquid crystal (LC) arrays [4] was followed by different methods of pulse shaping. Either using acousto-optics [17], or micro-mirror arrays which also work in the UV regime [18]. Pulse shaping with programmable spatial light modulators (SLM), as applied in this thesis, takes place in the Fourier space. The laser beam is split in a 4-f zero dispersion line into its frequency components. First, the beam is dispersed by a grating. Each frequency component, still retaining the original beam shape, is then focused by a cylindrical mirror or lens into the Fourier plane. Since the distance of the focussing element to the grating is equal to the focal length, all wavelengths are parallelized in the process. A spatial light modulator, consisting of an array of liquid crystals, is placed in the centre of the setup. With this, each frequency can be changed in its phase before another focussing lens and grating recombine the beam. In recent years, this setup was extended so that using one [19] or more SLMs could be used to control more and more properties of the electrical field. Using a total of four liquid crystal arrays and a series of waveplates one can achieve full control over the laser pulse's properties including phase, amplitude, polarization orientation, and ellipticity [20, 21].

4.3.1 Phase- and Amplitude-Shaping

The classic setup in which phase and amplitude shaping is realized uses two liquid crystal arrays at $\pm 45^\circ$ to the incoming horizontal polarized light. While phase shaping could be accomplished by only one array, two arrays are required for full control over the phase and amplitude of the laser spectrum. Arrays A_a and A_b can be seen a simple wavelength-dependant retardation plates rotated to plus or minus 45°. The Jones matrices for both arrays become:

$$\begin{aligned} \mathbf{A}_a &= \mathbf{D}(-45^\circ)\mathbf{RET}(\varphi_a)\mathbf{D}(45^\circ) \\ &= e^{i\frac{\varphi_a}{2}} \begin{pmatrix} \cos(\frac{\varphi_a}{2}) & i\sin(\frac{\varphi_a}{2}) \\ i\sin(\frac{\varphi_a}{2}) & \cos(\frac{\varphi_a}{2}) \end{pmatrix} \end{aligned} \tag{4.3.1}$$

and

$$\mathbf{A}_b = \mathbf{D}(45^\circ)\mathbf{RET}(\varphi_a)\mathbf{D}(-45^\circ) = e^{i\frac{\varphi_b}{2}} \begin{pmatrix} \cos(\frac{\varphi_b}{2}) & -i\sin(\frac{\varphi_b}{2}) \\ -i\sin(\frac{\varphi_b}{2}) & \cos(\frac{\varphi_b}{2}) \end{pmatrix} \tag{4.3.2}$$

The combined Jones matrix describing the effect of both arrays is the result of a matrix multiplication. It is noteworthy that only the difference or sum of the phase terms φ_a, φ_b appears in this equation:

$$\mathbf{A}_a \cdot \mathbf{A}_b = e^{i\frac{\varphi_a+\varphi_b}{2}} \begin{pmatrix} \cos(\frac{\varphi_a-\varphi_b}{2}) & i\sin(\frac{\varphi_a-\varphi_b}{2}) \\ \sin(\frac{\varphi_a-\varphi_b}{2}) & \cos(\frac{\varphi_a-\varphi_b}{2}) \end{pmatrix}. \tag{4.3.3}$$

This can be understood as a variable transformation from φ_a and φ_b to $(\varphi_a - \varphi_b)$ and $(\varphi_a + \varphi_b)$. Together with a polariser, the effect on the incoming electrical field becomes:

$$\mathbf{E}_{out} = \mathbf{POL}_{\parallel} \cdot \mathbf{A}_a \cdot \mathbf{A}_b \cdot \mathbf{E}_{in} = e^{i\frac{\varphi_a+\varphi_b}{2}} \begin{pmatrix} \cos(\frac{\varphi_a-\varphi_b}{2}) & i\sin(\frac{\varphi_a-\varphi_b}{2}) \\ 0 & 0 \end{pmatrix} \mathbf{E}_{in} \tag{4.3.4}$$

$$\begin{aligned} E(\omega)_{\parallel,out} &= H(\omega)E(\omega)_{\parallel,in} \\ &= e^{i\frac{\varphi_{a,\omega}+\varphi_{b,\omega}}{2}} \cos(\frac{\varphi_{a,\omega}-\varphi_{b,\omega}}{2}) E(\omega)_{\parallel,in} \end{aligned} \tag{4.3.5}$$

Here $H(\omega)$ is called a transfer function.

$$H(\omega) = R(\omega)e^{i\Psi(\omega)} \tag{4.3.6}$$

made up of an (amplitude) transmission function $R(\omega)$ and phase change $\Psi(\omega)$ as seen by each frequency component ω.

Nyquist-Limit

Pixelated pulse shaping systems feature one inherent problem which has to be addressed. The retardance generated by each liquid crystal array can be given in the range of $[0 - 2\pi]$ based on the periodicity of the incoming wave. Let us assume a phase difference between two adjacent pixels φ_1 and φ_2 at frequencies ω_1 and ω_2. This difference $\delta\varphi$ is undefined by a summand of $n2\pi$.

$$\varphi_1 - \varphi_2 = n2\pi, \tag{4.3.7}$$

where n is a integer. This means that a linear phase, created by a pulse shaper will allow for different interpretations and thereby to multiple replica pulses shifted by $2\pi n/(\omega_2 - \omega_1)$ in time. While these pulses are of low intensity (especially for high n), it is still desirable to maximize the resolution of a setup to minimize problems introduced by the Nyquist limit. The Nyquist limit is defined as being reached when the phase difference of to neighbouring pixels surpasses π:

$$|\varphi_2 - \varphi_1| \geq \pi \tag{4.3.8}$$

At this limit both interpretations (an increasing or decreasing phase) are equal.

4.3.2 Polarization-Shaping

Polarization pulse shaping was found to be especially useful when selecting multiphoton ionisation pathways in small molecules. This was shown impressively by Brixner et al.[23]. Polarization shaping can be used to control the complete polarization ellipse which requires either interferometric [24, 25] methods or at least 4 liquid crystal arrays in succession [20]. Fig. 4.3 shows what kind of pulses can be created using parametric shaping techniques. In most experiments simple polarization control will suffice.

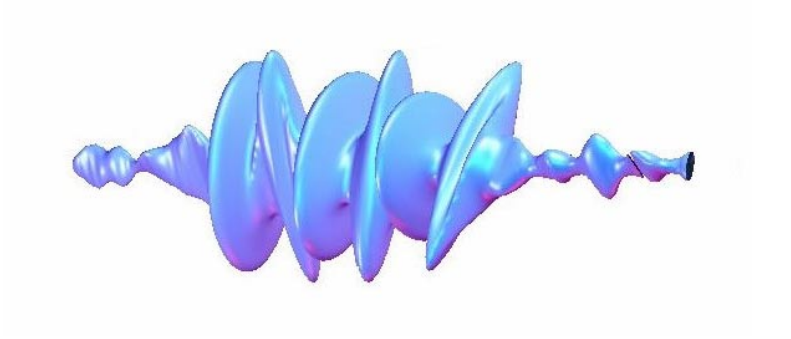

Figure 4.3: Example of a polarization shaped laser pulse generated with a setup described in [20]. Sub-pulses with alternating ellipticity and orientation are shown. This data originates from the work in [22].

In order to create two perpendicular polarized phase shaped laser pulses, only two arrays are required. A rotation by a half-waveplate, which is placed just after the two liquid crystals rotates the polarization of the beam by $45°$. The combined Jones matrix of both arrays then reads:

$$\mathbf{Ret}(\pi, 45°/2) \cdot \mathbf{A}_a \cdot \mathbf{A}_b = \frac{1}{\sqrt{2}} \begin{pmatrix} 1 & -1 \\ 1 & 1 \end{pmatrix} \frac{1}{2} \begin{pmatrix} e^{i\varphi_b} + e^{\varphi_a} & e^{i\varphi_b} - e^{\varphi_a} \\ e^{i\varphi_b} - e^{\varphi_a} & e^{i\varphi_b} + e^{\varphi_a} \end{pmatrix} \tag{4.3.9}$$

$$= \frac{1}{\sqrt{2}} \begin{pmatrix} e^{\varphi_a} & -e^{\varphi_a} \\ e^{i\varphi_b} & e^{i\varphi_b} \end{pmatrix} \tag{4.3.10}$$

For a parallel laser pulse this will result in:

$$\mathbf{Ret}(\pi, 45°/2) \cdot \mathbf{A}_a \cdot \mathbf{A}_b \cdot \mathbf{E}(\omega)_{\parallel} = \frac{1}{\sqrt{2}} E(\omega) \begin{pmatrix} e^{i\varphi_a} \\ e^{i\varphi_b} \end{pmatrix} \tag{4.3.11}$$

Using this setup, both polarization components can be phase-shaped independently using only two liquid crystal arrays in the Fourier plane. It is important to note, that without the waveplate phase shaping of both polarization components would be possible as well. This, unfortunately would lead to problems when the beam is recombined in the zero-dispersion compressor. Both gratings usually show a different reflectivity depending on the polarization of the light. Therefore, pulses which traverse a grating in a $\pm 45°$ angle, will be compressed in one axis. Those pulses would then seize to be orthogonal, which is circumvented with the aforementioned half-waveplate.

4.3.3 Methods for Parametric Pulse Shaping

Pulse shaping schemes allow to alter the phase, amplitude and polarization state of a incoming laser pulse. This control is achieved, as previously stated, by at least two liquid crystal arrays (for phase and amplitude shaping) which often consist of hundreds of liquid crystal cells. Since the width of the separate liquid crystal cells determines the spectral resolution and Nyquist limit it is desirable to apply SLM's with even more pixels. This provides one with the problem to address all these separate parameters. In many coherent control experiments genetic optimization algorithms are used to optimize all pixels separately but this approach is very time consuming and often does not lead to an insight into the physics present. One way of reducing the dimensionality is to find suitable parametrizations which can be used to directly change relevant pulse parameters. A first step was to extend the spectral phase into a Taylor series. The effects of the Taylor coefficients on the laser pulse were discussed in chapter 4.1.1. When sequences of separately shaped laser pulses with different intensities are required other concepts will have to be established.

Arbitrary pulse sequences

One method to achieve this full parametric control was developed by Weber et al. [26] and is based on the assembly of pulse sequences from separately shaped pulses in the time or frequency domain. Let us assume a series of separately shaped pulses based on a single input pulse:

$$E_i(\omega) = H_i(\omega)E_{in}(\omega) \tag{4.3.12}$$

Then, the transfer function for the complete pulse sequence is the sum of all single pulse transfer functions:

$$E_{out}(\omega) = H_{ges}(\omega)E_{in}(\omega) = H_1E_{in} + H_2E_{in} + ... = \sum_i H_i(\omega)E_{in}(\omega) \tag{4.3.13}$$

Here, the properties by each single pulse are defined by its transfer function $H_i(\omega)$. The time delay of the pulses with respect to the input pulse is therefore set by the linear phase term in the Taylor expansions of $\Psi(\omega)_i$. At this, point it has to be ensured that the full transfer function fulfils $|H_{ges}(\omega)| \leq 1$, because amplitude shaping can only be used to reduce the spectral intensity at a given wavelength. If this is not satisfied $|H_{ges}(\omega)|$ can either be clipped at a transmission of one or divided by the full transfer function's maximum. Latter would reduce the energy of the total pulse sequence which can be impractical in certain applications.

Fourier-Transform Iteration Method

In certain conditions the spectrum required for the generation of pulses is not available, or only phase shaping is available to create a desired pulse shape. Then, the aim of a pulse shaping method should be to find a spectral amplitude and phase function which will result in the closest resemblance with the desired pulse shape. To do so, one parameter has to be given up since the problem is over-determined. Here, an iterative approach can be used to find an optimal solution. The transfer function which describes the pulse shaping process can be split into an amplitude and

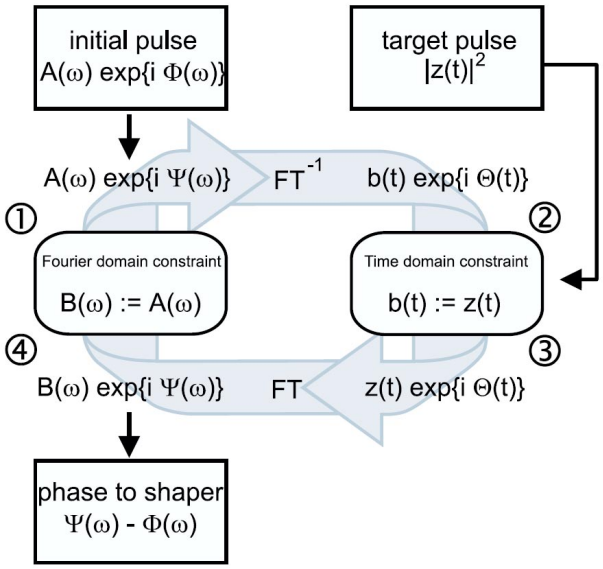

Figure 4.4: Schematic representation of the Fourier transform iteration method for phase shaped laser pulses. This image was taken from [27].

phase. If only phase shaping is available, the amplitude of the transfer function is zero ($R(\omega) = 0$) such that:

$$E_{out}(\omega) = H(\omega)E_{in} = e^{i\Psi(\omega)}E_{in}(\omega) \tag{4.3.14}$$

The goal of this algorithm is to find a pareto optimal phase $\Psi(\omega)$ to apply to the input pulse that simultaneously fulfils the two boundary conditions. The algorithm acts as follows: The input pulse $A(\omega)e^{i\varphi(\omega)}$ is transformed into the time domain:

$$B(t)e^{i\theta(t)} = \mathcal{F}^{-1}\left(A(\omega)e^{i\varphi(\omega)}\right) \tag{4.3.15}$$

then the desired temporal pulse shape ($\sqrt{|I_d|} = E_d(t)$) replaces the temporal field $B(t)$. After a transformation back into frequency space:

$$A'(\omega)e^{\varphi'(\omega)} = \mathcal{F}\left(E_d(t)e^{i\theta(t)}\right) \tag{4.3.16}$$

we find a new spectral phase and amplitude. Since only phase shaping is allowed we will again replace the spectral amplitude with the original amplitude $A(\omega)$. Here, $\varphi'(\omega)$ is the first estimate for the desired spectral phase function $\Psi(\omega)$. The capabilities of this method, as well as an in-depth explanation can be found in [27].

4.4 Properties of Optical Media

In this section, the linear and nonlinear properties of optical media, as well as polarization effects resulting from birefringent material will shortly be introduced.

4.4.1 Dispersion

The way light interacts with bound electrons of an optical medium it traverses, changes with its frequency ω. This so called chromatic dispersion is characterized by the refractive index $n(\omega)$. The refractive index originates from resonances of the optical medium at which photons of the incident light can be absorbed [28]. Knowledge of these resonances is sufficient for stating the Sellmeier equation:

$$n^2(\omega) = 1 + \sum_{k=1}^{m} \frac{B_k\omega_k^2}{\omega_k^2 - \omega^2}. \tag{4.4.1}$$

The set of material parameters B_k, ω_k are crucial for experiments involving ultrashort laser pulses since different wavelengths travel at different speeds $c/n(\omega)$ through optical media. The spectral phase (or rather: $k(\omega)L$) can be expanded into a taylor series:

$$\varphi(\omega) = k(\omega)L = k_0L + L\frac{dk}{d\omega}(\omega - \omega_0) + \frac{L}{2}\frac{d^2k}{d\omega^2}(\omega - \omega_0)^2 + ... \tag{4.4.2}$$

Here $k = n(\omega)\omega/c$ is the wave vector, L the length of the optical medium and ω_0 the central frequency of the pulse's spectrum. The first two coefficients become:

$$\frac{dk}{d\omega} = \frac{1}{v_g} = \frac{1}{c}\left(n + \omega\frac{dn}{d\omega}\right) \tag{4.4.3}$$

$$\frac{d^2k}{d\omega^2} = \frac{1}{c}\left(2\frac{dn}{d\omega} + \omega\frac{d^2n}{d\omega^2}\right) \tag{4.4.4}$$

Eq. 4.4.3 is called group delay (GD) and equates to the temporal shift optical frequencies experience after travelling a distance L through a medium. The group delay is usually stated in units of fs/mm. Eq. 4.4.4 which refers to the change of GD, is called group velocity dispersion (GVD). GVD is expressed in units of fs^2/mm and will result in a broadening (linear chirp) of the pulse after transmission through the medium. When the GVD is greater than zero, the material is said to have normal dispersion, while a GVD less than zero is called abnormal dispersion. Continuation of the spectral phase's Taylor expansion will define higher order material properties like the third-order dispersion (TOD) etc. These terms become particularly significant when dealing with broadband spectra.

For optical waveguides such as fibres, other types of dispersion may become relevant. In an optical fibre multiple propagation modes are possible. Since the propagation speed of each wavelength is constant, fibre modes with wavevectors k_x or k_y that are non-zero will be transmitted slower in the direction of the long fibre axis.

$$k = \frac{n(\omega)\omega}{c} = \sqrt{k_x^2 + k_y^2 + k_z^2} \tag{4.4.5}$$

implies that $k_z < k$ and thereby slower propagation of these modes.

4.4.2 Birefringence

Fibres which possess a non centro-symmetric core as well as most non isotropic materials will feature a special kind of polarization mode dispersion. Birefringence is defined by the difference of the orthogonal refractive indices [29]:

$$B = |n_\perp - n_\parallel| \tag{4.4.6}$$

Where $n_\perp, n_\parallel$ are the refractive indices of the orthogonal optical axes. The optical axis corresponding to the larger refractive index is also called the slow axis while the axis with the smaller refractive index is the fast axis. We can calculate the length at which the phase dependence between both axes is again in sync by:

$$m2\pi = Bk_0L_B \Rightarrow m\lambda = BL_B \Rightarrow L_B = m\frac{\lambda}{B}\lambda \tag{4.4.7}$$

L_B is also called the beat-length after which the polarization state of the incident light will be recovered. The birefringence B of ordinary step-index fibres was found to be in the order of 10^{-5} to 10^{-6} [30]. However, hollow-core fibres can feature much larger birefringence due to their possible asymmetric internal structure [31]. Last but not least, stress by bending or twisting can as well have an effect on birefringence of an optical fibre [28]. Birefringence in optical crystals however is often used for phase matching in frequency conversion applications. In order to maximize the conversion efficiency it has to be ensured that newly created photons interfere positively throughout the crystal. By turning the angle of a birefringent crystal, one can select the refractive index of the extraordinary axis and thereby optimize phase matching between the signal and idling beam.

4.4.3 Intensity Dependent Refractive Index

In linear optics the light-matter interaction is described by the dielectric susceptibility tensor χ:

$$\mathbf{P} = \epsilon_0\chi_{i,j}\mathbf{E} \tag{4.4.8}$$

where, ϵ_0 is the vacuum permittivity and $\mathbf{P}$ the polarization of the optical medium. In the case of isotropic media, this equation can be simplified since $\chi_{xx} = \chi_{yy} = \chi_{zz} = \chi$. For intense electrical fields the optical response from a medium becomes nonlinear. This originates from the fact that, in the high intensity regime, the assumption that electrons are bound to their atoms by a harmonic potential is no longer valid. The total polarization thereby differs from the linear case [32, 33]:

$$P(t) = \epsilon_0 \chi(E)E = \epsilon_0 \left(\chi^{(1)}E(t) + \chi^{(2)}E(t)^2 + \chi^{(3)}E(t)^3 + ...\right) \tag{4.4.9}$$

Here $\chi^{(k)}$ are the k-th order susceptibility. While $\chi^{(1)}$ covers the effects of dispersion, $\chi^{(2)}$ is responsible for second harmonic generation as well as sum frequency generation. It should be noted that $\chi^{(2)}$ can only be non-zero for materials which are not isotropic on the molecular level. Most fibres, as well as gases thereby do not allow efficient second harmonic or sum frequency generation [28]. $\chi^{(3)}$ is an important factor in this thesis, since it is accountable for the Kerr-effect, third-harmonic generation and four-wave mixing [32]. While the Kerr-effect will occur in the experiments discussed later on, other, frequency generating processes can only be efficient when phase matching is observed. It is useful to define a linear and nonlinear polarization P_L and P_{NL}:

$$\mathbf{P}(\mathbf{r}, t) = \mathbf{P}_L(\mathbf{r}, t) + \mathbf{P}_{NL}(\mathbf{r}, t) \tag{4.4.10}$$

The nonlinear refractive index is defined as the change of the refractive index with intensity:

$$n = n_0 + n_2 I \tag{4.4.11}$$

Here I is the intensity (W/cm^2) which relates to the electrical field by:

$$I = \frac{cn\epsilon_0}{2}|E|^2 \tag{4.4.12}$$

Derivation of the Nonlinear Refractive Index

As seen before, we can split the electrical field in a slow and fast oscillating term:

$$\mathbf{E}(\mathbf{r}, t) = \left[\mathbf{A}(\mathbf{r}, t)e^{-i\omega_0 t} + c.c.\right]. \tag{4.4.13}$$

The same is possible for the linear and nonlinear polarization:

$$\mathbf{P}_L = \epsilon_0 \chi^{(1)}\mathbf{E} = \left[\tilde{\mathbf{P}}_L(\mathbf{r}, t)e^{-i\omega_0 t} + c.c\right] \tag{4.4.14}$$

$$\mathbf{P}_{NL} = \epsilon_0 \chi^{(3)}\mathbf{EEE} = \left[\tilde{\mathbf{P}}_{NL}(\mathbf{r}, t)e^{-i\omega_0 t} + c.c\right]. \tag{4.4.15}$$

By substituting Eq.4.4.13 into Eq. 4.4.15 we find

$$\tilde{\mathbf{P}}_{NL}(\mathbf{r}, t) = \epsilon_0 \chi^{(3)} \frac{1}{2}\left(\mathbf{A}^3 e^{-i3\omega_0 t} + 3\mathbf{A}\mathbf{A}^*\mathbf{A}e^{-i\omega_0 t} + c.c.\right). \tag{4.4.16}$$

The term oscillating with the third harmonic will only be relevant when phase matching can be achieved between ω_0 and $3\omega_0$. This is usually not the case in optical fibres or gases and will therefore be neglected. This finally leads to the relation between the nonlinear polarizability and the electrical field:

$$P_{NL} = \epsilon_0 \epsilon_{NL} E = \epsilon_0 3\chi^{(3)}|\mathbf{A}|^2\mathbf{A}, \tag{4.4.17}$$

which implies for the dielectric constant that:

$$\epsilon = 1 + \chi^{(1)} + \epsilon_{NL} = n^2 + \frac{3}{4}\chi^{(3)}|\mathbf{A}|^2. \tag{4.4.18}$$

Assuming that the occurring nonlinearities are a small perturbation to the refractive index we write

$$\epsilon = (n + n_2|\mathbf{A}|^2)^2 \approx n^2 + 2n_2|\mathbf{A}|^2 n \tag{4.4.19}$$

Identification results in the formula for the relation between the nonlinear refractive index and the third-order susceptibility $\chi^{(3)}$:

$$n_2 = \frac{3}{2n}\chi^{(3)}. \tag{4.4.20}$$

4.5 Light-Matter Interactions

The most relevant concepts concerning the interaction of laser pulses with matter will be introduced in this chapter. First, the concept of multiphoton excitation will be differentiated from single photon excitation. Then, secondary processes like fluorescence and photoionisation are discussed. In the context of the simulation of laser pulse propagation, different ionisation schemes will be investigated.

4.5.1 Multiphoton Excitation

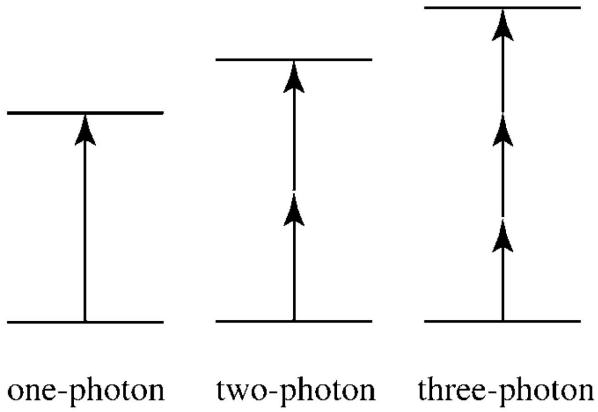

Figure 4.5: Examples for different excitation schemes. One, two, or more photons can simultaneously be absorbed and lead to the excitation of an atom or molecule. Different selection rules apply depending on the order of the process. This image originates from [33].

The first experiments on multiphoton excitation were performed by Kaiser and Garrett in 1961 [34] with a ruby laser, which was at that time called an optical maser. When high intensity laser systems became more common, applications of this new method of excitation were explored. In 1990, Denk et al. [35] demonstrated the advantages of two-photon excitation in microscopy applications. Multiphoton excitation, which relies on the simultaneous absorption of two or more photons can significantly enhance the resolution when used in a laser scanning microscope.

Since the diffraction limit is dependent on the wavelength of the exciting light, using two-photons cuts in half the wavelength used for excitation and thereby doubles the resolution which

is achieved. A second advantage of multiphoton microscopy is that the process is efficient at high intensities and scales with I^n, where n is the number of photons required for excitation. This means that only a volume close to the focus will be excited which is employed for creating three-dimensional images of a sample. Additionally multiphoton microscopy follows different selection rules than single photon excitation. A photon possesses an angular momentum of ± 1, while a two-photon transition requires an angular momentum change of $\pm 2, 0$. Therefore other, prior unreachable, states can be excited. Two-photon excitation at a frequency $2\omega_0$ is achieved by two photons with the energies $\omega_1 + \omega_2 = 2\omega_0$. To find the efficiency at which a certain transition is excited $E(\omega) = |E(\omega)|e^{i\phi(\omega)}$, one has to integrate over each possible combination of photon energies resulting in the total energy required for the transition.

$$E^{(2)}(2\omega_0) = \int_{-\infty}^{\infty} |E(\omega_0 - \Omega)||E(\omega_0 + \Omega)|e^{i(\phi(\omega_0-\Omega)+\phi(\omega_0+\Omega))} \tag{4.5.1}$$

The spectral phase $\Phi(\omega)$ determines if the two photons interfere constructively or destructively. If the phase is antisymmetric around ω_0, i.e.: $\Phi(\omega_0 + \Omega) = -\Phi(\omega_0 - \Omega)$, the two photon field $E^{(2)}(2\omega_0)$ will be maximal. At frequencies other than ω_0 this antisymmetric field (if not zero) will lead to destructive interference and therefore can be used to excite two-photon transitions selectively. The rate at which two-photon excitation occurs is furthermore determined by the two-photon cross section:

$$R^{(2)}(\omega) = \sigma^{(2)}(\omega)I^2 \tag{4.5.2}$$

This efficiency can be greatly increased if a resonance exists at the energy of one photon. If three photons are simultaneously absorbed the three-photon field can be calculated by:

$$E^{(3)}(3\omega_0) = \int_{-\infty}^{\infty} |E(\omega_0 - \Omega_1 - \Omega_2)||E(\Omega_1)||E(\Omega_2)|e^{i(\Phi(\omega_0-\Omega_1-\Omega_2)+\Phi(\Omega_1)+\Phi(\Omega_2))}d\Omega_1 d\Omega_2 \tag{4.5.3}$$

The rate is calculated accordingly:

$$R^{(3)}(\omega) = \sigma^{(3)}(\omega)I^3 \tag{4.5.4}$$

While three-photon excitation in principle shows the same properties as two-photon excitation, antisymmetric phase terms do not lead to maximal absorbance as in the two-photon case. It is clear that it is not possible to find a phase function for which $\Phi(\omega_0 - \Omega_1 - \Omega_2) = -\Phi(\Omega_1) - \Phi(\Omega_2)$ except $\Phi(\omega) = 0$. This leads to the conclusion that only the transform limited pulse maximizes higher order multiphoton excitation.

4.5.2 Fluorescence

Fluorescence is the process in which a molecule called fluorophore emits light under relaxation from an excited state. The wavelength of the emitted light depends on the energy difference between the initial (excited) and final (relaxed) state. This spectral distribution emitted by a fluorophore is called fluorescence spectrum. Fluorescence is a fast process in which lights is emitted in the timescale of ns upon excitation. When, in certain cases the relaxation process is forbidden by selection rules, light can be emitted over macroscopic timescales, which is then called phosphorescence. Fluorescence spectra are always red-shifted with regard to the absorption spectrum. This effect, called stokes-shift, is due to internal relaxations over non-radiative transitions. Another property of fluorescence spectra is their polarization. When a fluorophore is excited by linear polarized light, molecules with an aligned dipole transition element will be more efficiently excited

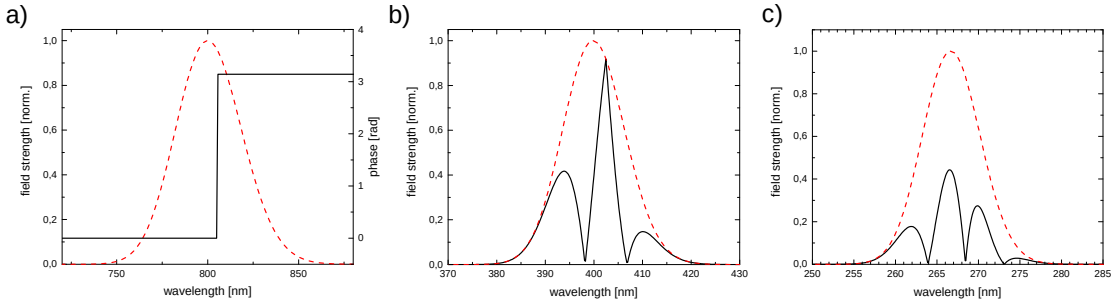

Figure 4.6: This graph illustrates the effect of a pi-step spectral phase on the two and three-photon field. a) Shows a Gaussian spectrum as well as the pi-step phase used to in eq. 4.5.1 and 4.5.3. In (b) we can see the two-photon field which reaches a value equal to the transform limited two photon field at the wavelength of the phase's antisymmetry. While the three-photon field (c) looks similar, the phase modulation led to an overall reduced efficiency in three-photon excitation.

than perpendicular aligned fluorophores. After a certain time period the excited fluorophore will relax and emit light polarized parallel to the dipole transition element once again. If the molecule is stationary and no internal energy transfer occurs, the polarization of the emitted photons should in average aligned with the polarization of the exciting light. The polarization of the emitted light is characterized by the fluorescence anisotropy:

$$r = \frac{I_{\parallel} - I_{\perp}}{I_{\parallel} - 2I_{\perp}}, \tag{4.5.5}$$

where $I_{\perp}$ and $I_{\parallel}$ are the fluorescence intensities perpendicular and parallel with respect to the linear polarized exciting light. Here, temperature and viscosity will have a great impact since fast rotation will reduce the measured fluorescence anisotropy. Finally, the quantum yield is defined by:

$$\Phi = \frac{\text{Number of photons emitted}}{\text{Number of photons absorbed}}, \tag{4.5.6}$$

which describes the efficiency at which fluorescence will take place. This can be reduced by competition of the fluorescence with non radiant processes (i.e.: collision induced relaxation).

4.5.3 Photoionisation

When the energy of a single photon surpasses the atom's ionisation potential (IP) ($\approx 10eV$) an electron can be seperated from the atom via the photo-effect. The electron will then retain the kinetic energy:

$$E_{kin} = \hbar\omega - IP \tag{4.5.7}$$

For his work on the photo-effect, Albert Einstein was rewarded the Nobel Prize in 1921. When the photon-energy is lower than the ionisation potential, no electron will be emitted. When we assume the ionisation potential of Hydrogen, which equals $13.6\,eV$, we find that the exciting light has to have a wavelength of $91\,nm$ or lower. Although molecules may possess IP's lower than that of hydrogen, it is evident that UV light or a simulatneous absorption of multiple photons is required for this effect to occur. No laser used for experiments in this thesis reaches far enough into the UV-spectrum. Hence, ionisation will most likely occur via multiple photons.

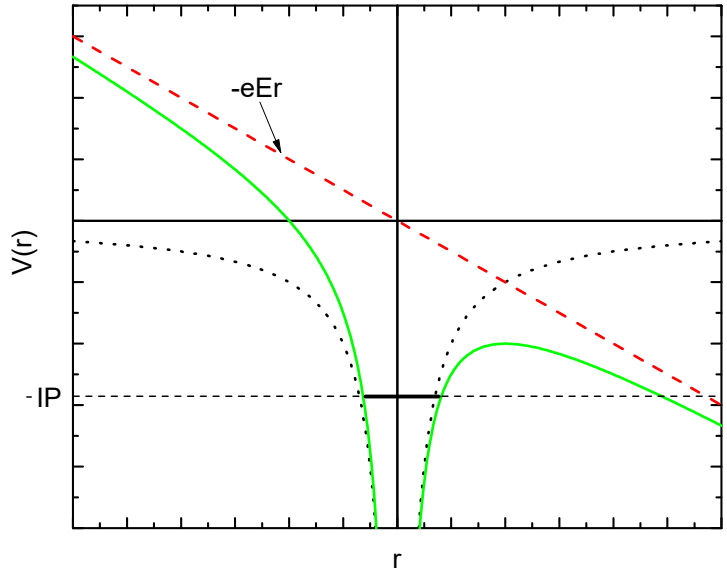

Figure 4.7: Bending of an atomic potential in an electrical field. When the electrical field reaches a certain strength, tunnelling through the remaining barrier becomes possible. If the field strength is even stronger over the barrier ionisation can occur.

Multiphoton Ionisation

Multiphoton ionisation is the process of ionisation after the absorbance of more than one photon. While the process of multiphoton ionisation is extremely improbable at low intensities, its efficiency increases with the order of I^N, where N is the number of photons required for ionisation. As M. Göppert-Mayer suggested in 1931 [36] the energy can be raised by multiple photons of lower energy. The rate at which ionisation occurs in the multiphoton regime is given by [37, 38]:

$$W_{mp} = \frac{2\pi\omega_0}{(l-1)!}\frac{I(\mathbf{r},\tau)^l}{(\hbar\omega_0^2\sigma_{mp})^l}, \tag{4.5.8}$$

where l is the number of photons required to achieve ionisation, σ_{mp} is the multiphoton cross-section and I is the intensity of the laser given in the retarded reference frame. This rate was derived using a rate equation approach where multiphoton absorption is seen as a process of consecutive single photon absorptions into virtual excited states [38].

Tunnel and OTB Ionisation

In filamentation which usually involves extremely short laser pulses other ionisation processes can become important. This is due to the fact that at high intensities the approximation that the electronic potential is undisturbed by the laser field breaks down [39]. In case of an electrical field of extremely high intensity the atomic potential might be deformed such that the tunnel probability through the remaining potential wall becomes possible. This process, called tunnel-ionisation, is dominant when the electrical field is oscillating slowly. Fig. 4.7 shows how the electrical field $-eEr$ changes the shape of the atomic potential $V(r)$. A measure of the tunnel-probability can be found in comparing the time required for an electron to tunnel out of the atom with the oscillation period of the laser field. The tunnelling time can be estimated via the distance the electron has to tunnel and its kinetic energy. The frequency times the tunnelling time then is:

$$\omega t_{tunnel} = \frac{s}{v} = \frac{IP}{eE}\sqrt{\frac{m_e}{2IP}} = \omega\frac{\sqrt{2m_eIP}}{2eE}. \tag{4.5.9}$$

$$\gamma_K = \omega \frac{\sqrt{2m_e IP}}{eE} \approx \omega t_{tunnel} \tag{4.5.10}$$

γ_K is called Keldysh parameter [40] and was found to indicate that multiphoton ionisation is dominant when $\gamma_K > 1/2$ and tunnel ionisation prevails when $\gamma_K < 1/2$ [41]. This Keldysh parameter is sometimes also compared to the ratio of the ionisation energy and the ponderomotive energy:

$$\gamma_K \approx \sqrt{\frac{IP}{U_P}}, \tag{4.5.11}$$

where the value of the ponderomotive energy is given by

$$U_P = \frac{e^2 E^2}{4m_e \omega_0^2}, \tag{4.5.12}$$

which is the energy a free electron gains in the oscillating electrical field during one laser cycle. At extremely high intensities, which are out of reach for laser systems used in the experiments for this thesis, another ionisation scheme emerges. As the electrical field, like it is depicted in Fig. 4.7, deforms the atomic potential the field strength can reach a value when the potential barrier is reduced by the binding energy of the valence electrons. Ionisation in this regime is called over the barrier ionisation. Further information can be found in [39].

4.6 Propagation of Ultrashort Laser Pulses

Since simulations of the pulse propagation are a substantial part of this thesis, the required equations will be introduced in this chapter. First, the full wave equation will be formulated. Later, the separate linear and nonlinear effects will be discussed. Finally, the split-step method will be derived shortly. It allows for efficient calculation of the pulse propagation by step-wise integration of the wave equation. This chapter is influenced by the notation and derivations in [28, 33].

4.6.1 The Nonlinear Schrödinger Equation

All electromagnetic effects and thus laser pulses are governed by the Maxwell equations:

$$\nabla \times \mathbf{E} = -\frac{\partial \mathbf{B}}{\partial t}, \tag{4.6.1}$$

$$\nabla \times \mathbf{H} = \mathbf{J} + \frac{\partial \mathbf{D}}{\partial t}, \tag{4.6.2}$$

$$\nabla \mathbf{D} = \rho_f, \tag{4.6.3}$$

$$\nabla \mathbf{B} = 0, \tag{4.6.4}$$

where $\mathbf{H}$ and $\mathbf{E}$ are the magnetic and electrical field and $\mathbf{D}$ and $\mathbf{B}$ are the electrical and magnetic flux density. $\mathbf{J}$ is the current density, whereas ρ_f is the free charge density. $\mathbf{J}$ and $\rho_f = \rho - \rho_{pol}$ are the sources for the magnetic and electrical fields. In a vacuum or uncharged media both become zero, largely simplifying the equations. In optical media the electrical and magnetic fields give rise to the flux densities:

$$\mathbf{D} = \epsilon_0 \mathbf{E} + \mathbf{P} \tag{4.6.5}$$

$$\mathbf{B} = \mu_0 \mathbf{H} + \mathbf{M} \tag{4.6.6}$$

$\mathbf{P}$ and $\mathbf{M}$ are the electrical and magnetic polarization. The liquids, gases and crystals used in this thesis are not magnetic. Therefore, we can safely assume $\mathbf{M} = 0$. It is possible to eliminate the magnetic field and the electrical flux density from the equation set. With the curl of Eq. 4.6.1 and the aid of all other Maxwell equations we get:

$$\nabla \times \nabla \times \mathbf{E} = -\frac{1}{c^2}\frac{\partial^2 \mathbf{E}}{\partial t^2} - \mu_0 \left[\frac{\partial^2 \mathbf{P}}{\partial t^2} + \frac{\partial \mathbf{J}}{\partial t}\right] \tag{4.6.7}$$

When we further use the identity $\nabla \times \nabla \times \mathbf{E} = \nabla(\nabla \mathbf{E}) - \Delta \mathbf{E}$, Eq. 4.6.3 and Eq. 4.6.5 we find:

$$\Delta \mathbf{E} - \frac{1}{c^2}\frac{\partial^2 \mathbf{E}}{\partial t^2} = \mu_0 \frac{\partial^2 \mathbf{P}}{\partial t^2} + \mu_0 \frac{\partial \mathbf{J}}{\partial t} + \frac{1}{\epsilon_0}\nabla \rho \tag{4.6.8}$$

This is the full wave equation including charges, currents and the influence of polarisable optical media. It can only be solved using numerical methods, of which the most commonly used method is integration.

Solutions of the Wave Equation in Optical Media without Free Charges

When no sources for the electromagnetic field are present, the wave equation 4.6.8 simplifies to:

$$\Delta \mathbf{E} - \frac{1}{c^2}\frac{\partial^2 \mathbf{E}}{\partial t^2} = \mu_0 \frac{\partial^2 \mathbf{P_L}}{\partial t^2} + \mu_0 \frac{\partial^2 \mathbf{P_{NL}}}{\partial t^2} \tag{4.6.9}$$

Because most material properties are given depending on the wavelength of the incident light, it is advantageous to transform eq. 4.6.9 into the Fourier domain.

For this we will express all quantities as their Fourier transform:

$$\mathbf{E}(\mathbf{r}, t) = \frac{1}{2\pi}\int_{-\infty}^{\infty} \mathbf{E}(\mathbf{r}, \omega) e^{-i\omega t} d\omega \tag{4.6.10}$$

$$\mathbf{P}_L(\mathbf{r}, t) = \frac{1}{2\pi}\int_{-\infty}^{\infty} \mathbf{P}_L(\mathbf{r}, \omega) e^{-i\omega t} d\omega \tag{4.6.11}$$

$$\mathbf{P}_{NL}(\mathbf{r}, t) = \frac{1}{2\pi}\int_{-\infty}^{\infty} \mathbf{P}_{NL}(\mathbf{r}, \omega) e^{-i\omega t} d\omega \tag{4.6.12}$$

The linear polarization arises from the the first order $\chi^{(1)}$ and is related to the electrical field by

$$\mathbf{P}_L(\omega)(\mathbf{r}, t) = \epsilon_0 \chi^{(1)}(\omega)\mathbf{E}(\mathbf{r}, \omega). \tag{4.6.13}$$

By taking the Fourier transform of equation 4.6.9 one can make use of the very useful identity

$$\mathcal{F}\left(\frac{d^n f(t)}{dt^n}\right) = (i\omega)^n f(\omega) \tag{4.6.14}$$

and thus one can write:

$$\Delta \mathbf{E}(\mathbf{r}, \omega) - \left(1 + \chi^{(1)}(\omega)\right)\frac{\omega_0^2}{c^2}\mathbf{E}(\mathbf{r}, \omega) = -\mu_0 \omega_0^2 \mathbf{P}_{NL}(\omega). \tag{4.6.15}$$

It is known that plane waves are a solution to the wave equation in free space ($\epsilon(\omega) = \epsilon_0$). This gives rise to the slowly varying envelope approximation (SVAE) . It is assumed that solutions to 4.6.15 are of the type:

$$\mathbf{E}(\mathbf{r}, t) = \left(\mathbf{A}(\mathbf{r}, t) e^{i(k_0 z - \omega_0 t)} + c.c.\right) \tag{4.6.16}$$

SVAE generally speaking means that we assume the changes of $\mathbf{A}(\mathbf{r},t)$ are slow compared to the oscillations ω_0:

$$\left|\frac{\partial \mathbf{A}}{\partial t}\right| \ll |\omega_0 \mathbf{A}|. \tag{4.6.17}$$

ω_0 is often called the carrier frequency, while k_0 is the linear wavevector at this carrier frequency. By expressing the slowly varying amplitude as its fourier-transform as well,

$$\mathbf{A}(\mathbf{r},t) = \frac{1}{2\pi}\int_{-\infty}^{\infty} \mathbf{A}(\mathbf{r},\omega)e^{-i\omega t}d\omega, \tag{4.6.18}$$

equation 4.6.15 can be written as:

$$\Delta\mathbf{A}(\mathbf{r},\omega) + 2ik_0\frac{\partial \mathbf{A}(\mathbf{r},\omega)}{\partial z} + [k^2(\omega) - k_0^2]\mathbf{A}(\mathbf{r},\omega) = -\mu_0\omega^2 P_{NL}(\mathbf{r},\omega)e^{-ik_0 z}. \tag{4.6.19}$$

This differential equation describes the evolution of the slowly varying amplitude $\mathbf{A}(\mathbf{r},\omega)$ in the frequency space. Let's now take a look at the mathematical description of various effects included in this formula.

4.6.2 Dispersion

As already shown in chapter 4.4.1, $k(\omega)$ can be expanded into a taylor series.

$$k(\omega) = k_0 + k_1(\omega-\omega_0) + \sum_{n=2}^{\infty}\frac{1}{n!}k_n(\omega-\omega_0)^n \tag{4.6.20}$$

k_0 and k_1 were excluded from the sum because they have distinct physical significance. k_0 is the wavevector at ω_0 and k_1 equals the inverse of the group velocity $1/v_g$. For clarity, we introduce the dispersion operator D:

$$D(\omega) = \sum_{n=2}^{\infty}\frac{1}{n!}k_n(\omega-\omega_0)^n \tag{4.6.21}$$

With this, equation 4.6.19 becomes:

$$\begin{aligned}\Delta\mathbf{A} + 2ik_0\frac{\partial \mathbf{A}}{\partial z} + \left[2k_0k_1(\omega-\omega_0) + k_1^2(\omega-\omega_0)^2 + 2k_0D(\omega) + 2k_1(\omega-\omega_0)D(\omega)\right]\mathbf{A} \\ = -\mu_0\omega^2\mathbf{P}_{NL}e^{-ik_0z}\end{aligned} \tag{4.6.22}$$

At this point $D(\omega)^2$ was neglected because it is small compared to the other terms. The parameters used in the expansion in equation 4.6.21, are the well known material quantities discussed earlier in chapter 4.4.1. The propagation through space ($\Delta\mathbf{A}$) of the slowly varying amplitude is governed by the dispersion of the optical medium ($D(\omega)$) as well as the nonlinear polarizability ($\mathbf{P}_{NL}(\mathbf{r},\omega)$). This equation can be analysed in Fourier space as well. A Fourier-transform gives rise to

$$\begin{aligned}\Delta\mathbf{A}(\mathbf{r},t) + \left[2ik_0\left(k_1\frac{\partial}{\partial t} + \frac{\partial}{\partial z}\right) - k_1^2\frac{\partial^2}{\partial t^2} + 2k_0D(t) + 2ik_1D(t)\frac{\partial}{\partial t}\right]\mathbf{A}(\mathbf{r},t) \\ = \mu_0\frac{\partial^2}{\partial t^2}\mathbf{P}_{NL}(\mathbf{r},t)e^{-i(k_0z-\omega_0t)}\end{aligned} \tag{4.6.23}$$

in which

$$D(t) = \sum_{n=2}^{\infty}\frac{1}{n!}k_n\left(i\frac{\partial}{\partial t}\right)^n \tag{4.6.24}$$

Depending on whether linear or nonlinear effects are dominating the propagation equation will later be solved either in frequency or temporal space.

4.6.3 Nonlinear Polarizability

In order to further analyse the nonlinear polarizability, the slowly varying amplitude approximation will be applied as before:

$$\mathbf{P}_{NL}(\mathbf{r},t) = \tilde{\mathbf{P}}_{NL}(\mathbf{r},t)e^{i(k_0 z-\omega_0 t)} + c.c. \tag{4.6.25}$$

It was found earlier, that the nonlinear polarizability of an isotrope material and an instantaneous response on the electrical field is:

$$\tilde{\mathbf{P}}_{NL} = 3\epsilon_0\chi^{(3)}|\mathbf{A}(\mathbf{r},t)|^2\mathbf{A}(\mathbf{r},t). \tag{4.6.26}$$

The first and second derivative of $\mathbf{P}_{NL}$ and thus become:

$$\frac{\partial}{\partial t}\mathbf{P}_{NL} = \left[\frac{\partial}{\partial t} - i\omega_0\right]\tilde{\mathbf{P}}_{NL}(\mathbf{r},t)e^{i(k_0 z-\omega_0 t)} + c.c \tag{4.6.27}$$

$$\frac{\partial^2}{\partial t^2}\mathbf{P}_{NL} = -\omega_0^2 e^{i(k_0 z-\omega_0 t)}\left(1+\frac{i}{\omega_0}\frac{\partial}{\partial t}\right)^2\tilde{\mathbf{P}}_{NL}(\mathbf{r},t) + c.c \tag{4.6.28}$$

When the second derivative is inserted into eq. 4.6.23 one find:

$$\begin{aligned}\Delta\mathbf{A}(\mathbf{r},t) + &\left[2ik_0\left(k_1\frac{\partial}{\partial t}+\frac{\partial}{\partial z}\right) - k_1^2\frac{\partial^2}{\partial t^2} + 2k_0 D(t) + 2ik_1 D(t)\frac{\partial}{\partial t}\right]\mathbf{A}(\mathbf{r},t)\\ &= -\mu_0\omega_0^2\left(1+\frac{i}{\omega_0}\frac{\partial}{\partial t}\right)^2\tilde{\mathbf{P}}_{NL}(\mathbf{r},t)\end{aligned} \tag{4.6.29}$$

Using relation 4.6.26 and by dropping higher order derivatives respecting the SVAE, one can approximate the right hand side of eq. 4.6.29 by neglecting the second derivative with respect to t [33]:

$$\begin{aligned}&\left[\Delta + 2ik_0\left(k_1\frac{\partial}{\partial t}+\frac{\partial}{\partial z}\right) - k_1^2\frac{\partial^2}{\partial t^2} + 2k_0 D(t)\left(1+i\frac{k_1}{k_0}\frac{\partial}{\partial t}\right)\right]\mathbf{A}(\mathbf{r},t)\\ &= -3\frac{\omega_0^2}{c^2}\left(1+\frac{2i}{\omega_0}\frac{\partial}{\partial t}\right)\chi^{(3)}|\mathbf{A}(\mathbf{r},t)|^2\mathbf{A}(\mathbf{r},t)\end{aligned} \tag{4.6.30}$$

4.6.4 Retarded Frame of Reference

Coming from eq. 4.6.9 the slowly varying envelope approximation for the polarizability as well as the electrical field was introduced. In the last two subchapters the dispersion and basic nonlinearities in isotropic media with an instantaneous response were both covered. Another important step towards numerically solving the wave propagation is the introduction of the retarded time frame [33]. It was found that k_1 equals the inverse of the group velocity. The retarded time frame moves along with the pulse at group velocity. One can substitute:

$$\tau = t - \frac{z}{v_g} = t - k_1 z \text{ and } z = z', \tag{4.6.31}$$

so that the differentials become:

$$\frac{\partial}{\partial\tau} = \frac{\partial}{\partial t} \text{ and } \frac{\partial}{\partial z} = \frac{\partial}{\partial z'} - k_1\frac{\partial}{\partial\tau}. \tag{4.6.32}$$

This leads to a wave equation (see eq. 4.6.29) in the form of:

$$\begin{aligned}\nabla_\perp^2 \mathbf{A}(\mathbf{r},t) + 2ik_0\frac{\partial}{\partial z'}\left(1 + i\frac{k_1}{k_0}\frac{\partial}{\partial\tau}\right)\mathbf{A}(\mathbf{r},t) + 2k_0 D(t)\left(1 + i\frac{k_1}{k_0}\frac{\partial}{\partial\tau}\right)\mathbf{A}(\mathbf{r},t) \\ = -\mu_0\omega_0^2\left(1 + \frac{i}{\omega_0}\frac{\partial}{\partial\tau}\right)^2 \tilde{\mathbf{P}}_{NL}(\mathbf{r},t),\end{aligned} \tag{4.6.33}$$

where one neglects the second derivative with respect to z' (in accordance with the SVAE). With the help of $k_0 = n\omega_0/c$ and $k_1 = 1/v_g$ the ratio k_1/k_0 becomes: $k_1/k_0 = c/nv_g\omega_0 \approx 1/\omega_0$ and thus:

$$\begin{aligned}\nabla_\perp^2 \mathbf{A}(\mathbf{r},t) + 2ik_0\frac{\partial}{\partial z'}\left(1 + i\frac{1}{\omega_0}\frac{\partial}{\partial\tau}\right)\mathbf{A}(\mathbf{r},t) + 2k_0 D(t)\left(1 + i\frac{1}{\omega_0}\frac{\partial}{\partial\tau}\right)\mathbf{A}(\mathbf{r},t) \\ = -\mu_0\omega_0^2\left(1 + \frac{i}{\omega_0}\frac{\partial}{\partial\tau}\right)^2 \tilde{\mathbf{P}}_{NL}(\mathbf{r},t),\end{aligned} \tag{4.6.34}$$

or:

$$\left[\left(1 + \frac{i}{\omega_0}\frac{\partial}{\partial\tau}\right)^{-1}\nabla_\perp^2 + 2ik_0\frac{\partial}{\partial z'} + 2k_0 D(t)\right]\mathbf{A}(\mathbf{r},t) = -\mu_0\omega_0^2\left(1 + \frac{i}{\omega_0}\frac{\partial}{\partial\tau}\right)\tilde{\mathbf{P}}_{NL}(\mathbf{r},t), \tag{4.6.35}$$

In order to discuss the relevant terms of this equation the correction terms are neglected $\left(1 + \frac{i}{\omega_0}\frac{\partial}{\partial\tau}\right) \approx 1$.

$$\frac{\partial}{\partial z'}\mathbf{A}(\mathbf{r},t) = \left[\frac{i}{2k_0}\nabla_\perp^2 + iD(t) + \frac{i3\omega_0}{2c}\chi^{(3)}|\mathbf{A}(\mathbf{r},t)|^2\right]\mathbf{A}(\mathbf{r},t) \tag{4.6.36}$$

It becomes quite clear that after some simplifications the propagation of the electrical field is determined by a combination of diffraction ($\frac{i}{2k_0}\nabla_\perp^2$), dispersion ($iD(t)$) and nonlinear phase acquisition, or self-phase modulation (SPM) ($\frac{i\omega_0}{2c}\chi^{(3)}|\mathbf{A}^2|$).

4.6.5 Self-Phase Modulation

We will now take a look at the simplified wave equation from last chapter. By finding a solution for the nonlinear term only we can understand what a high intensity laser pulse in a low dispersion medium would experience.

$$\frac{\partial}{\partial z'}\mathbf{A}(z,t) = \frac{i3\omega_0}{2c}\chi^{(3)}|\mathbf{A}(z,t)|^2\mathbf{A}(z,t) \tag{4.6.37}$$

Here, it is customary to introduce a normalized amplitude $\mathbf{U}(z,\tau)$ [28], for which $U(0,0)$ was chosen to be 1:

$$\mathbf{A}(z,\tau) = \sqrt{P_0}\mathbf{U}(z,\tau), \tag{4.6.38}$$

where P_0 is the peak power of the laser pulse. Using the approach $\mathbf{U}(z,\tau) = \mathbf{U}(0,\tau)e^{i\Phi_{NL}(z,\tau)}$ leaves eq. 4.6.37 as:

$$\frac{\partial\Phi_{NL}(z,\tau)}{\partial z} = \frac{3\omega_0 P_0}{2c}\chi^{(3)}|\mathbf{U}(0,\tau)|^2 \tag{4.6.39}$$

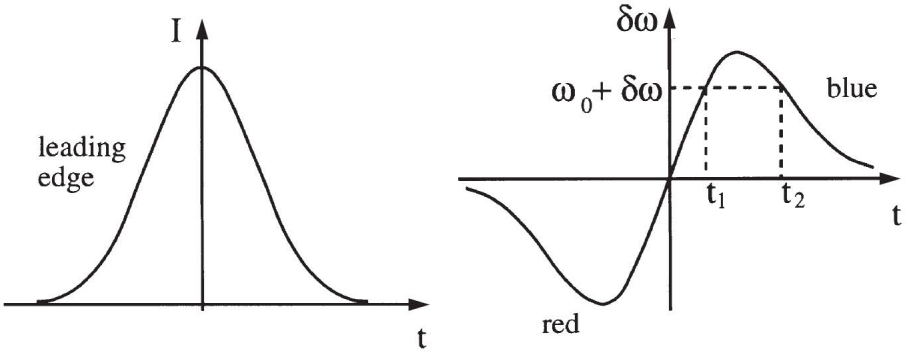

Figure 4.8: (left) A Gaussian laser pulse. (right) frequency shift originating from the intensity dependent refractive index. Early frequencies are red-shifted, while pulses on the trailing flank are blue shifted. This can result in spectrally broadened or narrowed laser pulses after passing through a nonlinear medium. This image was taken from [15]

The nonlinear phase is therefore proportional to the intensity of the laser pulse:

$$\Phi_{NL}(z,\tau) = \frac{3\omega_0 P_0}{2c}\chi^{(3)}|\mathbf{U}(0,\tau)|^2 z \tag{4.6.40}$$

In this equation, one can identify the nonlinear refractive index as introduced in chapter 4.4.3.

$$\Phi_{NL}(z,\tau) = k_0 n_2 P_0 |\mathbf{U}(0,\tau)|^2 z \tag{4.6.41}$$

Here, it becomes apparent that a laser pulse with high intensity picks up a phase while propagating through the material. This phase change will lead to a frequency shift of the instantaneous frequency. By calculating the derivative of the nonlinear phase, one can determine the nonlinear frequency shift:

$$d\omega = -\frac{\partial \Phi_{NL}(z,t)}{\partial t} = -k_0 n_2 P_0 \frac{\partial |\mathbf{U}(0,t)|^2}{\partial t} z \tag{4.6.42}$$

This frequency-shift has a profound effect on incident laser pulses in nonlinear media. A positively chirped (or transform-limited) laser pulse will experience spectral broadening. As can be understood from the last equation, the instantaneous frequency is shifted to longer wavelengths at the leading and to shorter wavelengths at the trailing flank of the pulse, thus broadening the spectrum. The opposite is true for a negatively chirped pulse. A negatively chirped pulse possesses short wavelengths at the beginning and long wavelengths at the end of the pulse. The nonlinear frequency shift thus increases the wavelength at the beginning and reduces the wavelength at the end of the pulse, resulting in a narrowed spectrum. This is why high peak intensities and strongly nonlinear optical media can be used for generation of ultra broadband light (e.g.: amplified laser pulses and thin sapphire plates [42, 43]).

4.6.6 Self-Steepening

Self-steepening is a high order nonlinear effect which occurs when pulses get even shorter ($< 100fs$ [28]) and the correction factor in $\frac{i}{\omega_0}\frac{\partial}{\partial\tau}$ can no longer be neglected. Taking a look at this term will allow for a basic understanding of this process. Starting from equation 4.6.30 which described pulse propagation in the laboratory frame the second derivative by z is neglected according to the

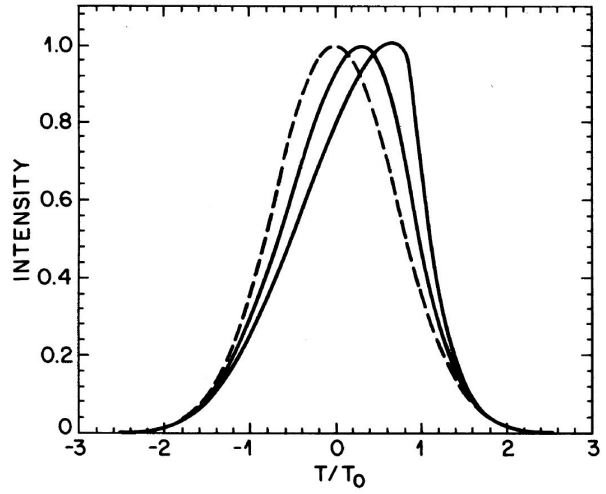

Figure 4.9: An example of the effect on self-steepening on a Gaussian laser pulse. The dashed line shows the non-distorted pulse, while the sold lines represent a self-steepened pulse experiencing increasing non-linearity. This image was taken from [28].

slowly varying envelope approximation.

$$\left[\frac{\partial}{\partial z} - \frac{i}{2k_0}\nabla_\perp^2 + \frac{n_0^{(g)}}{c}\frac{\partial}{\partial t} + \frac{ik_2}{2}\frac{\partial}{\partial t^2}\right]\mathbf{A}(\mathbf{r},t) = \frac{i3\omega_0}{2nc}\left(1 + \frac{i2}{\omega_0}\frac{\partial}{\partial t}\right)\chi^{(3)}|\mathbf{A}(\mathbf{r},t)|^2\mathbf{A}(\mathbf{r},t) \tag{4.6.43}$$

All higher order dispersion terms except the first $\left(D(t) = -\frac{1}{2}k_2\frac{\partial}{\partial t^2}\right)$ were dropped as well since only the effects due to higher order nonlinearities are going to be observed. It is useful to introduce the group velocity index $n_0^{(g)} = c/v_g$ which describes the slowdown experienced by the group velocity due to the medium, just like the reduction of the phase velocity is specified by the refractive index. It is noteworthy that when one would ignore the term $\frac{2i}{\omega_0}\frac{\partial}{\partial t}$ one could still make all approximations and find the results from chapter 4.6.5. For clarity a new quantity is introduced:

$$\gamma = \frac{3\omega_0}{2nc}\chi^{(3)}. \tag{4.6.44}$$

One thus finds:

$$\begin{aligned}\left[\frac{\partial}{\partial z} - \frac{i}{2k_0}\nabla_\perp^2 + \frac{n_0^{(g)}}{c}\frac{\partial}{\partial t} + \frac{ik_2}{2}\frac{\partial}{\partial t^2}\right]\mathbf{A}(\mathbf{r},t) &= i\gamma|\mathbf{A}(\mathbf{r},t)|^2\mathbf{A}(\mathbf{r},t) \\ &- \frac{4\gamma}{\omega_0}|\mathbf{A}(\mathbf{r},t)|^2\frac{\partial\mathbf{A}(\mathbf{r},t)}{\partial t} - \frac{2\gamma}{\omega_0}\mathbf{A}(\mathbf{r},t)^2\frac{\partial\mathbf{A}^*(\mathbf{r},t)}{\partial t}\end{aligned} \tag{4.6.45}$$

In the last step the derivative of the amplitude is evaluated. Both are real and thereby act on the amplitude of $\mathbf{A}$ (in contrast to the self-phase modulation term which gives rise to a phase). After rewriting,

$$\left[\frac{\partial}{\partial z} - \frac{i}{2k_0}\nabla_\perp^2 + \frac{n_{eff}^{(g)}}{c}\frac{\partial}{\partial t} + \frac{ik_2}{2}\frac{\partial}{\partial t^2}\right]\mathbf{A}(\mathbf{r},t) = i\gamma|\mathbf{A}(\mathbf{r},t)|^2\mathbf{A}(\mathbf{r},t) - \frac{2\gamma}{\omega_0}\mathbf{A}(\mathbf{r},t)^2\frac{\partial\mathbf{A}^*(\mathbf{r},t)}{\partial t} \tag{4.6.46}$$

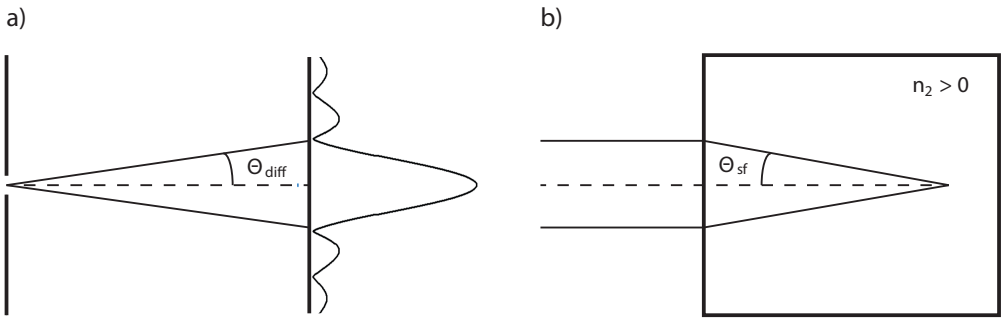

Figure 4.10: Illustration of the a) diffraction angle and b) self-focussing angle.

one can see that self steepening results in a intensity dependence of the group velocity:

$$n_{eff}^{(g)} = n_0^{(g)} + \frac{4\gamma}{\omega_0}|\mathbf{A}(\mathbf{r},t|^2 \tag{4.6.47}$$

The second term, being the derivative of the complex conjugate of the amplitude, has no simple physical explanation but could be described as a dispersive four-wave mixing term [33]. Fig. 4.9 shows the effect of the intensity dependent group index. At high intensities the pulse propagates slower leading to a formation of an optical shock at the trailing end of the pulse.

4.6.7 Self-Focussing

As covered in chapter 4.4.3, the index of refraction becomes intensity dependent when the assumption of a harmonic electron potential breaks down. When a Gaussian light beam passes through an optical medium the refractive index changes by:

$$n(\mathbf{r},r) = n_0 + n_2 I(\mathbf{r},r) \tag{4.6.48}$$

Here, the intensity I is proportional to the square of the electrical field and n_2 is called nonlinear refractive index which depends on the optical medium the laser beam propagates in. The light travelling through a slab of glass (or an amount of gas) with a constant thickness will experience an increased optical path length depending on the intensity-profile of the beam. Therefore the Gaussian beam creates itself a lens under which the beam is focussed. The propagation equation in a solely nonlinear medium would take the form:

$$\frac{\partial}{\partial z'}\mathbf{A}(\mathbf{r}',\tau) = \left[\frac{i}{2k_0}\nabla_\perp^2 + i\gamma|\mathbf{A}(\mathbf{r}',\tau)|^2\right]\mathbf{A}(\mathbf{r}',\tau) \tag{4.6.49}$$

It is apparent that by integrating this equation the amplitude would acquire two phase terms. Diffraction (arising from the perpendicular gradient operator) counteracts nonlinear focussing through the Kerr-term. An interesting quantity is called critical power. It states when nonlinear self-focussing is greater than diffraction and therefore will inevitably lead to a beam collapse. In other words, the critical power is reached when the diffraction angle is equal to the self-focussing angle:

$$\theta_{sf} = \theta_{diff} \tag{4.6.50}$$

The diffraction angle of the first minimum is known to be:

$$\theta_{diff} = \frac{1.22}{2}\frac{\lambda_0}{n_0 d}. \tag{4.6.51}$$

In case of the self-focussing angle we can apply Fermat's principle which states that all optical path lengths from a wavefront to a focus have to be equal. As a beam propagating on the outside of the spot experiences the linear refractive index while another beam at the centre of the spot is propagating corresponding to the intensity dependent refractive index one can write:

$$(n_0 + n_2 I) f = n_0 f / \cos(\theta_{sf}), \tag{4.6.52}$$

hence

$$\cos(\theta_{sf}) = (1 + \frac{n_2}{n_0} I) \approx 1 - \frac{\theta_{sf}^2}{2} \tag{4.6.53}$$

$$\theta_{sf} = \sqrt{\frac{2n_2 I}{n_0}}. \tag{4.6.54}$$

Equalizing the two angles results in the value for a critical power

$$P_{cr} = 0.61^2 \frac{\pi \lambda_0^2}{8 n_0 n_2} \approx \frac{\lambda_0^2}{8 n_0 n_2}, \tag{4.6.55}$$

where the definition of the Power $P = \pi(d/2)^2 I$ was used. This critical power determines when nonlinear self-focussing and diffraction are balancing each other out. If the laser power exceeds the critical power the beam will inevitably collapse since the critical power does not depend on the beam diameter.

4.6.8 Plasma Interactions

Plasma will be generated when the laser intensity becomes so great, that either tunnel, or multi-photon ionisation leads to a build up of free electrons within the time of the laser pulse's duration. Multiple ionisation schemes were discussed in chapter 4.5.3 where the ionisation rate for multi-photon ionisation was stated. This allows the calculation of the amount of free charges with a rate equation of the type:

$$\frac{\partial \rho_e}{\partial \tau} = W_{mp} \rho_0 = \frac{2\pi\omega_0}{(l-1)!} \frac{I(\mathbf{r}, \tau)^l}{(\hbar \omega_0^2 \sigma_{mp})^l} \rho_0 \tag{4.6.56}$$

Here, ρ_0 stands for the density of neutral atoms, and ρ_e for the amount of electrons. This approximation stands only for as long as no secondary ionisations take place and the density of neutral atoms does not change considerably. In the latter case a set of equations could be integrated to find the amount of charges when the average ionisation of the gas reaches close to 1. Now, following the approach presented in [37], one could find that the interaction of the electromagnetic field with a plasma is governed by four primary effects:

$$S_{free} = S_{plasma} + S_{rel} + S_{wake} + S_{ion} \tag{4.6.57}$$

Here, S stands for "source term". The wake-field and relativistic term will be neglected since we are only interested in the propagation of extremely short laser pulses. These terms become only relevant at intensities higher than these found in our experimental conditions. The plasma term,

$$S_{plasma} = \frac{\omega_p(\mathbf{r}, t)}{c^2} \left(1 - \frac{\nu_e}{\omega_0}\right) A(\mathbf{r}, t), \tag{4.6.58}$$

with $\omega_p = 4\pi q^2 \rho_e / m_e$ and ν_e being the electron neutral collision frequency, describes a decrease in the refractive index leading to defocussing of the laser beam. The imaginary term on the other hand

is determining the effect of inverse bremsstrahlung [37]. It is easy to see how the focussing from the nonlinear refractive index can be opposed by the plasma generated by the laser pulse itself, leading to defocussing of the laser beam. Since the laser pulses will be very short, collisional effects by the electrons will most likely not influence the propagation of the beam. Additionally, the trailing end of the pulse will see a larger amount of free charges than the beginning. While the laser pulse ionizes the gas it travels in, it losses energy by ionisation. This is modelled by the term [37]:

$$S_{ion} = -8\pi i k_0 \frac{U_{ion}}{c} \frac{\partial n_e}{\partial \tau} A(\mathbf{r}, t). \tag{4.6.59}$$

Here, U_{ion} stands for the required ionisation energy. This implies the pulse will suffer the biggest losses when the ionisation rate is maximal. As seen earlier, this rate is proportional to the intensity to the power of l (with $l = \lceil U_{ion}/\hbar\omega \rceil$)

4.6.9 Split-operator Method (Split-Step Fourier Method)

The nonlinear Schrödinger equation is a nonlinear partial differential equation and thus cannot be solved analytically (with some exceptions). One principal method for solving these kinds of equations has emerged. This is the so called split-step Fourier method. It exploits properties of the Fourier transform to rewrite the source terms discussed above such that they can easily be integrated. In this chapter, the description from [28] will be used to discuss this method. Eq. 4.6.36 can be written in the form:

$$\frac{\partial A(\mathbf{r}, t)}{\partial z} = (\hat{D} + \hat{N}) A(\mathbf{r}, t) \tag{4.6.60}$$

where the term responsible for the intensity dependent group velocity was included while neglecting the term relevant for diffraction (we will come back to it later) such that:

$$\hat{D} = \sum_{n=2}^{\infty} \frac{1}{n!} k_n \left(i \frac{\partial}{\partial t} \right)^n \tag{4.6.61}$$

and

$$\hat{N} = i \frac{3\omega_0}{2nc} \left(\chi^{(3)} |\mathbf{A}(\mathbf{r}, t)|^2 + \frac{i}{\omega_0} \frac{1}{\mathbf{A}(\mathbf{r}, t)} \frac{\partial}{\partial \tau} \left[|\mathbf{A}(\mathbf{r}, t)|^2 \mathbf{A}(\mathbf{r}, t) \right] \right) \tag{4.6.62}$$

The propagation will be carried out in steps. After a step h the amplitude will have changed by:

$$A(z + h, t) = e^{(\hat{D} + \hat{N})h} A(z, t) \tag{4.6.63}$$

This is an exact solution of eq. 4.6.60. The Split-step method carries out the integration in two steps, a dispersion step and a nonlinear step:

$$A(z + h, t) = e^{\hat{D}h} e^{\hat{N}h} A(z, t) \tag{4.6.64}$$

Here an approximation was made. This can be made clear by the use of the Baker-Campbell-Hausdorff (BCH) formula [44]:

$$e^{\hat{D}h} e^{\hat{N}h} = e^{(\hat{D}h + \hat{N}h + \frac{h^2}{2}[\hat{D}, \hat{N}] + \frac{h^3}{12}([\hat{D}, [\hat{D}, \hat{N}]] + [\hat{N}, [\hat{N}, \hat{D}]]) + \ldots)} \tag{4.6.65}$$

which shows that the non-commutating nature of $\hat{D}$ and $\hat{N}$ has been neglected. The size of the commutator will therefore determine the accuracy of this approach while a smaller step size will

also decrease the errors made in each step. The Linear operator will be evaluated in the frequency space:

$$A(z+h,t) = \mathcal{F}^{-1} e^{\hat{D}(\omega)h} \mathcal{F} e^{\hat{N}h} A(z,t), \tag{4.6.66}$$

because this allows for the usage of eq. 4.6.21 to easily evaluate the dispersion step. Due to the properties of the Fourier transform by which one can replace $\frac{\partial}{\partial \tau}$ by $i\omega$ the dispersion term is as simple as adding a spectral phase corresponding to the material dispersion in the optical medium over the distance h. When only self-phase modulation would be considered then even the nonlinear operator would reduce to a temporal phase. In combination with the fast Fourier transform algorithm (FFT) these simulations can be carried out reasonably fast. The accuracy of this method can be increased by using a symmetric approach:

$$A(z+h,t) = e^{\frac{h}{2}\hat{D}} e^{\hat{N}h} e^{\frac{h}{2}\hat{D}} A(z,t), \tag{4.6.67}$$

which reduces the error arising from the non-vanishing commutator to the order of h^3 [28].

4.7 Optical Fibres

Optical fibres are known to be the backbone of the modern day communication infrastructure. They are used to transmit increasing amounts of data in the form of pulsed light over long distances without significant losses. Besides that, they find further application in medicine (endoscopes) and even laser systems which rely on optical fibres as cavity or lasing medium. Therefore, it is important to understand and explore the fundamental properties of optical fibres. One distinguishes between different types of optical fibres which rely on different methods of beam confinement.

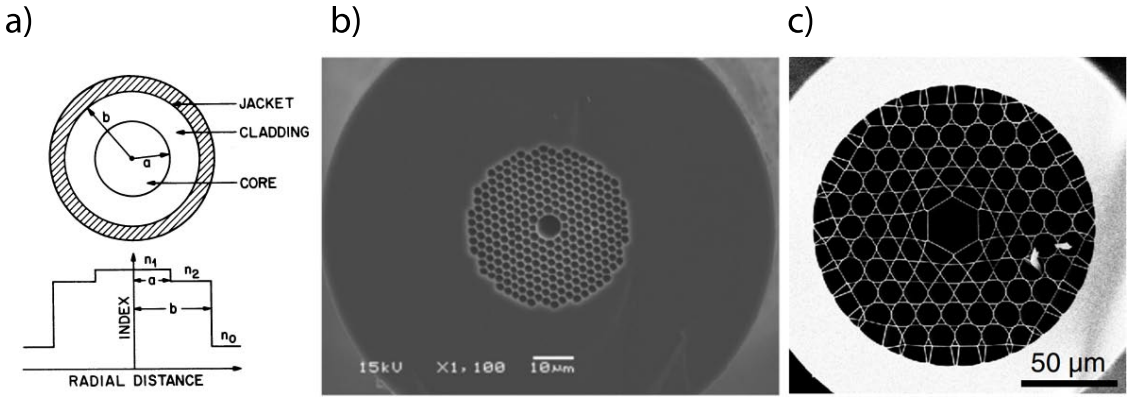

Figure 4.11: Comparison of three different optical fibres. a) Step-Index, b) Hollow-Core and c) Kagomé

Step-Index Fibres

Step-index fibres are the most common type of fibre and are made out of a core and a cladding material. As depicted in Fig. 4.12 the core of a step index fibre has a greater index of refraction than the cladding. Note: A jacket is only used to protect the glass from being damaged by reducing the stress when the fibre is bent. In these fibres, the beam-confinement is based solely on total internal reflection which occurs when a beam of light hits the boundary of two regions with different index of refraction at an angle bigger than the critical angle [45]:

$$\theta_c = \arcsin(\frac{n_2}{n_1}) \tag{4.7.1}$$

for which $n_2 > n_1$. This angle occurs when a beam coming from the lower refractive index medium would be refracted to an angle greater than $90°$ which can easily be found using Snell's law. From this it is clear that if a glass fibre is bent, certain modes will be coupled out of the core. This can lead to losses. Another limiting property of these classic fibres is the glass itself. Dispersion and nonlinear effects can lead to distortions of pulses or transmitted signals, limiting the achievable data rates or intensities. Besides chromatic dispersion, optical fibres introduce another type of dispersion called modal dispersion. Different modes with different wavevectors k will propagate the fibre at $v_{ph} = \frac{c}{n} = \frac{\omega}{k}$. A mode with a perpendicular wavevector $k_x, k_y > 0$, thus $k = \sqrt{k_x^2 + k_y^2 + k_z^2}$ will therefore travel slower than a mode for which $k = k_z$. Therefore, fibres are often designed as single-mode fibres such that only one mode can be transmitted without significant losses.

Hollow-Core Fibres

Hollow core fibres differ profoundly from step index fibres. They consist of an optical lattice with a big central hole. The lattice is surrounded by a cladding which does not play a role in the beam confinement as it does for other fibres (see Fig. 4.12 b). Hollow-Core Fibres (HCF), which are a subgroup of Photonic crystal fibres (PCF) rely on a band-gap for the guidance of the light [46]. This band-gap is formed when reflections from different surfaces surrounding the central core interfere destructively for light trying to escape (certain k_x, k_y), thereby confining the light to the fibre-core. Simulations like the ones carried out in [47] are required to find the allowed modes of a PCF. All hollow fibres share the advantage that nonlinearities and dispersion are extremely low. Some fibres were designed to achieve anomalous dispersion (GVD $< 0 fs^2/m$). In other applications, a gas filled central core, in conjunction with the high intensities confined at the centre, are used for efficient high harmonic generation [48].

Kagome Fibres

Just recently, another type of fibre has been developed. It features extremely low chromatic dispersion as well as very low nonlinearities, which is beneficial in high intensity applications. Due to its properties it is a promising tool for super continuum generation. Especially, since it has a very low impedance on a broad wavelength range. In Raman-Scattering schemes it was demonstrated that the exciting light as well as the scattered light could be found propagating in the same fibre, significantly simplifying the experimental setup [49, 50]. In contrast to HCF's, Kagome fibres rely on a different principle of light guidance. While HCF's feature full band-gaps which trap the light of certain wavelengths, Kagome fibres offer band-gaps only at certain azimuthal angles [51]. This allows them to transmit a wider spectral range at the cost of higher losses. The guidance principle is currently not fully understood but is supposed to be related to "anti-resonant reflection optical waveguiding" [51].

4.8 Optimization Algorithms

Optimization algorithms are inherently important for coherent control experiments because of the vast number of parameters to explore when trying to control fluorescence, ionisation or photodissociation. In the course of this thesis two different optimization methods were employed.

4.8.1 Genetic Optimization

Genetic optimizations (GO), a specialization of evolutionary algorithms (EA), are based on the principles of mutation and selection in biology. These algorithms are efficient in optimizing a large parameter set despite comparatively large noise. Unfortunately, it is difficult to obtain a value indicating the optimization's convergence and they tend to converge in local minima. Genetic algorithms encode parameters in a "gene" or an "individual". By evaluating the parameters, each individual of a generation can be assigned a "fitness" which needs to be optimized. The function which defines the fitness has to be selected carefully to match the aim of the optimization. It can be based on experimental results or be a direct function of the parameters in a simulation scheme. Starting from a generation of individuals, four steps are used to find a surpassing (optimized) generation. These steps will be iterated until a termination criterion is reached.

I **Evaluating the fitness**
The fitness function and/or an experiment is used to evaluate the fitness of each individual.

II **Elitism (optional)**
The best individual (or more) is selected and used in the next generation without alteration. The rest of the generation is filled by mutation or crossover from the previous generation:

III **Mutation**
Parameters p_i will be mutated with a certain probability. The mutated parameters are calculated via $p_i' = p_i\, rnd(-1,1)\mu_p$, where μ_p is the mutational parameter and $rnd(-1,1)$ is a random number in the range of -1 to 1.

IV **Crossover**
Crossover takes care of convergence of the population: Two parents are selected (favourably with a high fitness) and children are generated by randomly selecting genes from either parent.

Crossover and mutation counteract each other and the number of individuals used for either process has to be fine tuned depending on the number of parameters and the problem at hand. Convergence is furthermore controlled by the change of the mutational parameter μ_p and the mutation probability. For low mutation parameters convergence by crossover will dominate and will result in an overall convergence. A high mutational parameter on the other hand spreads the parameter space the generation occupies. A widespread method to determine μ_p is the "1/5th rule", first formulated by Rechenberg [52]. It states that when 1/5th of the population has increased their fitness from one iteration to another one shall increase the mutational parameter by a factor. When this criterion is not reached, the mutational parameter shall be reduced. This leads to an increased search space when better fitness can still be achieved and convergence when the optimum is found.

4.8.2 Phase Resolved Interferometric Spectral Modulation

The PRISM algorithm (phase resolved interferometric spectral modulation) is based on the intrapulse interference of spectral components in a non-linear detector. By optimizing the non-linear

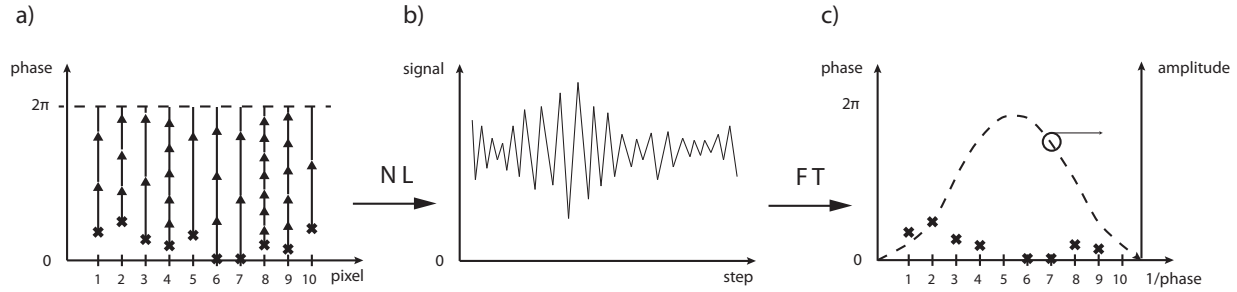

Figure 4.12: Illustration of the PRISM algorithm. a) Each pixel is assigned a step size. Every measurement step, each pixel's phase is increased by the step size and the non-linear signal measured b). The non-linear signal shows a beating pattern. A Fourier transform reveals the phase of each frequency component (=step size) which can be used to precompensate the phase and generate a transform limited pulse at the position of the detector.

(e.g. multiphoton excitation), PRISM can be used to find transform-limited pulses (i.e.: an offset phase function) at the place of detection. The algorithm functions as follows: Each pixel to be optimized is assigned a different step size. For each step, the phase of all pixels is increased by this step size and the non-linear signal is measured. By interference of the spectral components a pulse is formed which varies in intensity depending on the current phase applied by the pulse shaper. In the process of increasing the phase of each of the pixels at a different rate, the non-linear signal will experience a beating pattern at the frequencies corresponding to the step sizes. Hence, when a Fourier transform of the measured non-linear signal is calculated, each pixel can be assigned a frequency of the Fourier transform. The phase of the Fourier transform for each frequency (which can be linked to a single step size and thereby a single pixel) is equal to the phase offset each wavelength experiences from the shaper up to the detector, plus the phase offset which was present before the pulse shaping setup. This offset can be used to pre-compensate all dispersion and to create a transform limited pulse at the place of detection.

Experimental Setup

5

5.1 Laser Systems

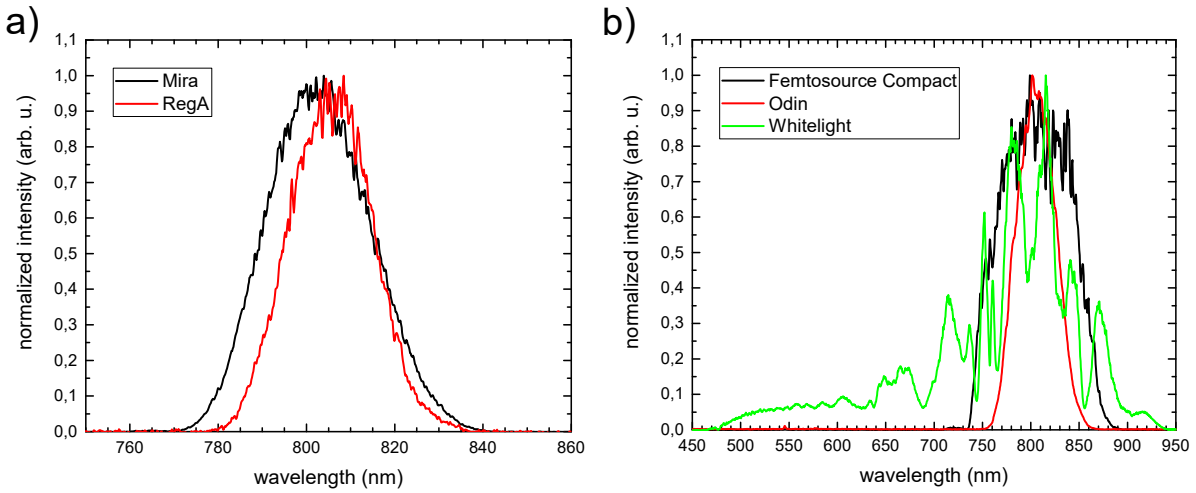

Figure 5.1: Comparison of the spectra generated by the various laser sources used in the experiments for this thesis. a) Available spectra with the Mira and the RegA setup. b) Oscillator, amplifier and white-light spectrum which was generated by filamentation.

Two separate laser systems were used in the experiments conducted for this thesis. The first is a system by Coherent (Mira, RegA) and relies on a regenerative amplifier as it features pulse energies in the order of μJ, a central wavelength of $805\,nm$ and a repetition rate of $286\,kHz$. The second laser system was used during filamentation experiments and consists out of a Femtosource Compact (Spectra-Physics) Oscillator and an Odin multipass amplifier. It operates at a lower repetition rate of $1\,kHz$ but can generate, in its current state, pulses with the energy of $\sim 0.6\,mJ$ at a central wavelength of $800\,nm$ and a spectral bandwidth of $80\,nm$ FWHM.

5.1.1 Mira Oscillator

The Mira Oscillator is a typical Ti:Sapphire femtosecond oscillator manufactured by Coherent Inc. It is pumped by a Verdi Nd:YVO4 solid state laser, which can output 5W at $532\,nm$ (frequency doubled). The pulse generation of the Mira oscillator is based on the previously discussed Kerr-lens modelocking technique. An adjustable aperture is situated in the cavity just before the out-coupling mirror. A pair of prisms is used to compensate for the dispersion introduced by all other elements that make up the cavity. A pair of oscillating mirrors is used to start mode-locking by introducing random fluctuations. The Mira oscillator typically puts out a power of $700 - 800\,mW$ at a repitition rate of $76\,MHz$, which corresponds to an energy per pulse of $\sim 10\,nJ$. The spectrum can be tuned from $750\,nm$ up to $820\,nm$ and the spectral bandwidth can be adjusted by the dispersion compensated in the prism compressor. A broad range of spectral bandwidths, from $22\,nm$ up to $38\,nm$, can be selected. In most experiments, the oscillator was tuned to $\lambda_0 = 805\,nm$ and $\Delta\lambda = 28\,nm$ (Fig. 5.1 a).

5.1.2 RegA 9000 amplifier

Pulses generated by the oscillator can be amplified with the help of a regenerative amplifier (RegA 9050, Coherent). Before the pulses enter the amplifier, they are stretched by a grating compressor so that they do not risk to damage the lasing medium. Intensities of amplified transform limited pulses would rapidly reach the damage threshold of the Ti:Sa crystal. This method is called Chirped pulse amplification (CPA) and is used in nearly every pulse amplification schemes nowadays. The stretched pulses entering the RegA get injected into the cavity by a acousto optic modulator. Since the amplifier operates at a significantly lower repetition rate a divider selects each $\sim 280th$ pulse from the $76MHz$ pulse train. For injection, a standing wave is induced in the acousto optic modulator which acts as a grating, refracting the incoming pulse into the cavity. A double refraction scheme is used to maximize the efficiency injection [53]. The cavity is set up similar to the oscillator cavity, although the amplifier does not require an aperture and a pair of oscillating mirrors. A (Millenia-X, Spectra Physics) Diode laser is used for pumping of the Ti:Sa crystal. The pump laser uses a Nd:YVO_4 gain medium and can reach a power of 10W. The amplifier features an additional Pockels-Cell in the beam line which prevents self-lasing by acting as a variable absorbing medium. The pockels-cell blocks the beam except for a selected time window in which the pulse is amplified. Careful tuning of this time window is fundamental for efficient amplification. Amplified pulses show narrowing in their spectral width to $24\,nm$ from previously $28\,nm$ (Fig. 5.1 a). The repetition rate is now significantly lower ($286\,kHz$) than that of the oscillator but results in pulses with up to μJ in pulse energy. A grating compressor completes the CPA-scheme which compresses pulses back to $\sim 60\,fs$.

5.1.3 Femtosource Compact

The oscillator used in the whitelight setup is a Femtosource Compact manufactured by Spectra-Physics. It is a "turn key" system which should require minimal calibration from day to day. Unfortunately, stability was a problem when the system heated up such that the pump beam had to be realigned continuously for 3 hours until the system was thermalised and would not fall out of mode-lock. Mode-locking is again achieved by exploiting the Kerr-effect. Two focussing mirrors around the lasing medium are positioned to be slightly out of focus in cw and in focus in the nonlinear regime. Tuning the distance of these two mirrors can influence the stability of the mode-locking regime (By tuning the losses of the cw cavity). Just like in the Mira system the lasing medium is a Ti:Sa crystal which is pumped by a 5W frequency doubled Nd:YVO_4 solid state laser (Verdi). The oscillator generates a spectrum centred at $805\,nm$ and a spectral width of $90-100\,nm$ FWHM (Fig. 5.1 b). The pulse energy is at approximately $5\,nJ$ at the repetition rate of $75\,MHz$. Just behind the oscillator an infrared diode is used for syncing the Pockel's cell used in the amplifier to the pulses generated by the oscillator. A Faraday isolator, positioned between oscillator and amplifier, ensures that no reflexes return from the amplifier which could disturb the operation of the oscillator.

5.1.4 Odin Multipass Amplifier

The Odin Multipass amplifier (Quantronix), which also uses a Ti:Sa crystal as gain medium is pumped by a $10\,W$ YLF-type gas laser. The seed pulses which come from the Faraday isolator are stretched to about $50\,ps$. Then, each 75.000th pulse is selected by a Pockel's cell. It's voltages are driven by a Pockel's cell driver (Medox Electro-optics, Inc.). Pulses, now at a repetition rate of $1\,kHz$ are amplified by passing the Ti:Sa crystal 8 times and meanwhile increase their energy

$\sim$100,000-fold. The output bandwidth decreases slightly in the amplification process and is usually in the range of $50 - 60\,nm$ FWHM (Fig. 5.1 b).

5.2 Pulse Shaper

Different temporal pulse shaping setups were employed during the course of this thesis. While different types of pulse-shapers exist (micro-mirror, acousto optic), only liquid-crystal modulators were used in the conducted experiments. Thus the focus will lie on the technical aspects of liquid-crystal type modulators.

5.2.1 SLM640

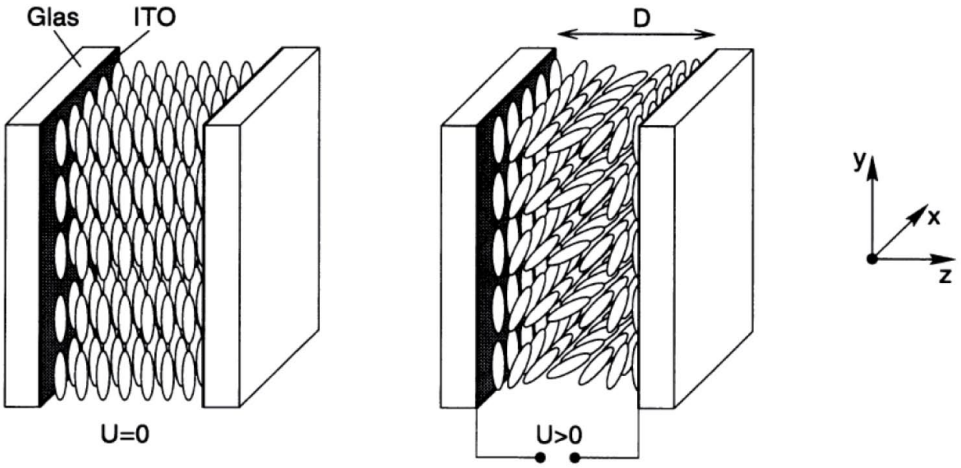

Figure 5.2: Schematic view of a liquid crystal cell. when a voltage is applied to the electrodes on both sides of the cell, the polar crystals turn. This reduces the refractive index along the y axis leading to a change of phase retardation. This image was taken from [22]

The pulse shaper used for temporal pulse shaping is a $SLM640$ two-array, 640 pixel liquid crystal SLM manufactured by CRI. It is now sold by another company (Meadowlark Optics, Inc.). Each linear array of pixels has a width of $98\,\mu m$. Between the pixels there is a gap of $2\,\mu m$. The insides of the LC cells are brushed so that the LC molecules align in a given direction when no electrical field is applied. The front and back of each pixel is covered by a transparent cathode and anode. The liquid crystal molecules turn according to the external field when a voltage is applied. This is due to the polar nature of the LC molecules. Besides their polarity they are birefringent, which results in a refractive index change when the molecules turn. The inside of both arrays are brushed orthogonally to each other (at plus and minus $45°$ with respect to the laser table). Hence, when applying a voltage, the phase of both perpendicular polarization components can be altered independently. For this, the relationship between voltage and phase retardance has to be calibrated, which will be addressed later in the experimental part of this thesis. The SLM sits in the centre of a dispersion free 4f-compressor. In this Fourier plane, each wavelength is linearly separated and focussed by a combination of a grating (Setup A: 1200 lines/mm, Setup B: 300 lines/mm) and a cylindrical lens (Setup A: $f = 25\,cm$) or a cylindrical focussing mirror (Setup B: $25\,cm$). For correct parametric pulse shaping, the relationship between pixels and wavelength has to be known. Calibration carried out each day, ensured that pixel 321 matched the central wavelength

	GDD (fs^2/m)	TOD (fs^3/m)
fast-axis	$-7.5 \cdot 10^3$	$4.1 \cdot 10^5$
slow-axis	$7.5 \cdot 10^3$	$7.3 \cdot 10^5$

Table 5.1: Dispersion of the Hollow-Core fibre as measured in [13]

of the spectrum ($805\,nm$). The spectral resolution was not subject to change and was only once calibrated to be $0.272\,nm/px$.

5.2.2 Hollow-Core Fibre

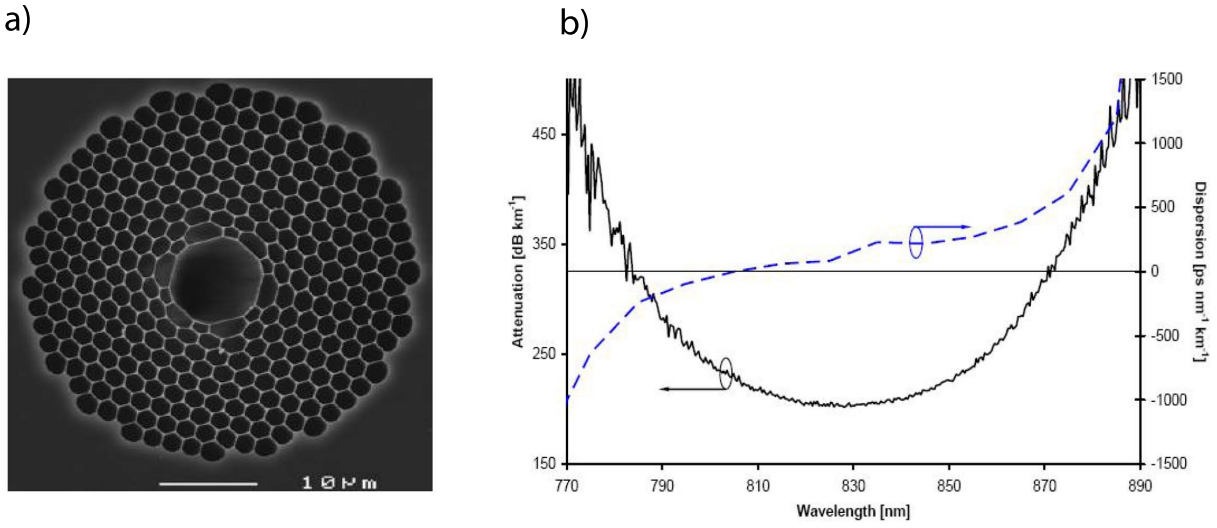

Figure 5.3: a) Here the Core of a type HC-800-01 photonic crystal fibre is shown. b) Transmission is allowed in a window of about $70\,nm$ centred around 830nm. It can be seen that the GDD (the slope of the dispersion) is smallest at $830\,nm$ as well. This image was taken from [54]

The Hollow-Core Fibre used in the experiments is of the type (HC-800-1) and was acquired from Blaze Photonics (now NKT Photonics). It features a central hollow core with a diameter of about $9.2\mu m$ which is surrounded by a series of smaller holes. These form the optical band-gap needed for beam confinement. Its attenuation (see Fig. 5.3) allows propagation of wavelengths from 795 to $865\,nm$ without significant loss. In this region the GDD of this fibre is pretty small. The value of TOD has to be assumed to be comparably large. The dispersion of the fibre is listed in Tab. 5.1. The fibre has a total length of $110\,cm$ and was shipped with two collimating optics on either end which are encapsulated in two (FC/PC) plugs. Additionally, the fibre has a thin window on both end-faces which keeps dust from entering the hollow cores. This has proven to be a problem for unattenuated amplified pulses, which were able to damage the entrance window. This required the fibre to be serviced by the supplier once.

5.2.3 Kagome Fibre

The second fibre used in the experiments is a Kagome fibre (PMC-PL-780-USP from GLOphotonics). The optical lattice which forms the kagome fibre is depicted in fig. 5.4 (a). Its inner core

has a diameter of 50 to 70 μm depending on the optical axis. The maximum allowed pulse energy, as stated by the manufacturer is $50\mu J$ at a pulse length of 200 fs [55]. The fibre will break if bent to a radius lower than 10 cm but transmission losses increase already significantly when the fibre is slightly bent to a radius of $\sim$ 50 cm. As the fibre-core is not sealed, an entrance cap was built to keep dust from entering the fibre. This fibre is especially useful for high intensity ultrashort and broadband applications, since it features low dispersion and low attenuation over a significant wavelength range (see fig.5.4 (b)). Its dispersion was measured by calculating the difference of the phase required to form a TL-pulse before and after the fibre. This difference of both compensations resulted in a effective GVD of $-116\, fs^2/m$ and TOD of $2000\, fs^3/m$. These values are extremely low and represent nearly undisturbed propagation of ultrashort pulses.

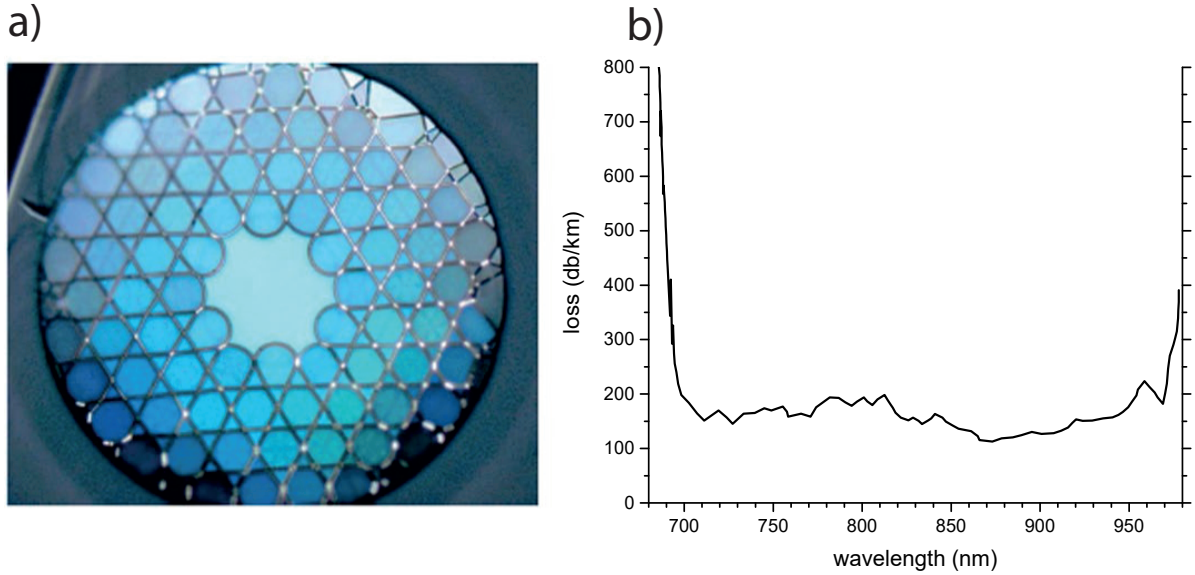

Figure 5.4: a) Core of the PMC-PL-780-USP Kagome fibre. The inner core diameter is 50 or 70 μm large, depending on the axis. b) The fibre allows efficient propagation over a broad spectral range. [55]

5.3 Pulse Characterization

Pulse characterization can be carried out in either the temporal or spectral domain. It is relatively easy to determine pulse characteristics using a pulse shaper and a spectrometer [56] via the spectrum and the spectral phase. Pulse characterization in the temporal domain is more difficult because of the extremely short timescales involved. Two time-domain approaches will be dicussed in this chapter.

5.3.1 Cross and Autocorrelators

Cross and autocorrelators rely on a short (ideally TL) laser pulse to probe a "signal" pulse. A delay between both pulses is scanned and a nonlinear signal that depends on the interference between both pulses is measured. An autocorrelation in contrast to a cross correlation, uses the same pulse as probe and signal pulse, which introduces limitations but significantly simplifies the setup. A cross correlator setup, made up from a BBO (type 2) crystal, lenses and a photomultiplier was setup earlier by the scientific group. Besides that, two autocorrelators (PulseCheck, NIR/IR-KTP)

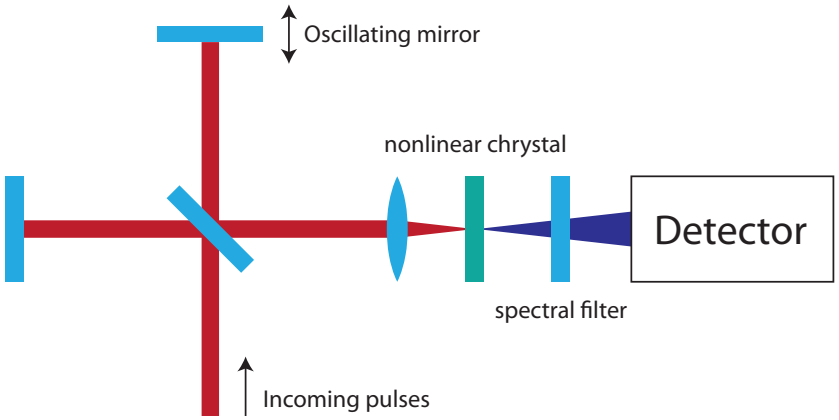

Figure 5.5: Illustration of an autocorrelator setup.

manufactured by (A P E GmbH) were used to quickly determine the pulse lengths at different positions in the setup. It can be easily set up to scan ranges from $150\,fs$ to $15\,ps$ with a minimal resolution of $1\,fs$ in the spectral range from 750 to $1100\,nm$. In the course of this thesis a data link was established to download measurements to the computer and automate data acquisition.

5.3.2 TG-FROG

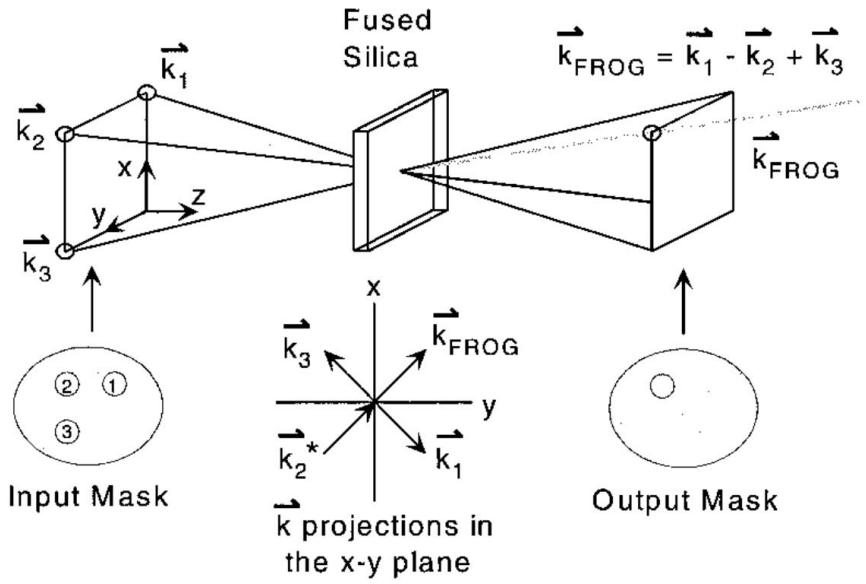

Figure 5.6: This image shows an illustration of the TG-FROG setup used to characterize WL-pulses in this thesis. A nonlinear four-wave mixing process generates a phase matched beam k_{frog} which is analysed with a spectrometer. Since all beams experience the same dispersion, extremely short pulses can be measured. Note that this illustration shows the nonlinear material to be Fused Silica, while BK7 was used in the experiments in this thesis. This illustration originates from [57]

In 1999 Li et. al. described a variant of the TG-FROG (transient grating - frequency resolved optical gating) which would be able to measure extremely short pulses [57]. This is possible because a degenerate four-wave mixing process is used that is inherently phase matched over a

broadband spectrum which is usually difficult to achieve in classical correlator schemes. The temporal resolution of a pulse-characterizing setup, which does not use a TL reference pulse, is limited by the difference in dispersion the beams experience. The TG-FROG uses an aperture, not a beam splitter, and a focussing mirror to create three separate beams. This enables the measurement of extremely short pulses. The beams are focused with a focussing mirror ($250\,mm$) into a thin slab of BK7, while one beam is delayed by the means of a computer controlled translation stage (PLS-85, MICOS). The resulting beam K_{FROG}, created by degenerate four-wave mixing is selected by an aperture behind the focus and measured by a spectrometer (USB2000, Ocean optics). Beam K_1 in Fig. 5.6 is delayed with respect to beam two and three. Thus, the output signal is given by the formula [57]:

$$I(\omega,\tau) \propto \left| \int_{-\infty}^{\infty} E_1(t-\tau)|E_2(t)|^2 e^{i\omega t} dt \right|^2 \tag{5.3.1}$$

The setup used in the course of this thesis was built and characterized by Schmidt et. al. [58].

5.4 Fluorescence Detection

Fluorescence experiments were carried out with varying focal lengths. Different lenses were used to focus the beam in order to reach intensities required for the examined multiphoton process. The dye was kept as a solution in a $10\,mm$ by $10\,mm$ quartz cuvette. Fluorescence was detected with a spectrometer or photomultiplier tube situated after two large collimating lenses (CaF). The beam was set up to be focussed close to one of the sides of the cuvette so that reabsorption effects of fluorescence propagating in the cavity would be minimized (Rhodamine B shows strong reabsorption which can shift the observed fluorescence spectrum to longer wavelengths). With the help of spectral filters (BG38, BG39, Schott) the exciting IR light was blocked. The intensity of L-Tryptophan fluorescence was not sufficient to be detected via the spectrometer. Therefore, a photomultiplier tube was used in conjunction with an UG11 filter to separate the light originating from L-Tryptophan fluorescence.

5.4.1 Rhodamine B

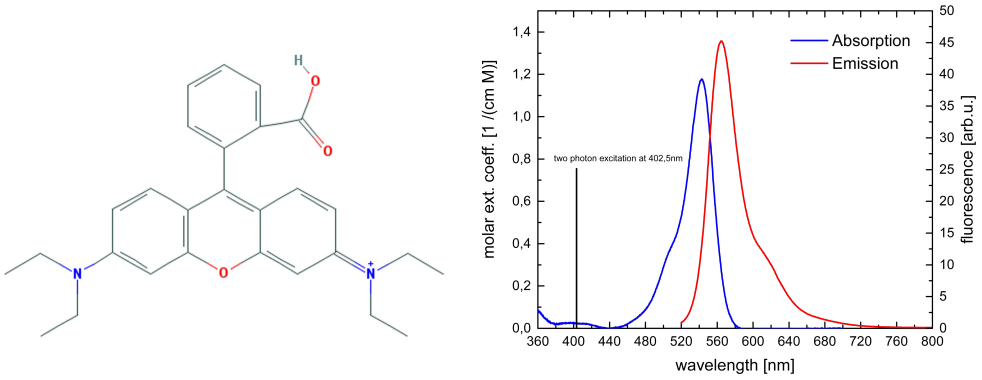

Figure 5.7: (left) Molecular structure and (right) emission and absorption spectra of Rhodamine B. Structure:[59], Spectral data: [60].

Rhodamine B (spectroscopy grade, Sigma-Aldrich) is a well known fluorescent dye. It is used as marker substance in microscopy and has once been used as food colouring. Its emission and absorption spectra are overlapping which can lead to reabsorption which in turn can shifts the observed spectrum to longer wavelengths. Rhodamine B is an extremely efficient dye. Excitation by two photons with a wavelength of $805\,nm$ yields sufficiently strong yellow fluorescence to detect it easily with a spectrometer. In the conducted experiments it has been solved in ethanol and sometimes glycerine in varying concentrations. When illuminated with high powered pulses Rhodamine B photobleaching was observed, which over time lead to decreased fluorescence of the samples. This was especially relevant when glycerine was used as solvent since “fresh” molecules cannot easily replenish the volume of the laser focus. Two-photon excitation cross-sections of Rhodamine B and other fluorescent dyes were measured using a tunable Ti:Sa laser by Xu and Webb [61]. Fig. 5.7 shows the structure of Rhodamine B as well as its one photon absorption and emission spectrum.

5.4.2 Coumarin 1

Coumarin 1 (also known as Coumarin 460 and Coumarin 47) is a derivate from the basic Coumarin which can be found in many plants. Although it is not equally efficient as Rhodamine B, its blue

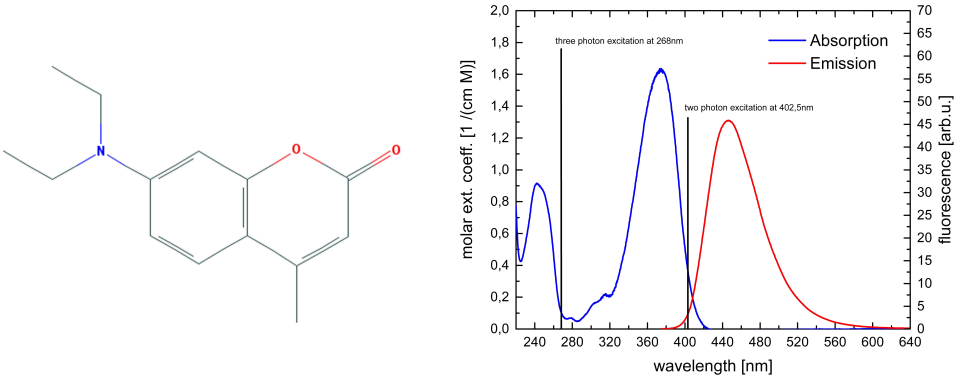

Figure 5.8: Molecular structure of Coumarin 1. Structure:[59], Spectral data: [60].

fluorescence can still easily be detected by a spectrometer. Its quantum efficiency is especially big in unpolar solvents. Additionally, it was found that polar solvents have a red-shifting effect on the emission spectrum of various Coumarin derivatives. Extensive studies regarding this aspect can be found in [62]. Fluorescence and absorption do not favour strong reabsorption and bleaching was not observed. Two-photon excitation with light at $805\,nm$ will target the flank of the absorption curve (see Fig. 5.8). This means that tuning the two-photon excitation spectra will have a non-trivial influence on the excitation efficiency of Coumarin 1. It has to be noted that the spectra shown in Fig. 5.8 are one-photon spectra. Two-photon excitation follows different selection rules which implies these curves are not totally accurate. Two-photon absorption spectra are difficult to obtain but it can be assumed that two-photon absorption in large molecules can be approximated by one-photon absorption.

5.4.3 L-Tryptophan

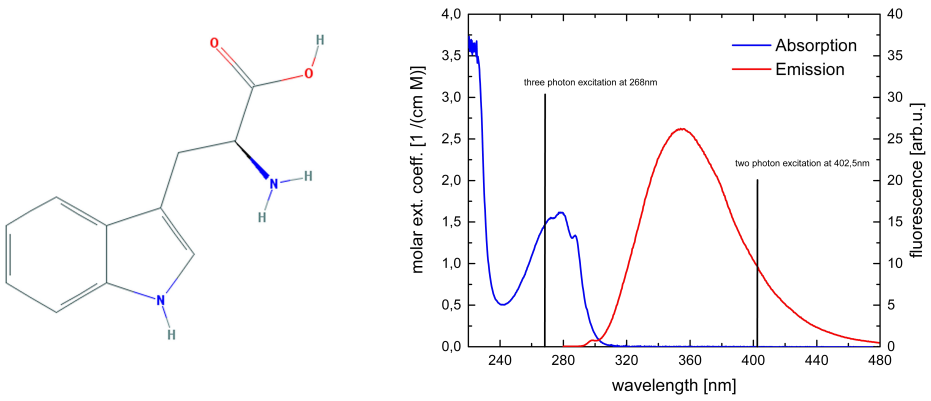

Figure 5.9: Molecular structure of L-Tryptophan. Structure:[59], spectral data: [60].

L-Tryptophan (Sigma) is one of the essential amino acids required for human life. Together with Tyrosine, and Phenylalanine it is detectable by fluorescence without any additional marker substance. Tryptophan absorbs UV light and thus can be excited by three-photon excitation with a Ti:Sa laser. The blue fluorescence was primarily detected with the help of a photomultiplier tube and spectral glass filters. This enabled measuring the excitation efficiency of Tryptophan for pulses other than the most efficient transform limited pulse. Tryptophan has always been solved in distilled water in concentrations of 15mM in v.e. water.

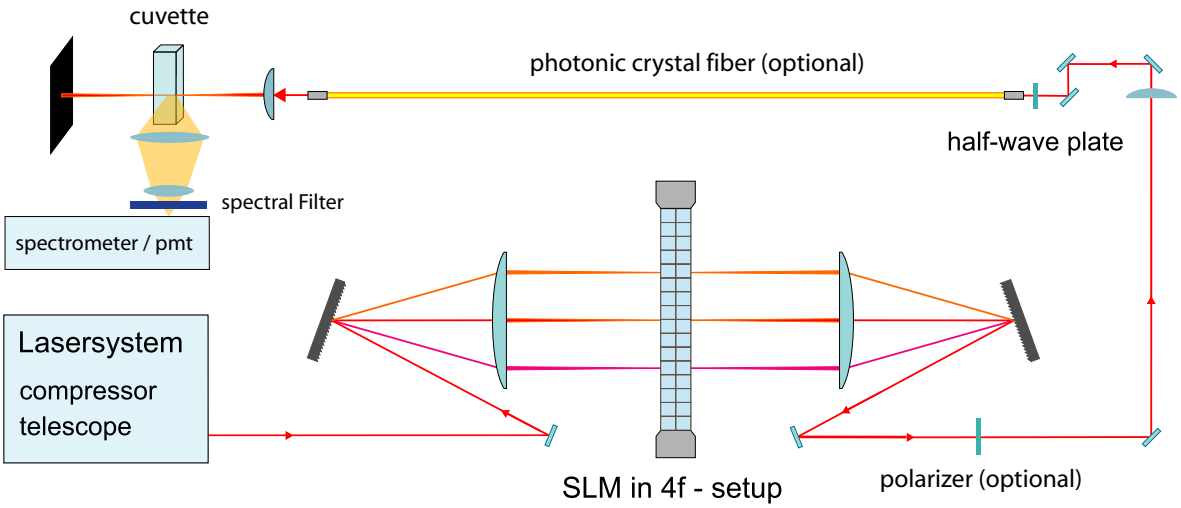

Figure 5.10: Experimental setup used in the fluorescence experiments including Rhodamine B and Coumarin 1. For the experiments with L-Tryptophan amplified pulses were used and the fibre was taken out of the experimental setup.

5.5 Setup A - Fluorescence Experiments

The experimental setup which was used in the fibre and fluorescence experiments is quite modular and was adapted to suit the performed experiments. This chapter will try to outline the capabilities of this first setup on the basis of the previously described devices and methods. Laser pulses are generated in the Mira Oscillator (5.1.1) and can be amplified by chirped pulse amplification with a subsequent regenerative amplifier (5.1.2). Amplified pulses have an energy of up to $1\mu J$ while oscillator pulses are in the order of $\sim nJ$. The pulses which can be characterized by an autocorrelator 5.3.1 then enter the pulse shaping setup (5.2.1). Here, depending on the experimental requirements, it was chosen between two setups. The two liquid crystal arrays, which are placed in the Fourier plane of a dispersion free 4-f compressor, can be used to either control phase and amplitude of an incoming horizontal polarized laser pulse or control the phase of two perpendicular polarization components separately. For the latter, waveplates were added to rotate both shaped polarization components from $\pm 45°$ to $0°, 90°$ just after the LC arrays. This is necessary because the polarization-dependent reflectivity of the gratings would stretch the polarization state and thereby change the angle between both polarization components. This waveplate ensures that both polarization components stay perpendicular. On the downside, this introduces intensity differences between the vertical and horizontal component. These were ruled out by another waveplate in front of the pulse shaping setup, splitting the intensity on the two arrays unevenly, thus precompensating for the grating losses. Both liquid crystal arrays were calibrated prior to the experiments. The liquid crystals will align along the brushed inside of the cells when no voltage is applied. At maximum voltage, however, all liquid crystals will be aligned along the beam's propagation direction. This ensures that at maximum voltage the phase retardance can assumed to be constant. For calibration, one array is kept at this maximum voltage, the other's voltage is lowered which increases the retardance on that polarization component. A polariser and a power meter, set up after the shaper, can be used to monitor the polarization change on horizontally polarized incident light. This is then used to create the calibration lookup table required for further operations. Fur-

thermore, the SLM was positioned such that pixel 320 was in line with the central wavelength of the spectrum ($805\,nm$). The wavelength resolution was found to be $0.2716\,nm/px$. The pulses can then be transmitted through a hollow-core photonic crystal fibre (5.2.2) or Kagome fibre (5.2.3) for which a telescope was used to adjust the diameter of the beam. The overlap of the beam with the fibre mode determines how much light can be coupled into the fibre. Beam alignment had to be optimized every day with the help of a photodiode on the back side of the fibre as reference. Even though photonic crystal fibres are designed to allow much higher pulse intensities than conventional optical fibres the laser power was reduced to 60 mW when using amplified pulses to avoid damage to the front window of the hollow-core fibre. After the fibre, the beam diameter was widened by a telescope and then focused into a cuvette filled with the sample solution. Finally, two lenses placed on an axis perpendicular to the exciting laser beam captured as much fluorescent light as possible to be analysed by a (OceanOptics) spectrometer. The spectrometer data can be evaluated by a program and be used as feedback for e.g.: closed loop optimizations or to test different parametric phase functions on their efficiency in exciting one or more dyes selectively.

5.6 Setup B - Whitelight Laser Setup

The laser system used for the experiments on laser filamentation in Argon and Krypton differs significantly from the system described in the preceding chapter. This setup is capable of generating few-cycle, white-light laser pulses in a two stage filamentation scheme. First, pulses are generated by a Ti:Sa oscillator (5.1.3) and then amplified in a multipass scheme (5.1.4). A Faraday isolator (optical diode) in between the oscillator and the amplifier ensures that no backreflections disturb the mode-locked oscillator. The amplifier selects pulses at a rate of $1kHz$ and amplifies them during eight passes through a Ti.Sa crystal. The amplified beam intensity is reduced using a circular aperture to optimize the spectral broadening by the following two filamentation stages. A power of $490\,mW$ was found to optimize the whitelight spectrum (i.e.: least modulations in the spectrum, maximal broadening). This corresponds to a pulse energy of $490\mu J$ prior to the first filament. The first filamentation stage is composed of a focussing mirror $f = 2\,m$, a collimating mirror $f = 2.5\,m$ and a acrylic glas tube to minimize beam pointing fluctuations. It broadens the spectrum coming from the amplifier to a spectral width of $\Delta\lambda \sim 100\,nm$. The dispersion that laser pulses acquire in this first filament is compensated for with a pair of broadband chirped mirrors ($700 - 900nm$, Layertec). Each reflection on one of the chirped mirrors linearly chirps the pulse by $-30\,fs^2$. Pulses are compressed to a pulse length of $15fs$ [63] which is necessary for white-light generation during the second filamentation stage. Then, a second filamentation is used to further broaden the laser spectrum to the octave spanning spectrum which is shown in Fig. 5.12 (b). Here, filamentation is triggered by a $f = 1.5\,m$ focussing mirror, while a $f = 1.25\,m$ is used for collimating the beam before a second pair of chirped mirrors ($\sim -20\,fs^2$ per reflection) is used to compensate for most of the chirp induced in the filament. Pulses have a broadband spectrum at this point of the setup, which is why dispersion cannot be solely compensated for by linear chirp. High order dispersion comes into play which has to be compensated using pulse shaper. The beam enters the pulse shaping setup (a folded 4f compressor) which uses cylindrical focusing mirrors ($f = 25\,cm$) instead of lenses. This is important since lenses would induce chromatic aberration which would lead to strong spatial chirping of the outgoing beam. The pulse shaper sits in the Fourier plane of the 4f setup (5.2.1). The compressor uses two gratings with $300\,\text{lines}/mm$ which are blazed at $600\,nm$. A wire grid polariser (Edmund Optics) can be used after the pulse shaping setup to enable amplitude and phase modulation of the entire white-light spectrum. Each day, the setup was calibrated using two apertures in front and in the back of the setup. Additionally, the

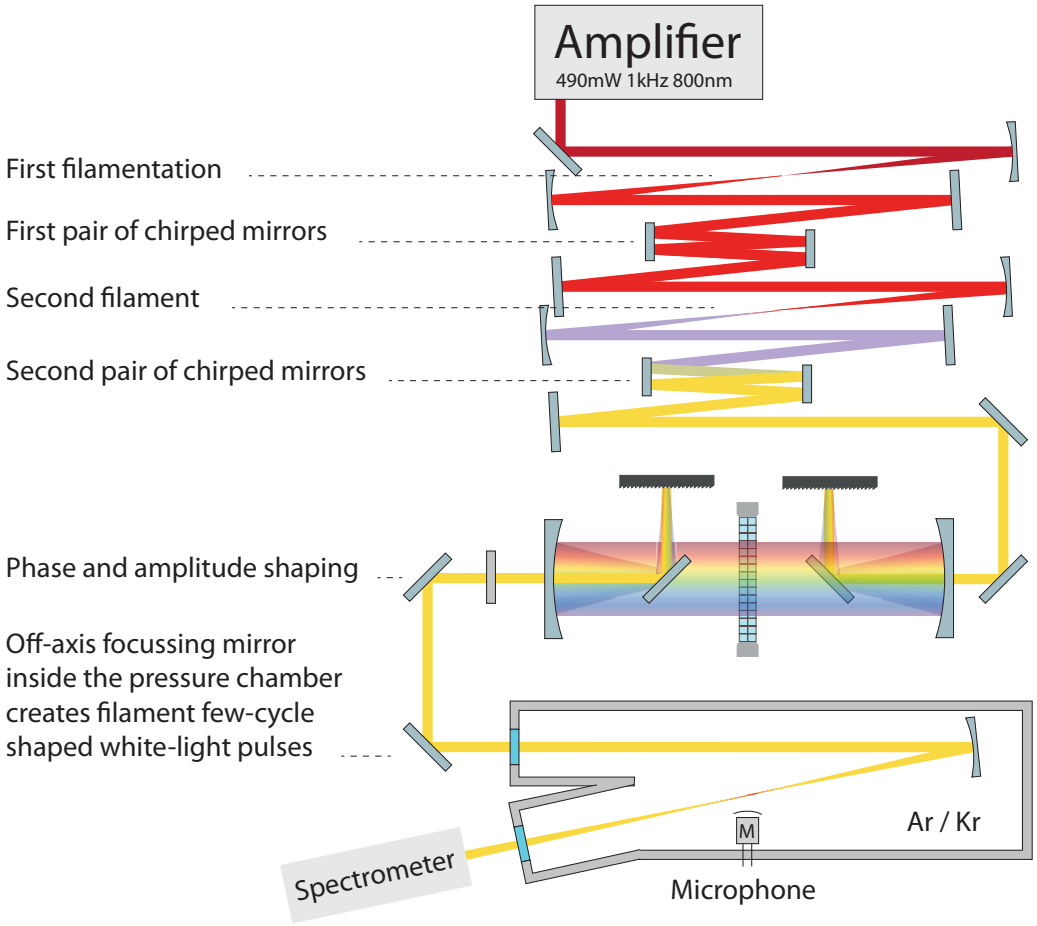

Figure 5.11: Experimental setup as used in the experiments on Krypton and Argon with shaped white-light pulses.

shaper was moved to match the central wavelength of the spectrum to a defined pixel number. This ensured that the calibration matched the wavelengths on each pixel. This is relevant, since the retardance introduced by each pixel is strongly wavelength dependent. Calibration of the white-light setup was described in [63]. In the scope of this thesis a program was developed which simplifies the calibration processes by automating all consecutive steps required for calibration. Besides the measurement of TG-FROG (5.3.2) traces of shaped pulses, amplitude shaping (especially when zero transmission was set as a test) was a strong indicator of a good calibration. After the shaper, the beam was then steered to either a spectrometer, TG-FROG or the experimental chamber. Using the pulse shaper to compensate for the remaining pulse-chirp we were able to repeatedly measure TG-FROG-lengths of $5-7\,fs$ (FWHM) at pulse energies up to $50\,\mu J$ just before the measurement chamber. Since the TG-FROG is very sensitive on the peak-intensity, we were not able to measure the pulses with more complex pulse shapes. [Fig. 5.12 a)] shows a close to transform-limited (TL) pulse as it was measured after manual compensation of the remaining chirp with the help of the pulse shaper. The capability of the pulse shaping setup is demonstrated in [Fig. 5.13] in which TG-FROG traces of a negativ and positiv linear chirped pulse are depicted. After the pulse shaping setup, the beam passes a couple of silver steering mirrors and finally an off axis focussing mirror ($f = 250\,mm$). The focussing mirror was placed inside of the pressure chamber which was filled with either Argon or Krypton. This ensured that in the entrance window of the chamber (d=1/4

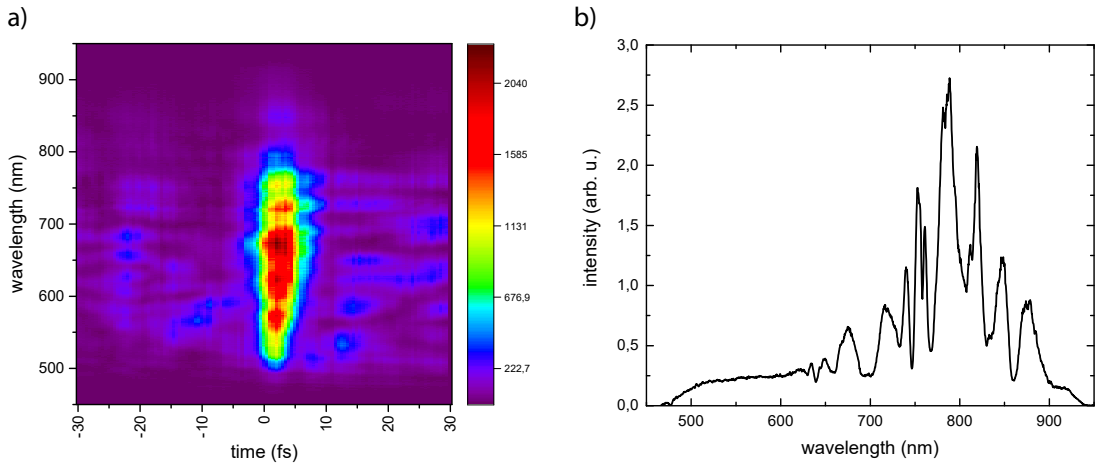

Figure 5.12: a) TG-FROG trace of a short white-light pulse as it was after manual phase correction. b) Usual white-light spectrum measured just before the pressure chamber.

inch) no nonlinear effects occurred that would interfere with the measurements. The spectrum was measured after passing through the exit window of the chamber with a spectrometer (USB2000 UV/VIS, OceanOptics) pointed at a beam block which was covered in Teflon. Teflon is used because it reduces the amount of interference from multiple reflecting surfaces. The chirp introduced by the gas cell and all further optical elements in the beam line had to be accounted for, as small variations measurably changed the pulse length on a daily basis. Thus, an electric microphone was placed just below the filament position. It recorded the acoustic shock wave produced by the formation of the plasma. This value can be safely assumed to be proportional to the free carrier density in the filament. By using PRISM [64] (chapter 4.8.2) an optimal phase compensation was found which would maximize the acoustic shock wave from the filament. The acquired shock wave was first amplified by an operational amplifier and then measured via an oscilloscope. The oscilloscope data was then evaluated by a computer to find the intensity of the acoustic shock. After one knows the phase that creates a transform limited pulse in the experiment, one can use this phase as an offset to every other phase modulation that could be applied to a pulse. This is of course only true when nonlinear effects can be neglected. This applies for the most part of the beam line after filamentation, since intensities become only significantly large when the beam is focussed.

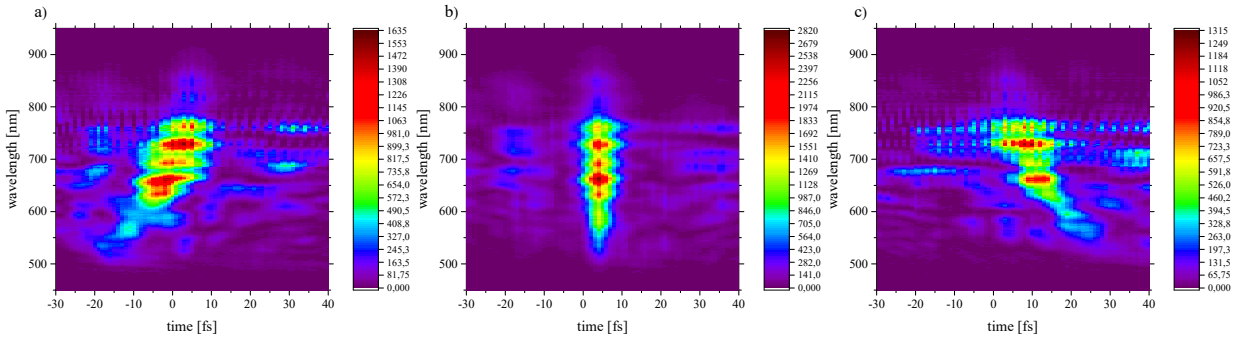

Figure 5.13: TG-FROG traces of chirped and unchirped pulses before the chamber: a) pulse negatively chirped to $-20\ fs^2$ b) transform-limited pulse c) pulse positively chirped to $20\ fs^2$. As a result of the TG-FROG's calibration higher wavelengths are underrespresented in the traces presented here.

Extended Simulation Methods and Algorithms

6

Computer controlled experimentation significantly increased the pace at which experiments are conducted. Data acquisition is now mainly executed by computer programs which allow to scan vast parameter spaces with little or no human input. This shifts the field of work of an experimental physicist towards planning, automation and analysis of said measurements. During this thesis, programs controlling parametric pulse shaping were developed, optimization algorithms enhanced and a simulation of the pulse propagation in nonlinear media was created.

6.1 Enhanced convergence for genetic optimizations by parameter-wise mutational coefficients

6.1.1 Introduction

Genetic optimization is a widely spread method for finding optimal pulses in coherent control experiments [65]. The principals of GO's were covered previously in chapter 4.8.1. The strength of these methods lies in the robustness of the optimization, even if a large number of parameters have to be optimized or the signal to noise ratio is not optimal. Downsides are that convergence cannot be measured, thus multiple optimizations have to be carried out to get a sense of whether a global optimum was found. In the early days of coherent control non-binary GO's were employed to optimize every pixel of a SLM separately [6]. Results, if achieved were difficult to interpret. This gave rise to parametric optimizations were sub-pulse parameters, like intensity and chirp, could be optimized directly [26]. During experiments conducted for this thesis, it became apparent that the choice of relative parameter scaling was a relevant factor affecting convergence of the optimization. The mutational parameter defines whether an optimization extends into the parameter space by mutation or converges due to crossover. This mutational parameter is usually applied to all parameters equally. Parameters are scaled down (using their search space boundaries) to a range of (0-1). Thus, parameters with a large influence on the fitness will have the greatest impact on how the evolutionary parameter evolves. This can lead to premature convergence for e.g.: chirp Taylor series parametrizations. Separate mutational parameters would solve this issue by independently scaling the search space in each dimension.

6.1.2 Method for Updating Parameter-Wise Mutational Coefficients

In order to change mutational parameters for each parameter separately, a measure for the fitness of a single dimension has to be defined. Therefore, an additional information was saved during the mutation-phase of the genetic algorithm. From one generation to another, mutation occurs for every parameter of a given set with a certain probability (P_μ). This in turn implies that not every parameter of one set will be changed by mutation. Let us assume we remember the information whether a parameter was mutated or not until after evaluation of the fitness. For each parameter we now count the number of cases where first, an individual improved its fitness from one generation to the next, and second, the parameter in question was indeed mutated (and therefore responsible for the change in fitness) during the last generation. This number (R_i) is normalized by the

	gen. until converged	not in time	local minimum
single mutational parameter	36.5	69	36
parameter-wise mutation rate	36.1	33	17

Table 6.1: Results of over 1000 optimizations carried out with either method were averaged. Both methods took the same average time to converge. Overall, parameter dependent mutational rates resulted in more robust optimization, thereby reducing the number of optimizations which did not finish in time or converged into local minima of the test function.

mutation probability and the number of individuals in one generation. This value (which was calculated for each parameter) was used to evaluate whether a single parameter had contributed to the improved fitness. Finally, when R_i was greater than 0.3 (in contrast to 0.2 which attributes to the 1/5th rule), the parameter-dependent mutation rate (μ_i) was increased by 1.2 and else decreased by 0.8.

6.1.3 Convergence of the Proposed Method on a Variety of Test Functions

The efficiency of the proposed method was tested in a simulation against the standard approach which uses only one mutational parameter. Ackley's function was chosen as a test-potential, since it possesses local minima as well as a global minimum at $f(x_i = 0) = 0$. Ackley's function is defined by [66]:

$$f(x_1, x_2, ..., x_n) = -20e^{-0.2\sqrt{\frac{1}{n}\sum_i x_i^2}} - e^{\frac{1}{n}\sum_i \cos(2\pi x_i)} \tag{6.1.1}$$

1000 automated optimizations were carried out for both, with and without parameter-wise mutational parameters. All other settings regarding the optimization were kept equal. In order to present the optimization with a scaled parameter space, the boundaries of 4 dimensions were chosen differently. The parameters were initialized and evaluated using the boundary conditions (± 5, ± 2, ± 1, ± 0.1). In both optimizations, P_μ was equal to 0.54, 14 individuals were used for crossover, 2 survivors kept from one generation to another. Generations themselves had 40 individuals and all mutational parameters were initialized with 0.05. Optimizations were either stopped after the error fell below the threshold of 0.004 or after 70 generations (which is a reasonable number to be evaluated in real world experiments). No extra noise was added which could be used to improve convergence into the global optimum. The success rate above which the mutational parameter is increased or decreased is different in both optimization schemes (0.2 for the single and 0.3 for the multi mutational parameter optimization). This is reasonable, since the definition of success was changed significantly for the multi-parameter approach. Both values were optimal for convergence of the corresponding method at the selected optimization settings. Tab. 6.1 summarizes the results from the optimizations carried out on the test function. Both methods converged in nearly the same number of generations. A difference became apparent when regarding the number of optimizations which did not converge in time, or converged into a local minimum. Here, the parameter-wise mutation rate led to more robust results. From the evolution of generations it was observed that a single mutational parameter led to symmetrical "ball like" convergence while for parameter-wise mutation rates elliptic spreading of the individuals during convergence occurred, which seemed to fit the unequal scaling of the four parameters.

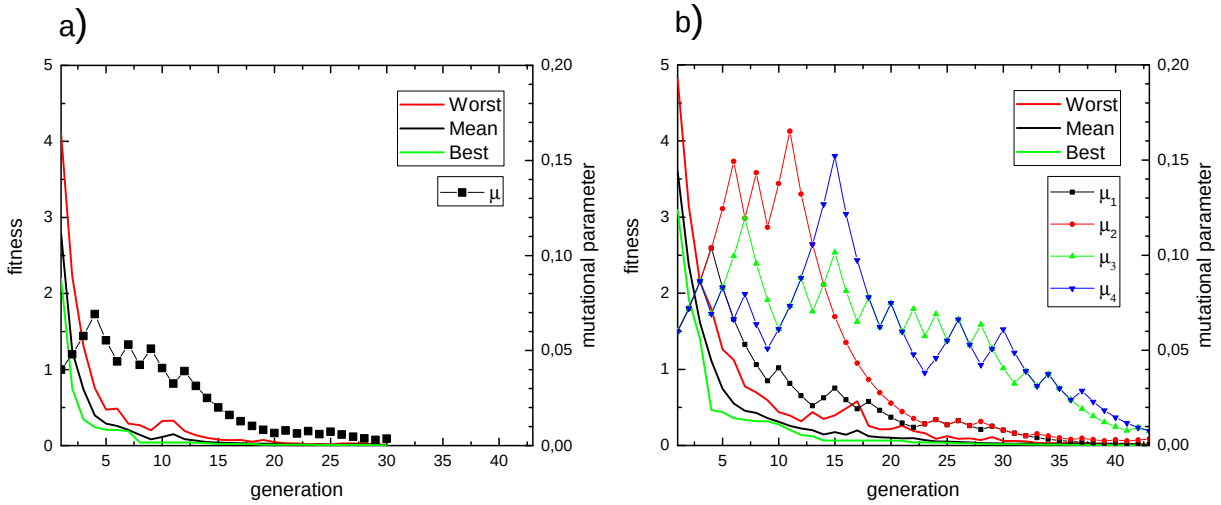

Figure 6.1: a) The optimization which relies on a single mutational parameter, converges quicker but is more prone to converge into local minima. b) Multiple mutational parameters evolve differently, which increases the search volume depending on the influence the parameter has on the fitness. Overall, in this example, it converges slightly slower as an optimization with only one mutational parameter.

6.1.4 Conclusion

A genetic optimization is especially suitable when not much information exists on the search space itself. On the other hand, parametric optimizations allow interpretation of the results obtained by the optimization and are favourable when the aim exists to learn something about the examined system. In both cases parameters can be scaled immensely different. While some will have nearly no influence on the evolution of the optimization, others will lead to more noticeable changes of the fitness and thereby be the deciding factor whether and when the optimization will converge. Using parameter-wise mutational coefficients, each dimension can converge independently. This can slightly increase the total time of convergence but reduce the risk of finding local minima. Additionally, the information on the evolution of the mutational coefficients can be used as a measure of influence of each parameter on the fitness. It can be concluded, that when scaling of the parameters is not known multi-evolutional-parameter optimizations can be considered to be beneficial.

6.2 Two-Dimensional Propagation of Octave Spanning Laser Pulses in Ionised Media

The simulation outlined in this chapter was initially based on the Split-Step Fourier method as described by Agrawal [28]. The method was first implemented to simulate nonlinear effects in a one dimensional retarded time frame, as it it is sufficient to reproduce effects observed in nonlinear fibres. This one-dimensional simulation was quickly extended to give insight on the nonlinear evolution of pulses in a focussed Gaussian beam. To accomplish this the intensity of the beam was calculated according to the formula of a Gaussian beam focus for each propagation step of the split step method. This allowed for the simulation of the spectral changes that occur in the Gaussian beam focus of the fluorescence setup as outlined in chapter 5.5. For amplified pulses, as they were used in the experiments on L-Tryptophan, self phase modulation was found to have a great influence on the excitation progress. Pulse shaping can be used to exploit this process as we will show later. As experiments on the filamentation in Argon and Krypton were conducted simulations on the propagation of ionising media became of interest. The simulation was consequentially adapted to allow propagation of the focussed beam following the work of Sprangle et.al. [37].

6.2.1 Pulse Parametrization and Initialization

As self-focussing and plasma defocussing are the most important effects governing filamentation, a spatial approach had to be found. In order to speed up the simulations a two-dimensional, cylindrical pulse parametrization was chosen. The electrical field was stored in form of an amplitude $|E(\omega, r)|$ and phase $\Phi(\omega, r)$, so that only the radial beam profile was modelled. Sampling of $r \to r_i$ (Δr) and $\omega \to \omega_j$ ($\Delta\omega$) was reduced until no more changes of the simulation output could be observed. Since the experimental conditions show an axial symmetry as well one should not expect large deviations from this parametrization when compared with a full 3D simulation. The pulses were initialized with the electrical field which was calculated from a reference spectrum ($I_{ref}(\omega)$) taken in front of the measurement chamber (Setup B). The beam, which is focussed by a focussing mirror placed in the pressure chamber, will only experience nonlinear effects around the focus. The propagation until nonlinearities arise can be easily calculated with the help of the formula's governing linear dispersion and the Gaussian beam. A region around the focus, from $-1\,cm$ to $1\,cm$ was selected and the pulse initialized to fit the conditions at the beginning of the simulation. To accomplish this, the beam diameter $w(z)$ and beam waist w_0 were calculated from the original beam width prior focussing ($1\,cm$) and the focal length of the focussing mirror ($25\,cm$). This beam waist ($\sim 0.4\,mm$) was then used to model the Gaussian radial falloff of the initial electrical field amplitude:

$$|E(r_i, \omega_j)| \propto \frac{w_0}{w(z)} e^{-\frac{r_i^2}{w(z)^2}} \sqrt{I_{ref}(\omega)} \tag{6.2.1}$$

The radial phase was initialized with the help of the Gaussian beam formula as well. Additionally, the phase amounting to the gas dispersion from the point of initialization up to the focus was compensated for. This was done assuming the pulse is transform limited at the focus position. The phase then becomes:

$$\Phi(r_i, \omega_j) = \frac{\omega_0 r_i^2}{2cR(z)}, \tag{6.2.2}$$

where

$$R(z) = z\left[1 + \left(\frac{\pi\omega_0^2}{\lambda z}\right)\right] \tag{6.2.3}$$

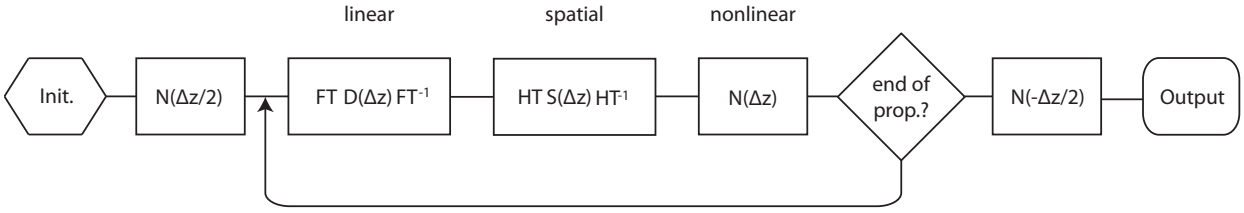

Figure 6.2: Flow-chart depicting the method for spatial, linear and nonlinear evolution of ultrashort laser pulses.

is the radius of curvature. Finally, the electrical field was normalized such that the pulse energy E_P becomes:

$$E_P = \sum_i \sum_j \left(2\pi r_i \frac{c\epsilon_0}{2} |E(r_i, \omega_j)|^2 \Delta r \Delta\omega \right) \tag{6.2.4}$$

6.2.2 Temporal and Spatial Propagation

The split-step method implemented here relies on the Fourier-transform to efficiently integrate all operators which take part in the evolution of the laser pulses. All effects are integrated in steps of the propagation distance Δz until the end of propagation is reached (see Fig. 6.2). Dispersion is easiest to evaluate in the spectral domain $E(r, \omega)$. All other nonlinear effects are propagated in the time domain $E(r, t)$. Finally, spatial propagation is achieved by adding a propagation phase in the reciprocal (k-) space. For this, a Hankel transform (radial Fourier transform) is used to transform the field into the reciprocal space $E(k, t)$. While dispersion (D , in Fig. 6.2) and spatial propagation (S) amount to a simple phase which is added in each propagation step, the nonlinear step on the other hand is more complex. Here, SPM, self-steepening, plasma defocussing and losses that occur through ionisation are included. This calculation takes up the biggest share of simulation time. An important factor of the simulation's sampling is the scaling imposed by the Fourier and Hankel transforms. As the scaling process is equivalent for spatial and temporal Fourier transforms, only one case will be discussed. Let us assume one chooses a sampling of the electrical field $E(\omega)$ in the frequency domain which starts at ω_{min}, ends at ω_{max} and uses N samples. The Fourier transform will then feature N samples extending from t_{min} up to t_{max}. One then obtains:

$$t_{max} = -t_{min} = \frac{\pi N}{(\omega_{max} - \omega_{min})} = \pi f_s. \tag{6.2.5}$$

and hence finds the spacing between temporal samples:

$$\Delta t = \frac{2\pi}{N\Delta\omega} \tag{6.2.6}$$

Here, f_s is called the sampling frequency (not to be confused with spectral frequencies). The resolution obtained from the Fourier transform in this way may sometimes be insufficient to accurately model nonlinear or extremely fast ionisation processes. As one can see from the last equation, the temporal resolution can be improved by increasing the number of samples. This was accomplished by padding zero's symmetrical in frequency space, typically increasing the temporal resolution by a factor of 3. While zero padding has a solely cosmetic effect on Fourier-transforms of continuous signals, it is a sensible and accurate method when applied to pulses with a finite pulse length.

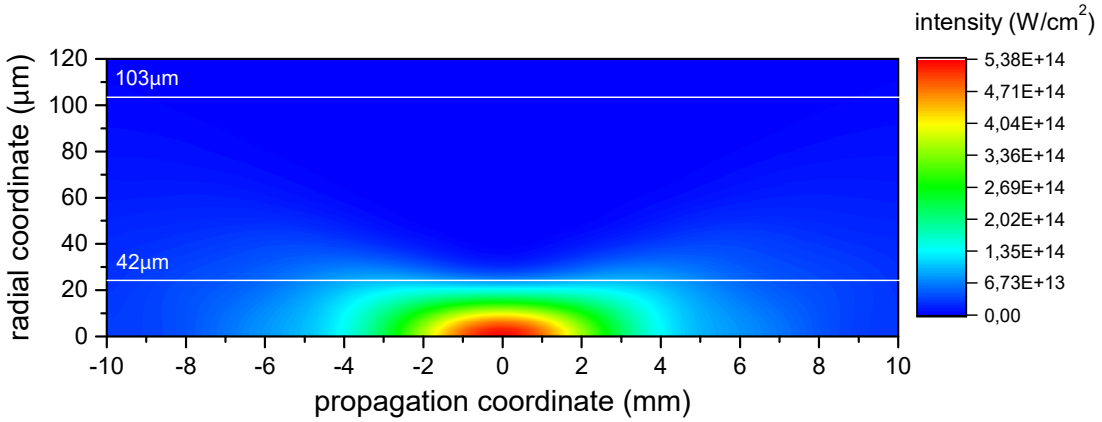

Figure 6.3: Test of the linear propagation of a focussed laser beam using the implementation of the split-step method. The calculation window ranges from $-1\,cm$ before to $+1\,cm$ after the focus. The expected beam width (measured at $1/e^2$ of the peak intensity) at the beginning of the simulation and at the focus is marked by a white line. This image is a two-dimensional representation of the simulation result. For each vertical line spectral as well as phase information is evaluated during propagation.

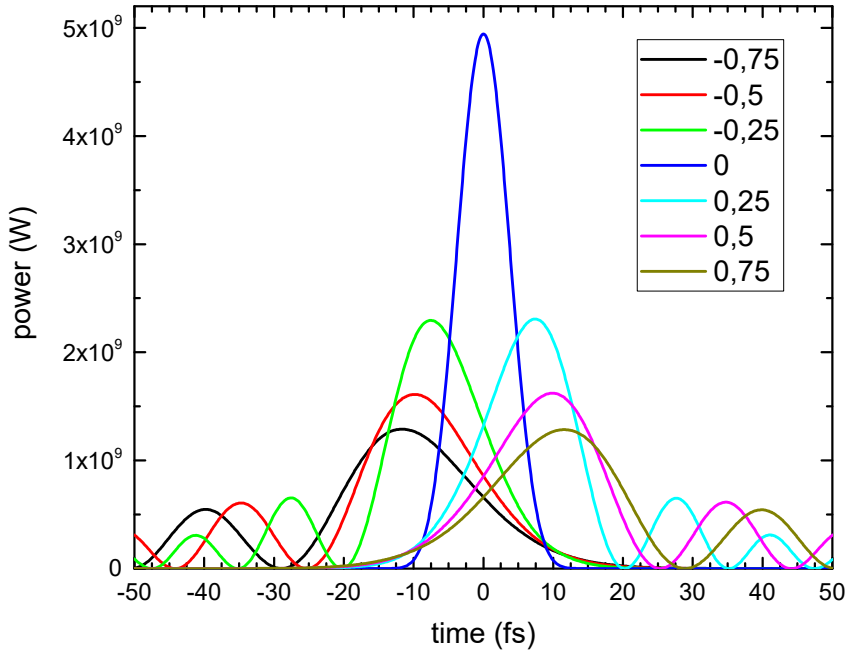

Figure 6.4: Propagation including dispersive effects. The simulated material features a GVD of $1000 fs^2/m$ and a TOD of $5 \times 10^4 fs^3/m$. The pulse was initialized by half the dispersion which would occur over the total propagation length. The simulation shows that the pulse becomes (as it is supposed to) TL at the centre of the simulation window.

6.2.3 Linear Propagation

In order to check whether the implementation is correct, a simulation of only the linear effects (spatial propagation, dispersion) was conducted. A beam with a diameter of $0.5\,cm$ is focussed by a focal length of $25\,cm$. The beam width at the beginning of the simulation was calculated using the Gaussian beam formula. At the beginning of the simulation ($-1\,cm$), the radial intensity was initialized to correspond to a Gaussian beam with a radius of $103\,\mu m$. The two-dimensional plot (Fig. 6.3) shows the focussed beam as an intensity profile in dependence of r and z. From this figure we can see that the beam waist, which was supposed to be $24\,\mu m$ was correctly reproduced. When nonlinear and plasma effects are neglected, dispersion and spatial beam propagation do not interfere. This was also the case in the simulation.

After a material dispersion of $10^3 fs^2/m(GVD)$ and $5\times10^4 fs^3/m$ was introduced, no changes to the spatial propagation were observed. The spectrum was initialized with a Gaussian spectrum centred at $750\,nm$ and with a width of $100\,nm$. Before the simulation was conducted, a spectral phase attributing to half of the dispersion which occurs over the complete propagation window, was subtracted. Fig. 6.4 shows the evolution of the temporal pulse shape corresponding to the data in Fig. 6.3. In this graph the temporal pulse power is plotted. The power was calculated from integrating the intensity over the beam profile. We can see that both spatial focussing and dispersion compensation lead to an extreme power build up towards the focus ($z = 0\,cm$). As expected the pulse shapes resemble symmetrically quadratically shaped pulses for positive and negative distances from the focus. These simulations, in addition to other tests of the capabilities of the implementation, show that dispersion and spatial evolution can be accurately modelled.

6.2.4 Nonlinear Propagation

All nonlinear effects that could influence the propagation of ultrashort pulses (see chapter. 4.6) were analysed and tested on their relevancy for the propagation of pulses under the experimental conditions at hand. In this chapter, tests to ensure all effects are correctly implemented will be presented.

Self-Phase Modulation

SPM is the dominant nonlinear effect in most of the conducted experiments. It manifests itself by a phase which is added in the temporal domain:

$$\Phi_{SPM}(r_i, t_k) = \frac{n_2\epsilon_0}{2}|E(r_i, t_k)|^2\omega_0\Delta z \tag{6.2.7}$$

This factor is proportional to the nonlinear refractive index, and the intensity. Self-phase modulation leads to self-focussing and spectral changes like spectral broadening. Fig. 6.5 a) illustrates the effect of strong self-phase modulation on a focussed laser pulse. This simulation used spatial propagation in addition to self phase modulation in a non dispersive medium. The nonlinear refractive index was selected to be $2\times10^{-23}m^2/W$. The spectrum on the other hand was initialized as a Gaussian spectrum with a central wavelength of $750\,nm$ and a spectral width of $100\,nm$. This allows for easy inspection of spectral changes. Fig. 6.5 b) depicts the spectrum at the end of the simulation. Spectral broadening due to self-phase modulation is greatest in the centre of the beam, while broadening is reduced for larger radial coordinates.

Since the beam width, focal length and central frequency of the spectrum for both (linear and nonlinear simulation) were equal, Fig. 6.5 (c) should compare well to Fig. 6.3. Self-focussing due to SPM increases to a 4-fold intensity build up in the focus. Additionally, the focus appears

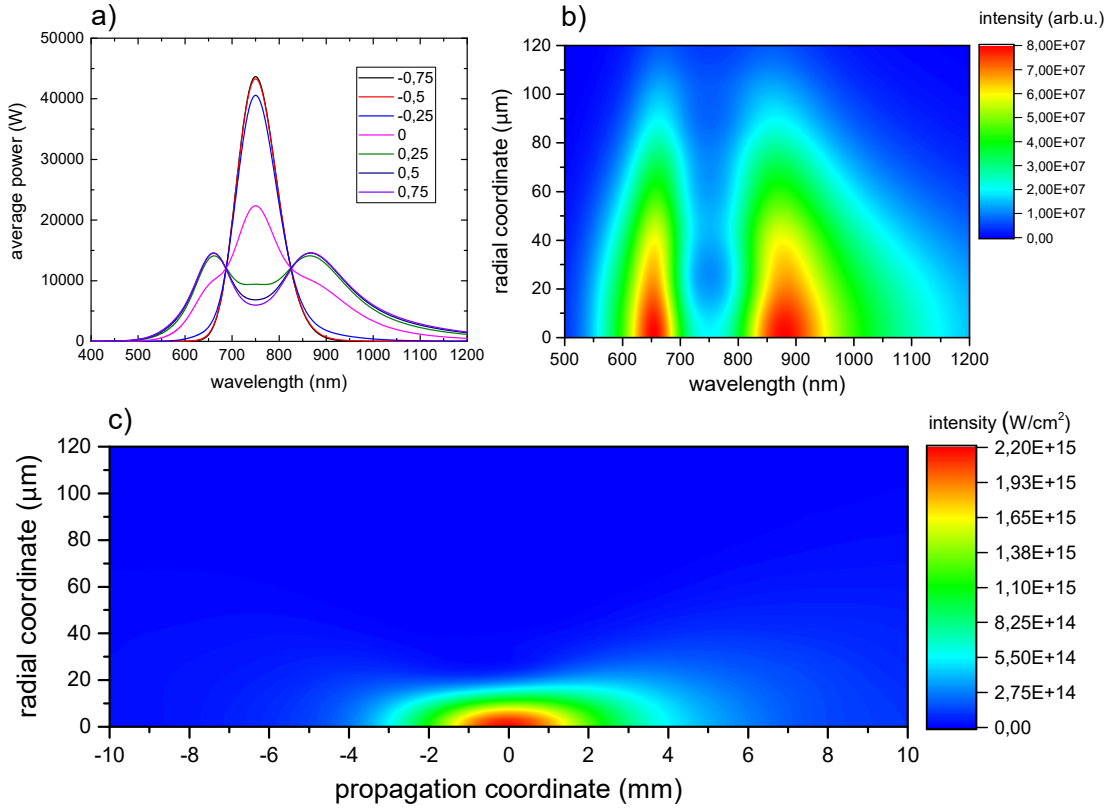

Figure 6.5: Propagation test, which includes SPM. a) Due to focussing the pulse intensity rises towards the focus. After the focus SPM distorts the pulse spectrum. Typical SPM induced spectral broadening can be observed. Note that spectra displayed here are integrated over the complete beam area. Since SPM is intensity dependent, spectral changes will differ depending on the distance to the centre of the beam. b) Intensity profile in dependence of the radius and wavelength after the full propagation distance (z=1). c) While the simulation result should be comparable to the linear case discussed before, distinct differences can be observed. SPM results in self-focussing and therewith higher peak intensities.

to be slightly asymmetric. This might be a result from decreased self-focussing due to the strong modulations which occur at the focus.

Self-Steepening

Self-steepening can be understood as a correction term to self-phase modulation which also arises from the nonlinear polarizability of the optical medium. Self-Steepening leads to a change of the temporal pulse profile, which can be best described as a steepening of the trailing flank of a pulse. Again, simulations were performed, in which Dispersion was neglected and the nonlinear refractive index reduced to a realistic value ($n_2 = 10^{-19} cm^2/W$) compared to the experimental conditions we will study later. Self-steepening manifests itself by a temporal phase and amplitude factor which incorporate a derivative of the temporal electrical field:

$$A_S = -\frac{n_2 \epsilon_0}{2} \left[\frac{\partial E(r_i, t_k)}{\partial t}^* E(r_i, t_k) + 2 \frac{\partial E(r_i, t_k)}{\partial t} E(r_i, t_k)^* \right] \Delta z. \tag{6.2.8}$$

Here, the partial integration is used for reasons of clarity. For evaluation, this term was replaced by an adequate discrete differentiation method. When self-steepening is taken into account it is

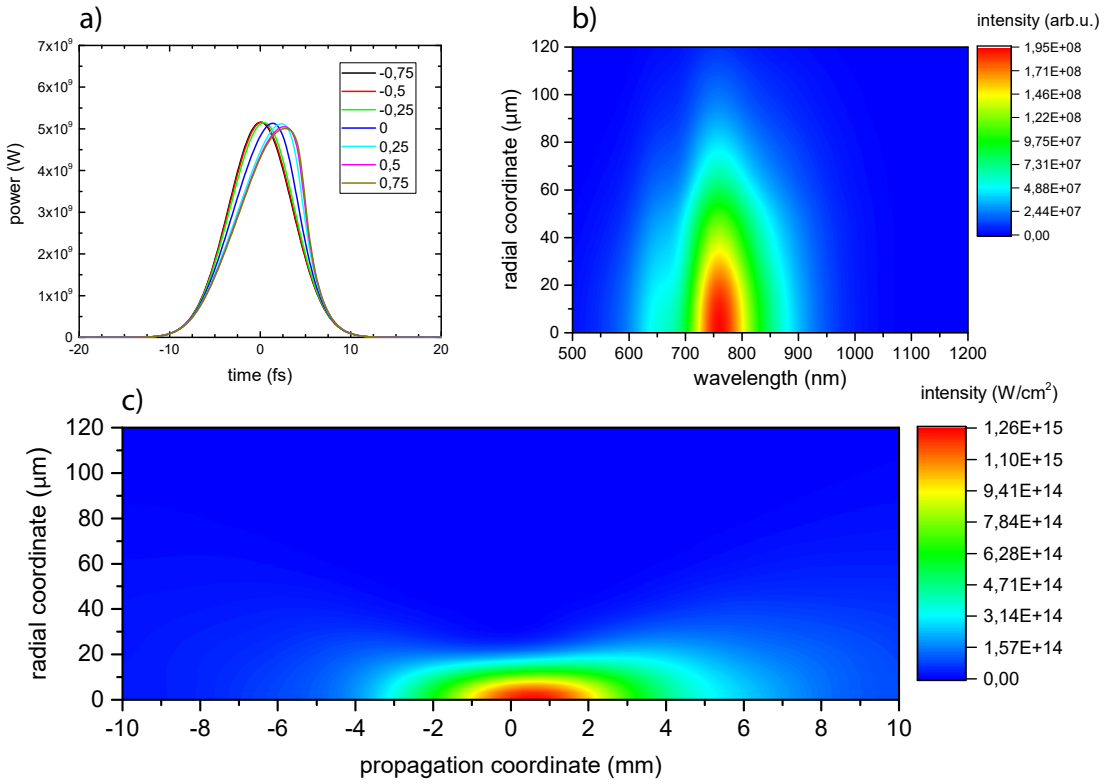

Figure 6.6: Propagation test which includes Self-steepening in addition to SPM and spatial evolution. a) Shows how the temporal pulse profile changes. Self-steepening leads to a steepening of the trailing edge of the pulse (Compare: fig. 4.9). b) Spectral modulations are less pronounced than in the SPM only simulation because of the smaller value for n_2 selected for this simulation. c) Spatial propagation is very similar to previous calculations.

critical to choose a fine sampling because small modulations can otherwise lead to a build up of errors during propagation. Fig. 6.6 summarizes the results found by this simulation. While no big differences can be found in the spatial propagation of the beam (Fig. 6.6 c)), the pulse evolution (Fig. 6.6 a)) depicts the previously discussed effect of a steepening of the trailing edge of the pulse. Spectral modulations, though smaller, are again strongest at the centre of the beam. Overall modulations are less pronounced which is the result of the decreased nonlinear refractive index.

Plasma-Effects

Plasma interaction is modelled by two separate effects. First, pulses loose energy while propagating due to the energy required for ionisation. Second, the free electrons have an effect on the polarizability of the medium, which manifests itself as a defocussing effect on the beam. Preliminary calculations showed that multiphoton ionisation is the dominant ionisation process in the conducted experiments. The rate at which multiphoton excitation occurs was calculated via (see eq. 4.6.56):

$$W_{mp} = \frac{c\pi\epsilon_0\omega_0|E(r_i,t_k)|^{2n}}{(n-1)!\,(w_0^2\hbar/\sigma_{mp})^n}, \tag{6.2.9}$$

where σ_{mp} is the multiphoton cross section. Here, we assume that recombination effects are far longer than the pulse duration. Additionally, the low repetition rate ensures that each pulse experiences a "fresh" volume of gas at each propagation step. This means, that simple integration

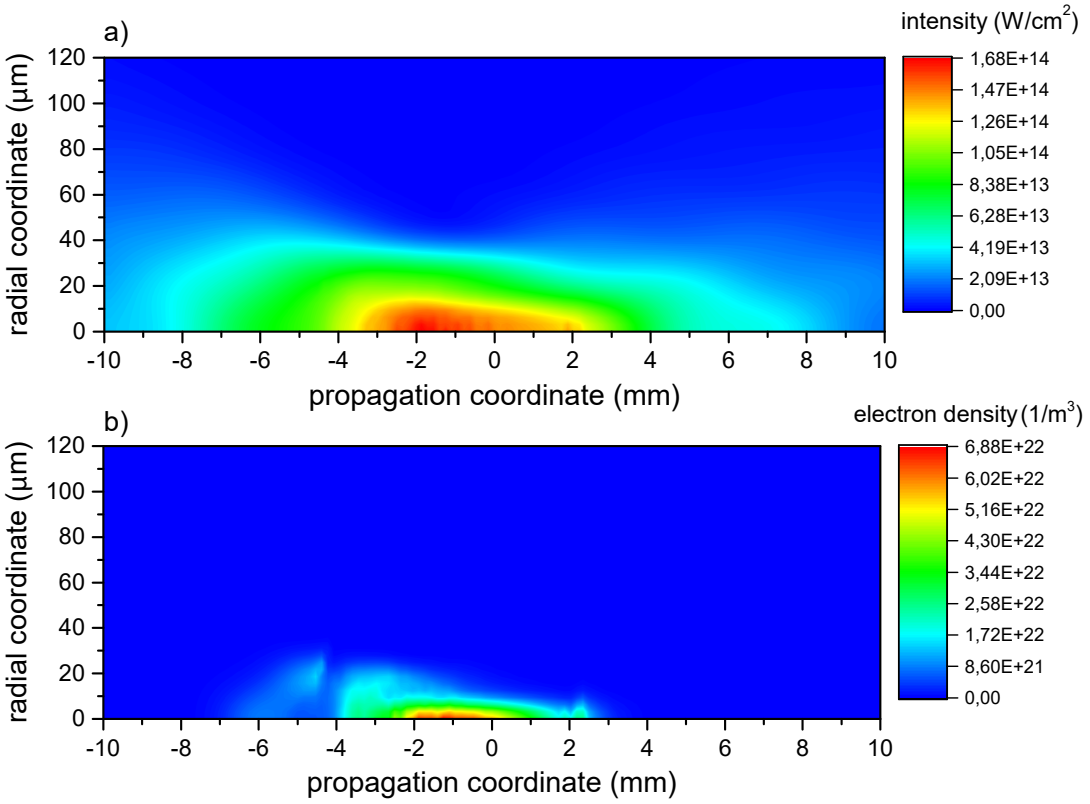

Figure 6.7: a) Radial intensity profile of a simulation incorporating SPM, self-steepening and plasma interactions. Plasma defocussing clearly increases the beam waist and creates an elongated focus. Maximal intensities are much lower than those found in previous simulations. b) Final electron (or ion) count $n_e(r,z)$ generated by a complete pulse. From these two plots the profound effect of the plasma on the beam propagation is displayed.

of W_{mp} can be used to find the ionisation count $n_e(r,t)$. From this the amplitude factor which amounts to the energy loss by ionisation was calculated by:

$$A_{ion}(r_i,t_k) = exp\left(-\frac{\partial n_e(r_i,t_k)}{\partial t}\frac{4\pi E_{ion}}{c\epsilon_0|E(r_i,t_k)|^2}\Delta z\right), \tag{6.2.10}$$

where E_{ion} is the ionisation energy. The phase factor on the other hand evaluated as:

$$\Phi_{ion}(r_i,t_k) = -2\pi\frac{n_e(r_i,t_k)^2e^2}{m_e c\omega\epsilon_0}\Delta z. \tag{6.2.11}$$

Both effects were taken into account when the simulation depicted in Fig. 6.7 was run. Fig. 6.7 a) shows a beam with a significantly larger beam waist than in previous examples. Plasma defocussing leads to an elongated focal region with a hot spot when the beam primarily focussed. Maximal intensities are also lower than in previous examples. Fig. 6.7 b) displays the electron count $n_e(r,z)$ which is the integrated number of electrons created by an entire pulse. It is interesting to see how the shape of the plasma clearly defines the shape of the focus. The full method as described in this chapter was not completed until the experiments on filamentation in Argon and Krypton. Thus, only a reduced but sufficient simulation model was applied to understand the measurements on Tryptophan, Rhodamine B and Coumarin 1.

Experimental results 7

7.1 Optimization of Two-Photon Processes after Photonic Crystal Fibres

Parts of this chapter were published within the scope of my doctoral thesis in the Journal Applied Physics [67]. The last section of this chapter covers experiments which utilize a novel Kagomé fibre for pulse delivery. The work on the Kagomé fibre was conducted in cooperation with Julius Otto, who wrote his Master thesis in our experimental group. These experiments were also published recently [68].

7.1.1 Preliminary Work and Introduction

The methods of coherent control allow us to gain a greater understanding of the structural and electronic properties of atoms, clusters and even biologically relevant samples. A promising field in coherent control lies in the excitation of multiphoton processes with shaped ultrashort pulses. In this chapter two-photon excitation with parametrically-shaped pulses created by a femtosecond oscillator will be explored. Control of three-photon processes by shaped amplified pulses will in turn be covered by the next chapter.
Two-photon excitation is a nonlinear process which was first studied by Maria Göppert-Mayer in 1930 [36]. It was shown that laser scanning microscopy can achieve higher resolution when multiphoton- rather than single photon excitation is applied [69]. Mostly, infrared light is utilized in two-photon excitation schemes which allows for greater sample penetration than one-photon excitation in the visible spectrum [70]. As the efficiency at which two-photon excitation takes place scales with the Intensity squared, the focus of the beam can be used to determine at which depth fluorescence will be originating. Therefore, this method can even be used to generate three-dimensional images [71]. By using Taylor-shaped laser pulses and by taking advantage of intra-pulse interference, narrow absorption bands can be selectively excited with the same efficiency as a transform-limited pulse [8]. With this method, selective excitation of close lying two-photon absorption bands becomes feasible [35]. At the same time, sample damage which originates from high order nonlinear effects is reduced. These advantages gave rise to a series of publications demonstrating first control of selective excitation by simple phase shaped pulses [72, 73, 74, 75]. Even if suitable phase functions or pulse shapes are identified, the pulses have to reach the sample in a controlled manner. Dispersion, as well as nonlinear effects can strongly disturb the pulse spectrum as well as its phase. Photonic crystal fibres allow the transmission of pulses with high peak intensities and mostly exhibit low dispersion. Fibres can be seen as a manageable method for pulse delivery if nonlinear and or linear effects are compensated for. Compensation of nonlinear effects and polarization changes which occur when a fibre is bent and twisted was demonstrated in two earlier publications, preceeding this thesis [76, 77].
Biologically relevant samples often feature broad absorption bands which overlap and hinder selective excitation. This chapter wants to explore different spectral phase functions on their ability to selectively excite fluorescent dyes with overlapping absorption bands after a hollow-core fibre. An evolutionary algorithm will be applied to find optimal phase functions maximizing the contrast of two fluorophores in either direction. This data is used in conjunction with simulations to

understand the abilities of these parametrizations to optimize contrasts of two two-photon excited fluorophores and give an overview of the limits and future possibilities of this approach. Finally a short section will cover experiments conducted on the Kagomé fibre where two polarization shaped pulses, each optimized for either fluorophore will be used to selectively excite two dyes depending on the polarization angle of observation.

7.1.2 Simulations of the Two-Photon Field

The two-photon excitation of phase-shaped laser pulses is governed by the two-photon effective field which describes how efficient a pulse is in exciting a transition at a given wavelength. The two-photon field arises from the interference of spectral components within the laser pulse itself. In the spectral domain, the electrical field can be conveniently split into an amplitude and a phase factor: $|E(\omega)|e^{i\Phi(\omega)}$. The two-photon field, which was introduced in chapter 4.5.1, then has the form:

$$E^{(2)}(2\omega) = \int_{-\infty}^{\infty} |E(\omega-\Omega)||E(\omega+\Omega)|e^{i(\Phi(\omega-\Omega)+\Phi(\omega+\Omega))}d\Omega. \tag{7.1.1}$$

As said before, the two-photon field can be understood as the efficiency at which an infinitely narrow two-photon transition would be excited. When a spectral phase function $\Phi(\omega)$ is antisymmetric around a chosen central frequency ω_c, the phase term in (7.1.1) vanishes and $E^{(2)}(2\omega_c)$ is at this frequency equal for the phase shaped and the transform-limited pulse. A phase which is antisymmetric fulfils following requirement:

$$\Phi(-\omega-\omega_c) = -\Phi(\omega-\omega_c) \tag{7.1.2}$$

Hence, an infinitely narrow two-photon transition at ω_c can be excited equally efficient by a pulse with an antisymmetric phase function and a transform-limited pulse [8]. Excitation of broad two-photon transitions on the other hand, will always be less efficiently excited by a phase shaped than by a short pulse. Antisymmetric functions examined in this thesis will be a step-function, a sinus phase as well as a third-order polynomial phase. For broad two-photon absorptions as seen for Rhodamine B and Coumarin 1 the fluorescence intensity $I_{R/C}$ is not directly proportional to the two-photon field: If each excitation leads to fluorescence the spectral intensity in our experiment can be found by convoluting the two-photon absorbance $(\mathrm{TPA}_{R/C})$ of a dye with the two-photon field:

$$I_{R/C} \sim \int_{-\infty}^{\infty} \left|E^{(2)}(\omega)\right|^2 \cdot \mathrm{TPA}_{R/C}(\omega)d\omega \tag{7.1.3}$$

where the index R or C stands for the examined dyes Rhodamine B and Coumarin 1, respectively.

It is desirable to know the TPA of Rhodamine B and Coumarin. Since only limited data is available, measurements of the two-photon absorption were carried out. Usually, tunable pulsed laser sources, like an Optical parametric oscillator (OPO) or Optical parametric amplifier (OPA) are used to scan the excitation wavelength. The technique applied here is somewhat different. The fibre was taken out of the setup to reach the maximal resolution in this initial experiment. An evolutionary algorithm was used to compensate for any arising dispersion up to the focus in the cuvette. Therefore, a two-photon diode was placed in the position of the cuvette and its signal was used as feedback for the evolutionary optimization algorithm. This diode (G1116, Hamamatsu) with an absorption around $400\,\mathrm{nm}$ is insensitive for single photon (IR) excitation. By means of amplitude shaping a Gaussian spectrum with a width of $2.5\,nm$ was cut out of the available input spectrum. Its central wavelength was then scanned and fluorescence spectra of Rhodamine B and Coumarin 1 were taken for each step. As a reference, the same scan was repeated while measuring

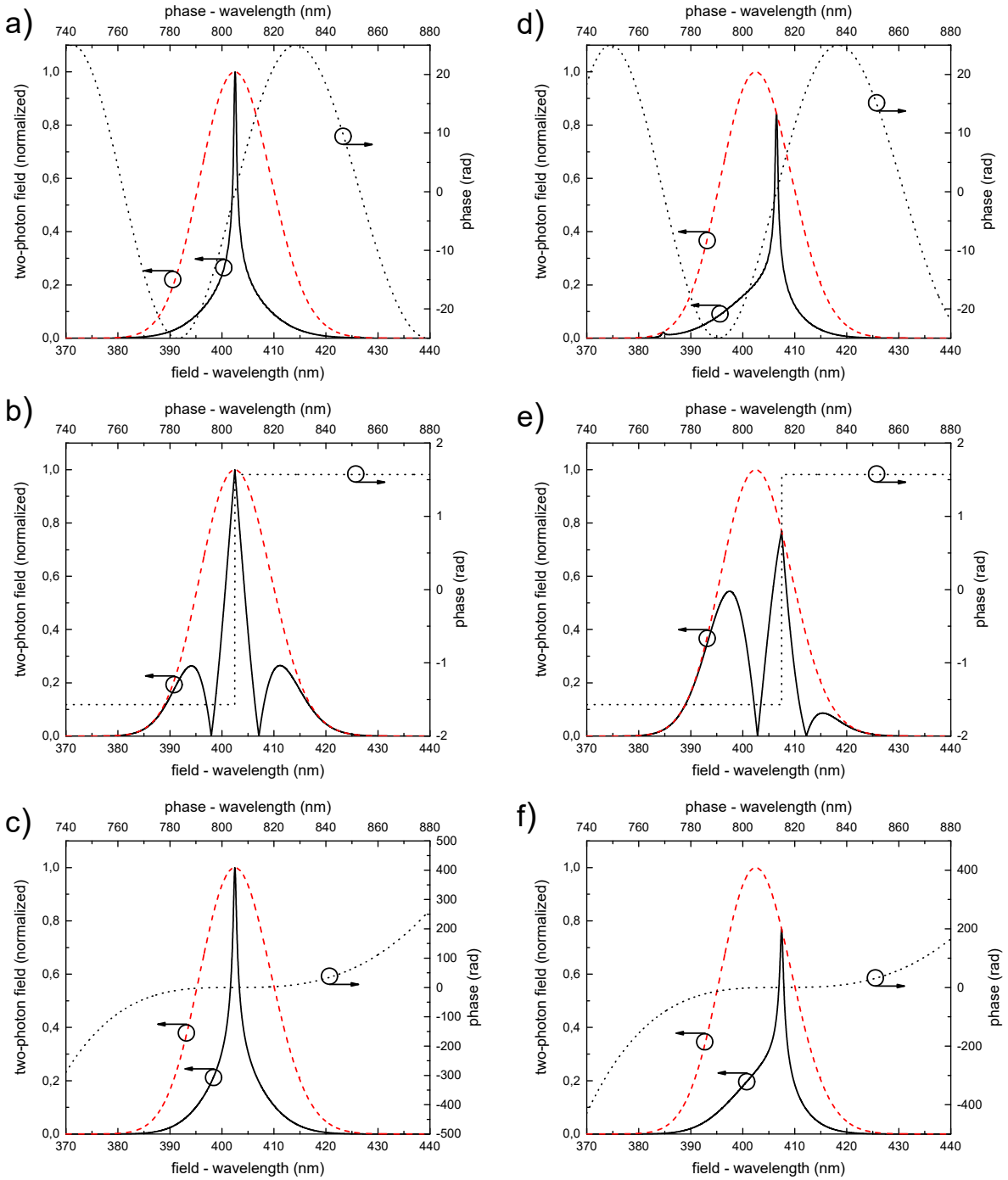

Figure 7.1: The two-photon field numerically evaluated for three types of antisymmetric phase functions. Dashed lines indicate the two-photon spectrum of a transform-limited pulse. The dotted line on the other hand is the spectral phase used in that calculation. The first three functions are antisymmetric around $805\,nm$*. For the second three graphs (d,e,f) the point of antisymmetry is shifted to* $815\,nm$*. The third-order phase (c,f) and the (a,d) sine function both result in a spike which can be used to selectively excite a certain spectral band. The* π*-step (b,e) features the same spike but also allows constructive interference for wavelengths further away from the point of antisymmetry. [67]*

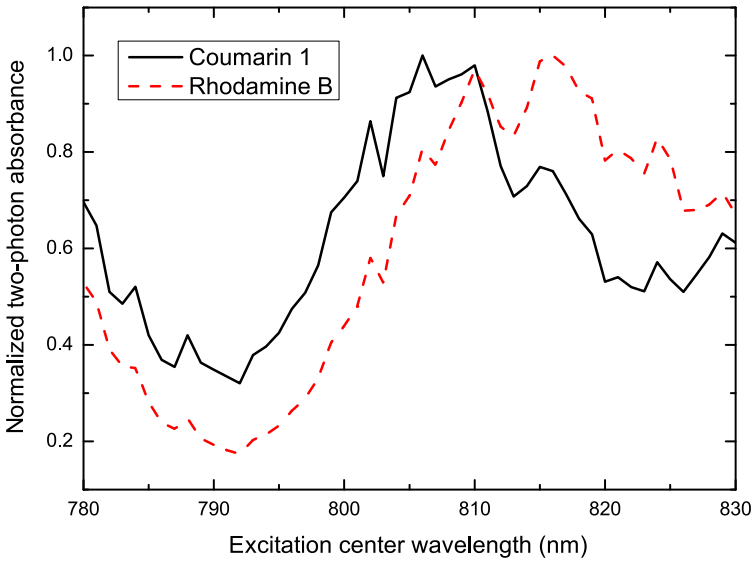

Figure 7.2: Two-photon absorbance of Rhodamine B and Coumarin 1. With the help of amplitude shaping, transform-limited pulses with a shifting Gaussian spectrum were created. For each shift of the central wavelength the fluorescence signal was integrated and divided by the signal of a two-photon absorbing diode. [67]

the signal of a two-photon absorbing diode as a reference. The integrated fluorescence signal divided by the two-photon diode signal is displayed in Fig. 7.2. Of course, this technique is only applicable in the range of the available laser spectrum. Hence, greater uncertainties of the TPA arise towards the edges of the spectrum. Also, only relative two-photon absorption can be measured. Lastly, we require a measure to evaluate the effect of different pulse shapes on selective excitation. Often, in biological imaging a contrast is defined as:

$$C = \frac{I_R - I_C}{I_R + I_C}. \tag{7.1.4}$$

Here, I_R and I_C are the integrated fluorescence signals. The contrast can feature values ranging from -1 to 1, which would imply that only either one signal is present. A contrast of 0 on the other hand stands for equal fluorescence from both samples. Obviously in real world applications the fluorescence intensity will primarily depend on the concentration of a dye in a given solution. The fluorescence ratio was not equal in the experiment, thus a transform-limited pulse was used to establish a reference intensity ratio. This was used to normalize the simulations to reflect the experimental conditions where a transform-limited pulse led to a contrast of 0.18.

7.1.3 Selective Excitation of Fluorophores after a Hollow-Core Fibre

For the actual experiments, pulses were transmitted through the Hollow-Core fibre. The fibre unfortunately possesses two glass windows on both ends which prevent dust from entering the fibre core. The beam power was reduced to $10\,\mathrm{mW}$ (which corresponds to a pulse energy of $35\,\mathrm{nJ}$) to ensure that the window did not get damaged. Nonlinear spectral changes in contrast would be no issue, since these could be compensated for by nonlinear backpropagation [13, 76]. As stated earlier, evolutionary parametric chirp optimizations were carried on the signal of a two-photon sensitive diode at the position where later the cuvette would be placed. The offset will be added to all antisymmetric phase functions discussed in this chapter to ensure that the phase is flat prior

Table 7.1: Phase functions used in the contrast scans of Coumarin 1 and Rhodamine B. λ_c or ω_c depicts their respective point of antisymmetry. The scans used parameters which are stated in the third column.

phase function	parametrization	parameters
sine	$A\sin(k(\lambda-\lambda_c))$	$A = 25\,\text{rad}$, $k = 0.0736\,\text{nm}^{-1}$
third-order	$\frac{b_3}{6}(\omega-\omega_c)^3$	b_3= $2\times10^5\,\text{fs}^3$
π-step	$\pi\Theta(\omega-\omega_c)$	

addition of a certain phase function at the point of maximal excitation. The cuvette was filled with a mixture of Rhodamine B and Coumarin 1 (chapter 5.4.2 and 5.4.1) at concentrations of: 10^{-3} molar and 7.5×10^{-3} molar.

The emission spectra of Rhodamine B and Coumarin 1 are well separated and thus can be easily distinguished (see Fig. 7.4). For contrast calculation, Rhodamine fluorescence was integrated from $560\,\text{nm}$ to $700\,\text{nm}$ and Coumarin fluorescence from $410\,\text{nm}$ to $550\,\text{nm}$. The gap in between was left un-integrated to reduce crosstalk between both signals. Contrasts calculated from the integrated spectra was then used as fitness for the evolutionary algorithm. These algorithms rely on evaluating a large amount of individuals (parameter set). This means that the time per sample is critical when trying to minimize optimization durations. This time was limited by two factors: First, liquid crystals in the modulator require some time to orient themself after an updated voltage is applied. Second, the spectrometer's integration time has to be accounted for. Many optimizations were performed until it became clear that the delay between to fitness measurements had to be twice the integration time of the spectrometer in addition to the modulator delay to ensure clean data acquisition. The evolutionary optimization was set to either maximize or minimize the contrast ratio. Besides optimizations, parameter scans of previously mentioned antisymmetric phase functions were carried out. Parameter scans are significantly faster than optimizations and are a therefore a valuable tool to map the contrasts and fluorescence intensities that can in principle be achieved. Fig. 7.2 shows that we expect Coumarin 1 to be more sensitive on wavelengths below the central wavelength of the laser spectrum. Whereas Rhodamine B has an absorption maximum which lies above the lasers central wavelength.

This leads to the conclusion that a function which results in constructive interference for lower wavelengths and destructive interference at higher wavelengths will optimize the contrast for Coumarin fluorescence and vice versa. Tab. 7.1 lists the definition of the phase parametrizations used in the parameter scans. All functions either possess a central wavelength λ_0 or central frequency ω_c which define their point of antisymmetry. At this point, the phase's antisymmetry 7.1.2 will always ensure complete constructive interference. The effect of the sine phase and third-order is clear: Constructive interference around the point of antisymmetry will be used to shift the two-photon spectrum towards the absorption maximum of either one fluorescent dye. The pi-step phase function, a variation of the Heavyside function $\Theta(x)$, shows destructive interference next to the point of antisymmetry. Further away from the step, the flatness of the phase leads to constructive interference thus resulting in an opposite effect to what the other two parametrizations accomplish. For each shift of the point of antisymmetry a spectrum is taken and the contrast evaluated. The resolution of this scan was equal to the resolution of the shaper where one pixel amounts to $0.2716\,nm$.

Fig. 7.3 shows a selection of scans that were carried out. All simulations match the measurement extremely well despite the fact that the TPA could not be easily measured at the edges of the laser spectrum. As the concentration of both dyes was not resulting in the exact same fluorescence

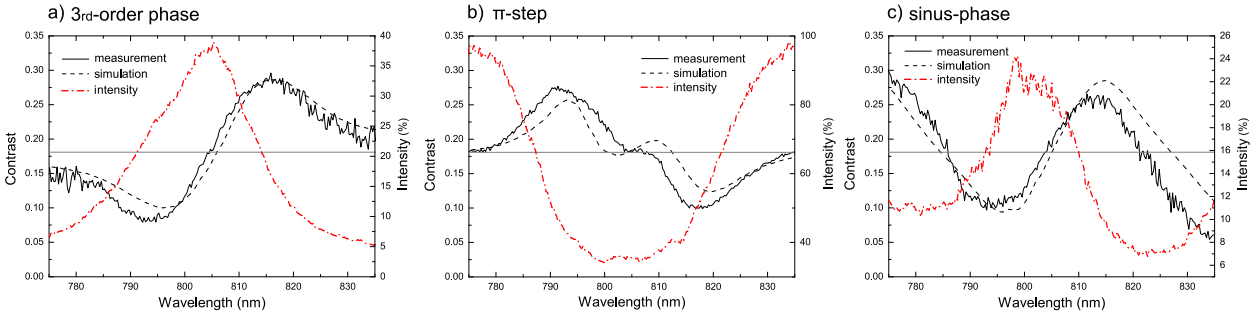

Figure 7.3: The point of antisymmetry is scanned from 775 nm *to* 835 nm *The sum of both intensities is plotted in red, and the black dashed line depicts simulations of the phase scans carried out on the basis of the previously measured TPA. a) The third-order phase shows a strong modulation of the contrast. The pi-step phase on the other hand is not as efficient in creating a contrast. A dip in the overall intensity can be seen as the step shifts through the laser spectrum. The sine-phase presents a contrast change comparable to that of the third-order phase. [67]*

for excitation by a transform-limited pulse, the contrast is shifted to larger values. The contrast of a TL pulse is marked as a solid black line as reference $C_{TL} = 0.18$. Deviations from this reference mean that a pulse either enhances Rhodamine B ($C > 0.18$) or Coumarin 1 fluorescence ($C < 0.18$). Both, the sine and third-order phase show large contrast differences which can used for selective excitation. The pi-step function on the other hand has a significantly lower influence on the contrast, which this is made up for by a large overall fluorescence intensity. At the point of maximal contrast the total fluorescence intensity is reduced to only 45% and 52% of the intensity of the transform-limited pulse.

Fig 7.4 depicts three spectra taken in the course of the parameter scans shown in Fig. 7.3. These spectra correspond to the phase shifts which generated maximal contrasts for the sine-phase parametrization. All scans were normalized to allow for easy comparison. Experimental conditions, concentration or the sensitivity of the detector will differ from setup to setup. Hence, it depends on the application whether larger fluorescence intensity or greater contrast is required.

7.1.4 Optimizations of Parametric Phase Functions for Selective Excitation

Parameters of three phase functions were optimized for maximal and minimal contrast between the fluorescence of Rhodamine B and Coumarin 1. As before, a precompensating offset-phase was added to all phase functions to account for all dispersion of the setup and fibre up to the sample. The contrast was directly used as fitness function for the optimizations. Since noise will become a significant factor for longer pulses which generate only low fluorescence it is necessary to normalize fluorescence intensities to that of a transform-limited pulse. This ensures that initialization occurs around 0 contrast. Positive and negative contrasts then stand for pulses optimized for either dye. However, all graphs depicted in this chapter will show the un-normalized contrasts. We concluded earlier, that the pi-step phase function is not able to generate large contrasts due to the nature of its two-photon field (see. Fig. 7.1). Hence, it was not used as a parametrization in the evolutionary optimizations. A third-order phase, a Taylor polynomial of 5th order and a sine phase with variable amplitude and frequency were selected as parametrizations for the optimizations. The results of the best optimizations are summarized in Table 7.2 and Table 7.3.

Multiple optimizations for each parametrization were carried out to ensure that they converged into the global optimum. After optimization, spectra for the best individual were measured using a longer spectrometer integration time to determine the contrast for each optimization. The third-order phase, which only features two parameters, converged in the lowest number of generations.

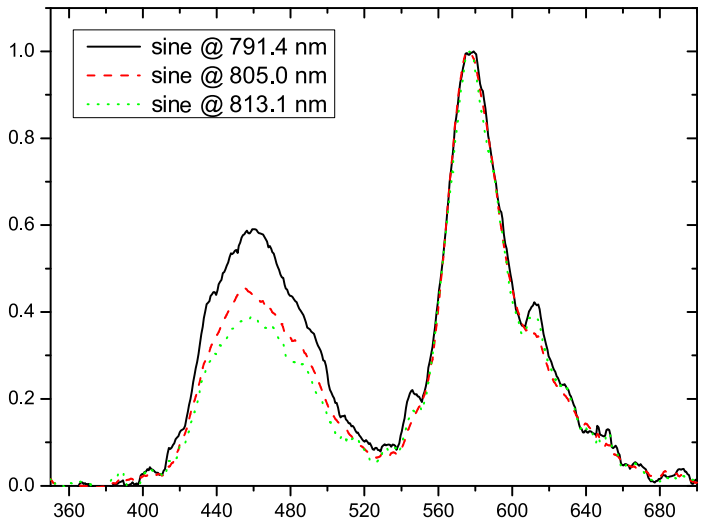

Figure 7.4: Exemplary spectra measured for pulses shaped with a sine phase antisymmetric around three different wavelenghts. These spectra were taken in line with the scan depicted in 7.3 and are normalized to 1 [67].

parametrization	best contrast	intensity	parameters
$A\sin(k(\lambda-\lambda_c))$	0.28	22.37 %	$\boldsymbol{A} = 17.2\,\text{rad}, \boldsymbol{k} = 0.059\,\frac{1}{\text{nm}}, \boldsymbol{\lambda_c} = 813\,\text{nm}$
$\frac{b_3}{6}(\omega-\omega_c)^3$	0.32	4.1 %	$\boldsymbol{b_3} = 7.94\times10^5\text{fs}^3, \boldsymbol{\lambda_c} = 823\,\text{nm}$
$\sum_{i=2}^{5}\frac{b_i}{i!}(\omega-\omega_c)^i$	0.33	4.72 %	$\boldsymbol{b_2} = -3.84\times10^4\,\text{fs}^3, \boldsymbol{b_3} = -1.46\times10^6\,\text{fs}^3$
			$\boldsymbol{b_4} = -5,23\times10^5\,\text{fs}^4, \boldsymbol{b_5} = 1.35\times10^9\,\text{fs}^5$

Table 7.2: Parameters found for optimized Rhodamine B fluorescence (larger contrast). The transform-limited pulse gives a contrast of 0.18.

parametrization	best contrast	intensity	parameters
$A\sin(k(\lambda-\lambda_c))$	0.09	22.99 %	$\boldsymbol{A} = 58.1\,\text{rad}, \boldsymbol{k} = 0.037\,\frac{1}{\text{nm}}, \boldsymbol{\lambda_c} = 791\,\text{nm}$
$\frac{b_3}{6}(\omega-\omega_c)^3$	0.08	8.8 %	$\boldsymbol{b_3} = 8.89\times10^5\text{fs}^3, \boldsymbol{\lambda_c} = 792\,\text{nm}$
$\sum_{i=2}^{5}\frac{b_i}{i!}(\omega-\omega_c)^i$	−0.004	10 %	$\boldsymbol{b_2} = -3.79\times10^4\,\text{fs}^2, \boldsymbol{b_3} = 1.67\times10^6\,\text{fs}^3$
			$\boldsymbol{b_4} = -4.33\times10^7\,\text{fs}^4, \boldsymbol{b_5} = 4.79\times10^8\,\text{fs}^5$

Table 7.3: Parameters found for optimized Coumarin 1 fluorescence (lower contrast).

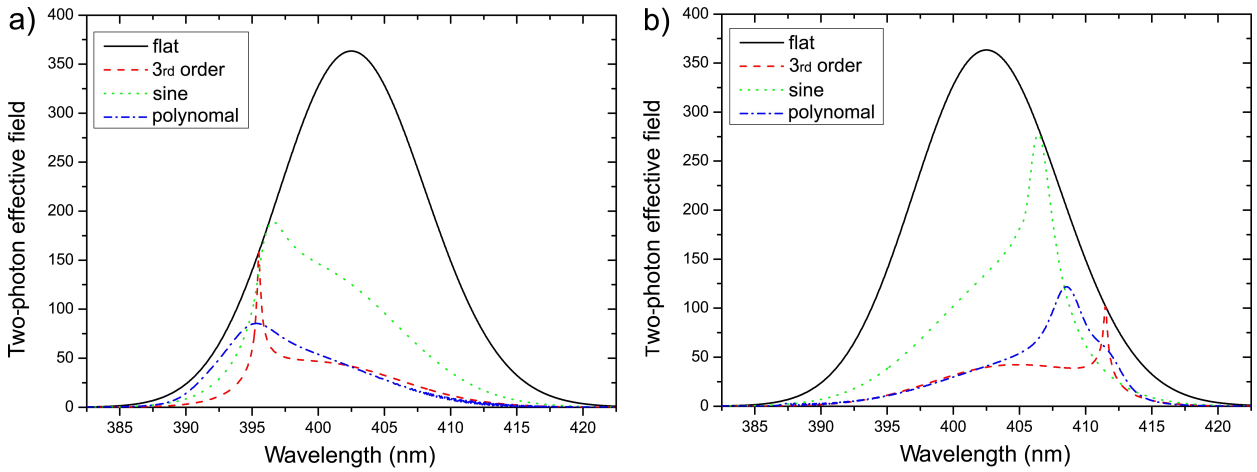

Figure 7.5: The graph shows simulated two-photon fields for the optimized parametric phase functions. It is can be seen that optimizations were able to find two-photon fields that match excitation of higher or lower transitions. Graph a) displays results for minimized, and graph b) for maximized contrast. The simple third-order phase function uses the spike, situated at the wavelength of antisymmetry, to shift the two photon spectrum to either higher or lower wavelengths. The step- and sine function appear to be beneficial when a reasonable fluorescence strength has to be retained. [67]

Although contrasts for both optimization goals were comparably large, the reduction in overall intensity was extreme. The fifth-order polynomial gave better contrasts and was able to use its higher parameter count to adjust the two-photon spectrum better to the TPA of both Coumarin 1 and Rhodamine B. Convergence on the other hand was relatively slow in comparison. The sine function did find the lowest contrasts but optimal pulses retained strong fluorescence intensity. To get an impression of the obtained results, Fig. 7.5 shows the two-photon fields corresponding to the parameters depicted in table 7.2 and 7.3.

This graph can help to illustrate the reason for the difference in total fluorescence intensity between the 3rd order phase parametrization and its contenders. The optimized fifth order polynomial allows for excitation of two-photon transitions on the lower end of the wavelength scale while minimizing excitation for higher wavelengths. While the high number of free parameters of the fifth-order polynomial phase were able to achieve the largest contrasts, the sine-phase parametrization is able to achieve comparable contrasts while retaining a lot of intensity with only three parameters. In further optimizations it was found, that an increased amount of parameters did not result in better contrasts. We can conclude that if mediocre contrast differences are sufficient the sine-phase parametrization is a useful parametrization which converges fast and does not suppress fluorescence as much as the other parametrisations tested here.

7.1.5 Solution Set

This optimization problem features conflicting goals. To achieve contrast between two fluorescence dyes the two-photon spectrum has to be modulated. This will inevitably lead to a reduction in overall fluorescence intensity $I_{tot} = I_R + I_C$. The space spanned by these two goals could be mapped by optimizations with an altered fitness function:

$$f = (I_R - I_C)^{\alpha}(I_R + I_C)^{\beta}. \tag{7.1.5}$$

Here, $\alpha \geq 0$ and $\beta \leq 0$ would define the importance of each goal. Unfortunately this would take a long time with the method of evolutionary optimization. To get a sense of this solution space, the

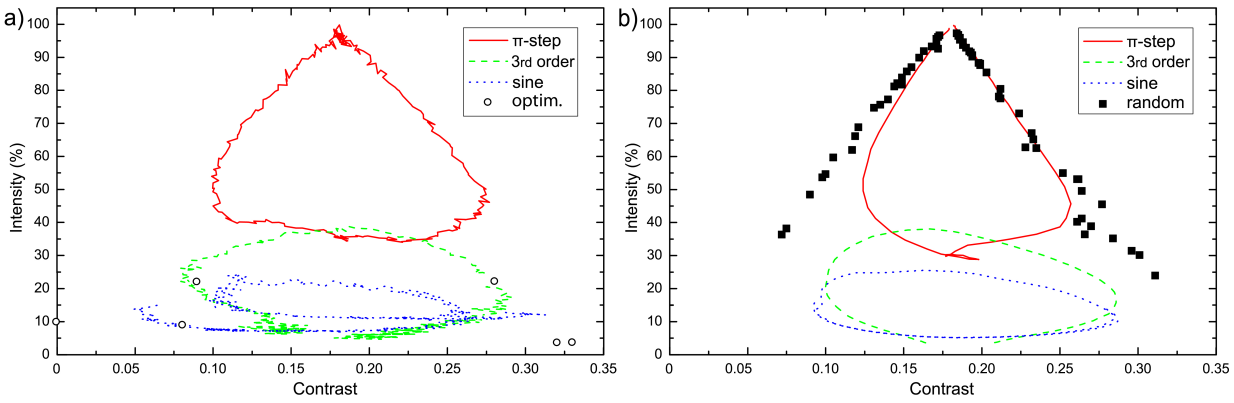

Figure 7.6: For all three phase scans, the total fluorescence intensity is plotted against the contrast. a) shows the scans from fig. 7.4 while circles mark the optimization results, b) depicts the corresponding simulations. In additional simulations, a large number of random phase functions were evaluated and their total fluorescence intensity and contrast calculated. Black dots mark solutions which were selected following the domination principle [78, 79]. [67]

phase scans from the previous chapter were plotted in Fig. 7.6. Experimental results were plotted in the left graph (a). Simulations of these scans were plotted on the right (b). In these graphs, the transform-limited pulse would achieve a contrast of 0.18 as well as total intensity of 100. A vast number of phase parametrisations could be devised, but it appears that they span a distinct area in the space of both conflicting goals.

The solution space seems to have a noticeable triangle shape. Phase functions seem to create solutions at an front which follows $dI_{fl}/dC = \text{const.} > 0$ for pulses optimized for Coumarin 1 and $dI_{fl}dC = \text{const.} < 0$ when contrasts are optimized for Rhodamine B fluorescence. The pi-step phase scan spans the top part of the graph, achieving mediocre contrasts at high overall intensities. Here one parameter is sufficient to select a phase function either resulting in larger contrast or signal. If larger contrasts are required optimizations with multiple parameters should be carried out. The differences between experimental data and simulations probably arises from the errors made during measurement of the TPA of the dyes. The question still stands whether phase-functions exist that can surpass contrasts and intensities found earlier by the three tested parametrizations. Hence, thousands of random phase-functions were evaluated in a simulation. Phases which fulfilled the domination principle were kept [78, 79], others discarded. This created a pareto-optimal front (black squares in fig. 7.6) which maps the space reachable by phase shaped pulses. It is surprising how close the pi-step phase function follows the possible range of solutions at high total fluorescence intensities. For low intensities higher contrasts than these found by parametric scans could be achieved.

7.1.6 Optical Properties of the Kagome Fibre

A Kagomé fibre relies on a different method of beam confinement than classical band-gap photonic crystal fibres. In a Kagomé fibre the band-gap is orientation dependent which allows for transmission of a broad spectral range. Its unique properties which include extremely low dispersion and nonlinearity make it an ideal candidate for endoscopic applications where high intensity pulses are required. In contrast to the Hollow-core fibre, this fibre's core is not covered by a glass window which in principle will allows the use of amplified pulses. An end cap with a window glued to its front was built to ensure that no dust enters the fibre. Light was coupled into the fibre with a $15\,cm$ lens and re-collimated after the fibre with another lens ($f = 30\,cm$). PRISM-phase

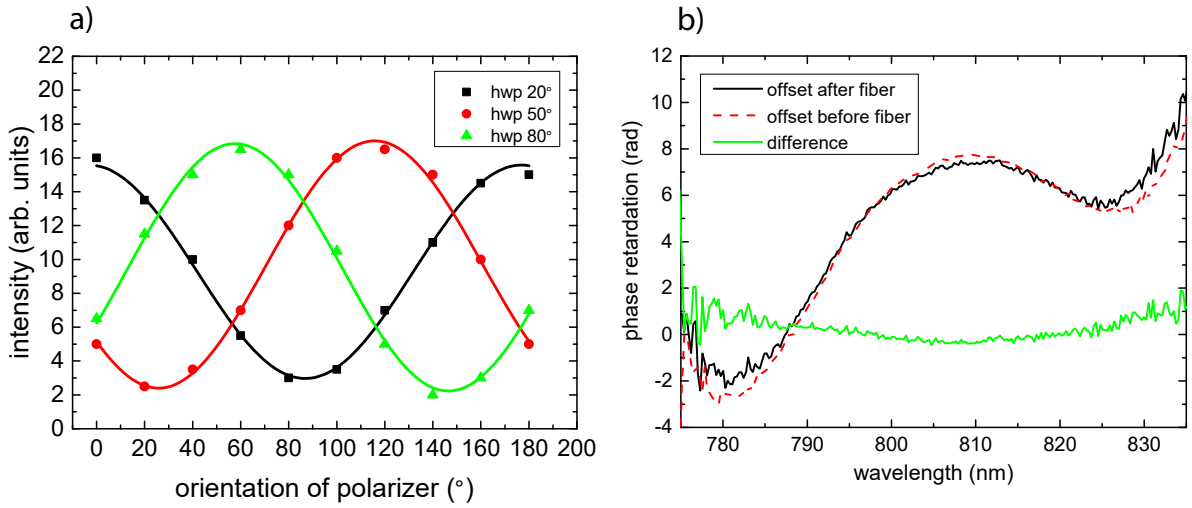

Figure 7.7: a) Ellipticity of a pulse measured for incoming linear polarized pulses rotated by a half-waveplate. b) Phase compensation found for directly before and after the Kagomé fibre. The difference amounts to the fibre's dispersion.

measurements were performed using a nonlinear detector just before and after the fibre. Fig. 7.7 b) shows the difference between both PRISM-offsets used for compensation and the difference which corresponds to the fibre's dispersion. A fit around $805\,nm$ gave a total fibre induced chirp of $-406\,fs^2 \pm 20\,fs^2$ and $7000\,fs^3 \pm 1100\,fs^3$. Another fibre property is birefringence. While the Hollow-core fibre showed strong birefringence, the Kagomé fibre appears to have no influence on the pulse's polarization state. Fig. 7.7 b) shows that linear polarized light entering the fibre under varying angles is still linear polarized after transmission through the fibre. This implies that no distinguished fast or slow axis exist that would have an influence on the polarization of the transmitted pulse.

7.1.7 Polarization Shaped Laser Pulses for Selective Two-Photon Fluorescence Excitation after a Kagomé Fibre

A pulse with a spectrum centered around $805\,nm$ and a spectral width of $32\,nm$ was shaped using the method specified in chapter 4.3.2. Thereby, two perpendicular polarization components can be independently phase-shaped. The polarization shaped pulses were coupled into the fibre and were then focussed into a cuvette filled with a mixture of the two fluorescent dyes. A fluorescent dye which is excited by linear polarized light usually emits light in the same polarization it was excited. If no internal charge transfer leads to a polarization change of emitted light, the polarization of the fluorescence solely depends on two factors. A longer lifetime of an excited state allows the molecule to rotate, which leads to the emission of slightly depolarized light. The second factor is the average rotational speed of the molecules. This is influenced by temperature and viscosity of the dye's solution. Rhodamine B and Coumarin 1 were solved in Glycerol to inhibit movement of the molecules maximizing their fluorescence anisotropy. Fig. 7.8 a) shows a measurement of Rhodamine B and Coumarin 1 anisotropy. Fluorescence anistoropy is defined by

$$a = \frac{I_{\parallel} - I_{\perp}}{I_{\parallel} + 2I_{\perp}}, \tag{7.1.6}$$

where $I_{\parallel}$ and $I_{\perp}$ are fluorescence intensities parallel and perpendicular to the exciting polarization direction. A half-waveplate in front of a polariser was rotated and spectra recorded. From these

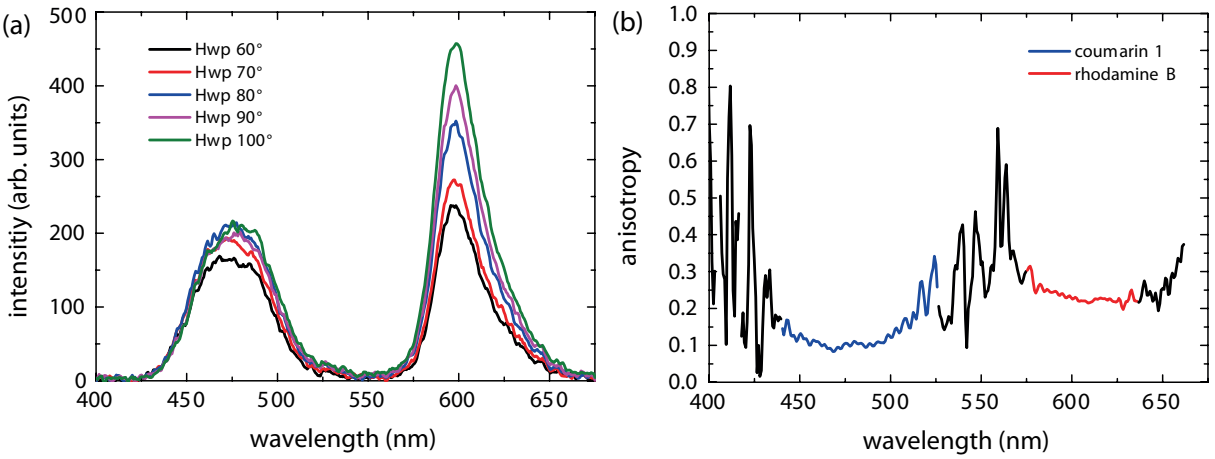

Figure 7.8: Polarization anistropy calculated from spectra taken for various positions of a polarizer between cuvette and spectrometer [68]

spectra we computed the anisotropy over the spectral range. Fig 7.8 b) suggests reasonable values for the anisotropy of both dyes. For Coumarin 1 a slightly lower anisotropy was measured. This might originate from the smaller size of Coumarine which causes faster rotation compared to Rhodamine. It is of interest if this anisotropy could be used by two perpendicular phase shaped laser pulses to create selective fluorescence in either polarization of the detection. Therefore, a phase which amounts to the compensation found by PRISM in addition to an antisymmetric second order chirp term of the type $\varphi(\omega) = \frac{b_3}{6}(\omega - \omega_c)^3$ were written on the shaper. The antisymmetric phase on Array A was chosen to be optimal for Coumarin fluorescence ($\lambda_c = 797\,nm$), while Array B was optimized for Rhodamine B fluorescence ($\lambda_c = 813\,nm$). Then, pulses were focussed in the cuvette and the spectra were recorded by a spectrometer and a polariser in line with the beam. A half-waveplate was rotated and the polarization dependent fluorescence captured. As before, resulting from the difference in concentrations and the problem that turning the waveplate in front of the fibre slightly changed the efficiency at which the beam is coupled into the fibre, the fluorescence intensities were normalized by that of the transform-limited pulse. When the perpendicular polarized double pulse is oriented such that the pulse optimized for Rhodamine is parallel to the polariser in front of the spectrometer, then one will expect a contrast of:

$$c_{max} = \frac{I_R^{(1)} + \beta_R I_R^{(2)} - I_C^{(1)} - \beta_C I_C^{(2)}}{I_R^{(1)} + \beta_R I_R^{(2)} + I_C^{(1)} + \beta_C I_C^{(2)}}. \tag{7.1.7}$$

Here, $I_R^{(2)}$ would refer to the fluorescence intensity of Rhodamine originating from excitation by the pulse which was optimized for Coumarin fluorescence. $\beta_{R/C} = (1-a)/(2+a)$ denotes the ratio of fluorescence which gets emitted perpendicular to the excitation for a given dye. The same can be calculated for the minimal contrast:

$$c_{min} = \frac{I_R^{(2)} + \beta_R I_R^{(1)} - I_C^{(2)} - \beta_C I_C^{(1)}}{I_R^{(2)} + \beta_R I_R^{(1)} + I_C^{(2)} + \beta_C I_C^{(1)}}. \tag{7.1.8}$$

Measured, and calculated contrasts are plotted in Fig. 7.9. Calculated contrasts which were derived from the equations for c_{min} and c_{min} are matched well by the measurements. As the anisotropy measurements reveal (fig. 7.8), the spectrometer will always capture fluorescence originating from both orthogonal pulses, not matter how the polariser in front of the spectrometer is oriented. Despite this fact, reasonable contrasts were achieved. The inset in the upper right corner depicts the

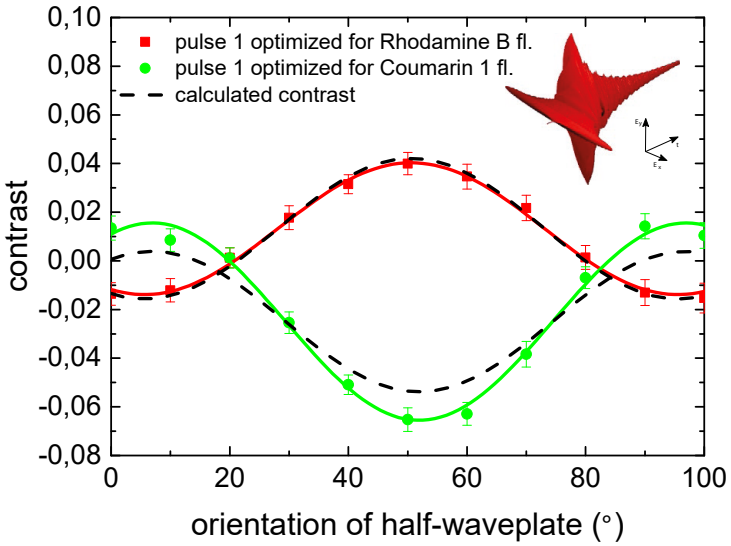

Figure 7.9: Demonstration of selective excitation using a polarization shaped laser pulse. By using two differently phase shaped perpendicular polarized pulses, polarized fluorescence was evoked. Turning a polariser in front of the detector can then be used to choose between stronger Rhodamine B or Coumarin 1 fluorescence. [68]

phase shaped perpendicular polarized double pulse which was used in this experiment. The dominant feature seen in this illustration arises from the strong quadratic chirp, used for shifting the two-photon field in either direction.

7.1.8 Conclusion

In this chapter phase shaped pulses were used to selectively excite two fluorescent dyes after transmission through two fibres. It was demonstrated that by precompensating pulses, phase shaped pulses can be used in fluorescence experiments on the rear end of photonic-crystal fibres. Phase functions, which can be beneficial for the modulation of the two-photon field, were analysed. Parameter scans gave insight on the solution space spanned by two conflicting goals (retaining a large amount of fluorescence intensity, while increasing the fluorescence contrast as much as possible). In the parametric phase scans, the third-order phase function outperformed the sine-parametrization. The phase-step function did not achieve comparable contrasts able to maintain a strong fluorescence signal from both dyes. These results are in line with simulations of the two-photon field depicted in Fig.7.1. The parameters (chirp, step size, amplitude) which defined the earlier phase functions were manually selected. Therefore, evolutionary optimizations were used to find parameters for a series of phase functions which would be optimal for either Rhodamine B or Coumarin 1 fluorescence, while at the same time inhibiting fluorescence of the other dye. The largest contrast was found by the polynomial phase parametrization. But a phase-step was surprisingly effective for high intensity results. Optimzations were found to be applicable for finding phase functions which could lie on the pareto-optimal front defined by both conflicting goals. Furthermore a novel type of fibre was studied. This Kagomé fibre was found to feature extremely low dispersion and have nearly no influence on the polarization state of a incoming laser pulse. Two perpendicular polarized phase shaped pulses were created with the SLM. One was optimized for maximal and one for minimal contrast. While rotating the polarization of the double pulse with the help of a waveplate in front of the Kagomé fibre, the polarized fluorescence spectrum of

Rhodamine B and Coumarine 1 in glycerol was recorded. Since both dyes show strong fluorescence anisotropy, it was possible to show that solely rotating the waveplate and thus the double pulse before the fibre could be used to maximize Rhodamine or Coumarin fluorescence at a given polarization. This method to control two-photon excitations should in principle be applicable to all anisotropic fluorescent molecules which possess a different slope in two-photon absorption in the spectral range of the exciting laser pulse. These results could hence be useful in endoscopic applications, or could be applied to enhance two-photon fluorescence excitation microscopy. The kagome fibre allows for much higher pulse energies than those applied in the outlined experiment. This would permit further experiments at intensities required for three-photon excitation.

7.2 Influence of Nonlinear Effects on the Three-Photon Excitation of L-Tryptophan

7.2.1 Preliminary work and Introduction

Two-photon fluorescence is already a valuable tool in biological research and medicine. The previous chapter (7.1) discussed how photonic crystal fibres can be used to deliver phase or even polarization shaped pulses to selectively excite two-photon transitions in endoscopic applications. While two-photon fluorescence microscopy, due to it's intensity dependence, can achieve higher resolution images as well as depth scans, three-photon excitation increases this effect even further [80]. Three-photon excitation which requires even higher laser intensities to become efficient, could in principle be also achieved after transmission through a hollow-core fibre. In this chapter, we will explore the effect of phase shaping on three-photon fluorescence excitation of the amino acid Tryptophan. Benefits of exciting Tryptophan directly via three IR photons is again the increased penetration depth of the exciting light as well as the fact that Tryptophan occurs naturally in biological systems. Non-invasive three-photon excitation in vivo was demonstrated by Horton et.al. [81] who produced stunning 3D images of red fluorescent protein-labelled neurons in a mouse brain. Many marker substances were analysed [82] but the use of UV autofluorescence would protect the sample of this contamination. Tryptophan, Phenylalanin, Tyrosin and Histidin all are aromatic compounds and thus can be used in fluorescence experiments. Of these four Tryptophan shows the most efficient fluorescence. As one of the required amino acids for human life the properties of Tryptophan were studied extensively [83, 84]. Chen et.al. studied in 2004 if pulse shapes could be used to optimize a fluorescence ratio of two and three-photon processes [85]. In these experiments engineered fitness functions were used to find pareto optimal results for simultaneous two and three-photon fluorescence. Results seem to favour transform-limited pulses when higher-order excitation was prioritized, while trivial results were found for cost functions which optimized two-photon fluorescence. Unfortunately these optimization were carried without any phase parametrization and hence hard to interpret. In this chapter we will look at the benefits of pulse shaping for three-photon excitation. Since intensities required for this kind of process are relatively high, nonlinear effects will occur at the focus. Tryptophan solved in water was selected as biological relevant system and simulations of the evolution of the pulse within the cuvette will be compared to experimental results. Finally we will examine whether nonlinear effects and pulse shaping could be exploited to selectively excite naturally occurring fluorophores in future microscopy applications. Experiments presented here have been published in the context of my theses in the Journal of the Optical Society of America B [86].

7.2.2 A Model for Nonlinear Pulse Propagation in a Fluorescence Setup

In contrast to the experiments conducted earlier, only amplified pulses offer the high intensities required for three-photon excitation. The RegA (see chapter 5.1.2) amplifier provides pulses of $\sim 3\,\mu J$ at a rate of $287\,kHz$. The spectrum was tuned to a central wavelength of $805\,nm$ while the spectral width was reduced by the amplification process to $22\,nm$. A grating compressor in between the amplifier and pulse shaping setup compressed the pulse to a length of $58\,fs$. The pulse length was measured with the autocorrelator introduced in chapter 5.3.1. After the pulse shaping setup, which was set up to allow for simultaneous amplitude and phase modulation, the beam was focussed into a glass cuvette by means of a ($f = 20\,cm$) focussing lens. The $12\,mm$ long cuvette had a wall thickness of $1\,mm$ and contained 15mM L-Tryp in v.e. water. The focus was adjusted to lie exactly in the centre of the cuvette (at a depth of $6\,mm$). Pulse energies were

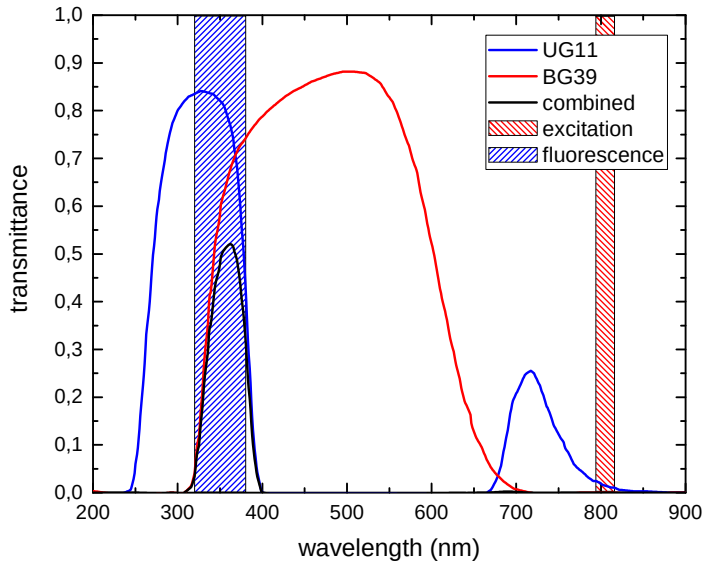

Figure 7.10: This graph shows the transmittance of the employed glass filters BG38 and UG11. Their combined use is particularly suitable for removing stray IR and visible light from the Tryptophan fluorescence signal. Transmittance data was extracted from [87].

so high that in the cuvette walls, the slightly focussed light was intense enough to provoke white light generation. With the help of neutral density filters the maximal laser power was limited to $0.7\,\mu J$, preventing white light generation in the glass. Here, even if the threshold for white-light generation is undercut, it is clear that the glass (e.g.: also the glass in microscopy application) will have a strong influence on the propagation and thus selectivity of shaped pulses if these high pulse intensities are employed. Two lenses were used to focus light (emitted sideways) from the cuvette into a photomultiplier tube, while a spectrometer was placed in the direction of beam propagation to monitor nonlinear changes of the pulse spectrum after the cuvette. Two filters (UG11, BG39) were used to select Tryptophan fluorescence and minimize the signal from stray IR light detected by the photomultiplier (see fig. 7.10).

The phase offset which can be used to create a transform-limited pulse at the focal point in the cuvette could not be found by using Tryptophan fluorescence as a signal, as nonlinear effects like self-steepening can change the offset phase required. Hence, Rhodamine B solved in v.e. water was used as nonlinear fluorescence signal fed back to the PRISM algorithm. The phase compensation found for the fluorescence optimization as well as a iteration of PRISM on the signal of a two-photon diode at the cuvette's position were compared. The difference of both phases was appropriate to that of a cuvette and a lens (The only difference in the optical path for both PRISM runs). This validates that only linear dispersion was compensated by this offset phase.

A reduced model of the pulse propagation method discussed in chapter 6.2 was used for this setup to predict the change of the spectrum due to nonlinear effects in the focus. The simulation took account of dispersion, self-phase modulation and self steepening. At each propagation step of the Split-step Fourier method the intensity of the beam was re-evaluated according to the experimental conditions (focal length, original beam diameter, beam power) to account for the fact that nonlinearities occur primarily close to the focal point. The simulation of the pulse-propagation was initialized at the beginning and terminated at the end of the cuvette. So at each step, either the material properties (consisting of a set of GVD, TOD and the nonlinear refractive index n_2

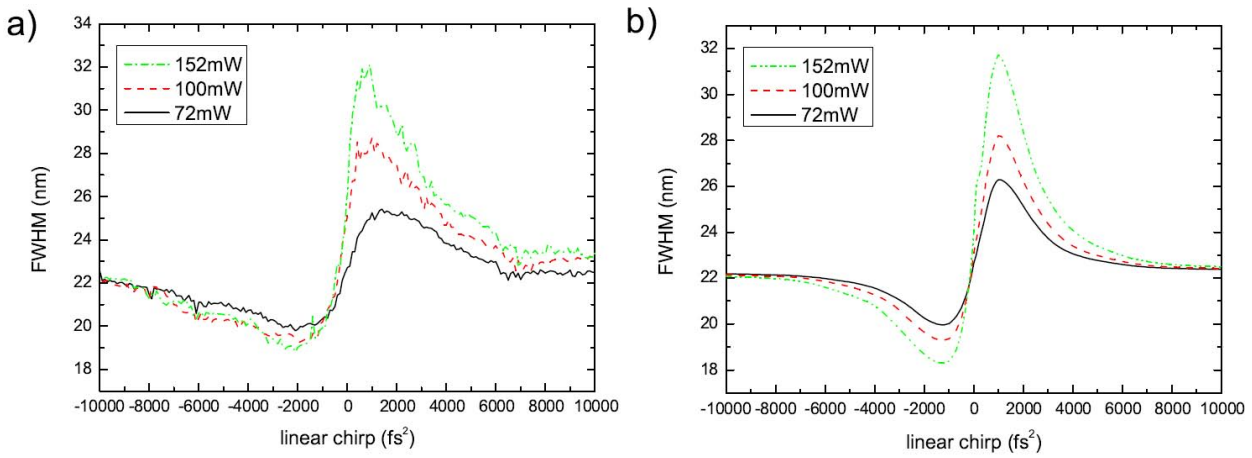

Figure 7.11: a) Measured FWHM of the pulse spectrum after the cuvette plotted against the linear pulse chirp which was added to the compensation phase. Three scans were performed for a pulse power of $72, 100$ *and* $162\,mW$*. b) Simulations of the SPM induced spectral broadening (and narrowing) for a input pulse with a central wavelength of* $805\,nm$ *and a spectral width of* $22\,nm$*.*

[88, 89, 90, 91]) of quartz glass or water were selected. This is required, since the nonlinear refractive index, as well as dispersion are significantly larger in quartz than in water. Propagation in air was neglected due to the same reasoning.

For selective excitation a third-order phase function was selected. This phase parametrization offers the advantage that the effect not only on the three-photon field but also on the temporal pulse shape of a third-order phase is well understood. A third-order phase, antisymmetric around a frequency ω_c

$$\Phi(\omega) = \frac{b_3}{6}\left(\omega - \omega_c\right)^3, \tag{7.2.1}$$

equals a quadratically chirped pulse. When ω_c coincides with the central frequency of the laser spectrum the pulse is simply quadratically chirped by the value of b_3. Although, a central frequency which differs from ω_c will result in a linearly and quadratically chirped pulse which can be easily seen by performing a Taylor expansion of $\Phi(\omega)$ with respect to ω_0. All these pulses feature an asymmetric pulse profile which will have a distinguished effect when self-phase modulation is considered. A third-order phase with significantly lower value than that of the previous chapter was chosen. This is sensible since the efficiency of three-photon fluorescence is proportional to $\propto I(t)^3$.

As a simulation of SPM and self-steepening depends on the factor ($n_2 \times$ I), both the nonlinear refractive index of the material as well as the pulse shape and power have to be known exactly. The beam power was measured with a power meter. As these are quite imprecise, it is reasonable to check whether SPM and self-steepening are correctly modelled. A comparison of the FWHM, measured and simulated, of the spectrum after transmission through the cuvette is given in fig. 7.11.

Literature values were used for the dispersion and the nonlinear refractive index of water and quartz. The simulations show a good conformance with the measurement. It can therefore be concluded that SPM and self-steepening are correctly modelled by the proposed simulation method.

Fig. 7.11 shows besides the well known spectral broadening another effect. Negatively chirped pulses for which shorter wavelengths arrive early and longer wavelengths are delayed experience a spectral shift towards longer wavelengths at the leading and a shift towards shorter wavelengths at the trailing edge of the pulse. This results in a reduced bandwidth after propagation through

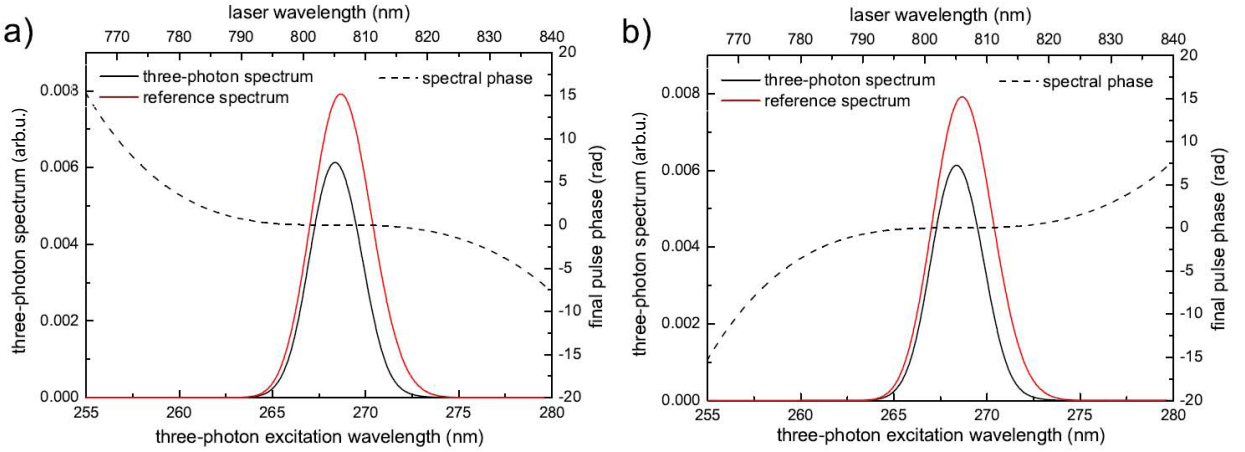

Figure 7.12: a) Three-photon spectrum for a positive third-order phase of $5 \times 10^4 fs^3$. b) The three-photon spectrum resulting from a negative third-order phase ($-5 \times 10^4 fs^3$) is equal to the positive case when effects like SPM and self-steepening are neglected. The red line stands for the three-photon spectrum of the transform-limited pulse.

a nonlinear medium as can be seen in simulation and measurement alike. It is easy to spot that this effect can result in pulse-shape dependent spectral changes which will have an influence on the spectrum and ultimately multiphoton excitation as well. Without nonlinear effects the three-photon spectrum for a quadratically chirped pulse does not depend on the sign of the chirp. Fig. 7.12 depicts the coinciding three-photon spectra for quadratic chirps of $\pm 5 \times 10^4 f^3$. Whereas the red line depicts the three-photon spectrum of a transform-limited pulse, based on the reference spectrum taken before the cuvette. For each precompensated pulse a simulation of the propagation was performed from the beginning of the cuvette up to the focus. The spectrum and spectral phase found at the focal point were then used to evaluate the three-photon spectrum according to eq. 4.5.3. While inverting the sign of the phase function does not change the simulated three-photon spectrum in the linear case, it should make a difference when nonlinear effects are taken into account. Fig. 7.13 shows this difference. Graph (a) and (b) can be compared to the linear simulations performed earlier: SPM results in a strong reduction of the efficiency in three-photon excitation. The asymmetry of the pulse shape during propagation in the cuvette thus leads to an asymmetric three-photon spectrum. As the input spectrum was centred at a wavelength slightly above $805\,nm$ the amount of reduction in efficiency is not equal for positive and negative third-order phases. The effect of a shifted point of antisymmetry can be seen in graphs (c) and (d) where λ_c was chosen to be $811\,nm$.

It can still be said that the point of antisymmetry defines the shape of the three-photon spectrum. When the point of antisymmetry is scanned from one side of the exciting spectrum to the other, the maximum of three-photon spectrum shifts just like it is the case for the two-photon spectrum (see Fig. 7.13). In the two-photon case this effect can still be understood analytically while for three-photons a double-convolution over the exciting IR spectrum ensures that every phase unequal to the flat phase will lead to a reduced three-photon excitation efficiency. A flat phase close to the point of antisymmetry for the third-order phase allows for constructive interference of photons around this wavelength. A rule of thumb for the shape of the three-photon spectrum is that the maximum will be situated at the point of antisymmetry while an overall reduction in efficiency will depend on the remaining peak intensity of the shaped pulse. The dominant effect on the spectral evolution of the pulses in the cuvette was SPM. Only small changes were spotted when self-steepening was disabled.

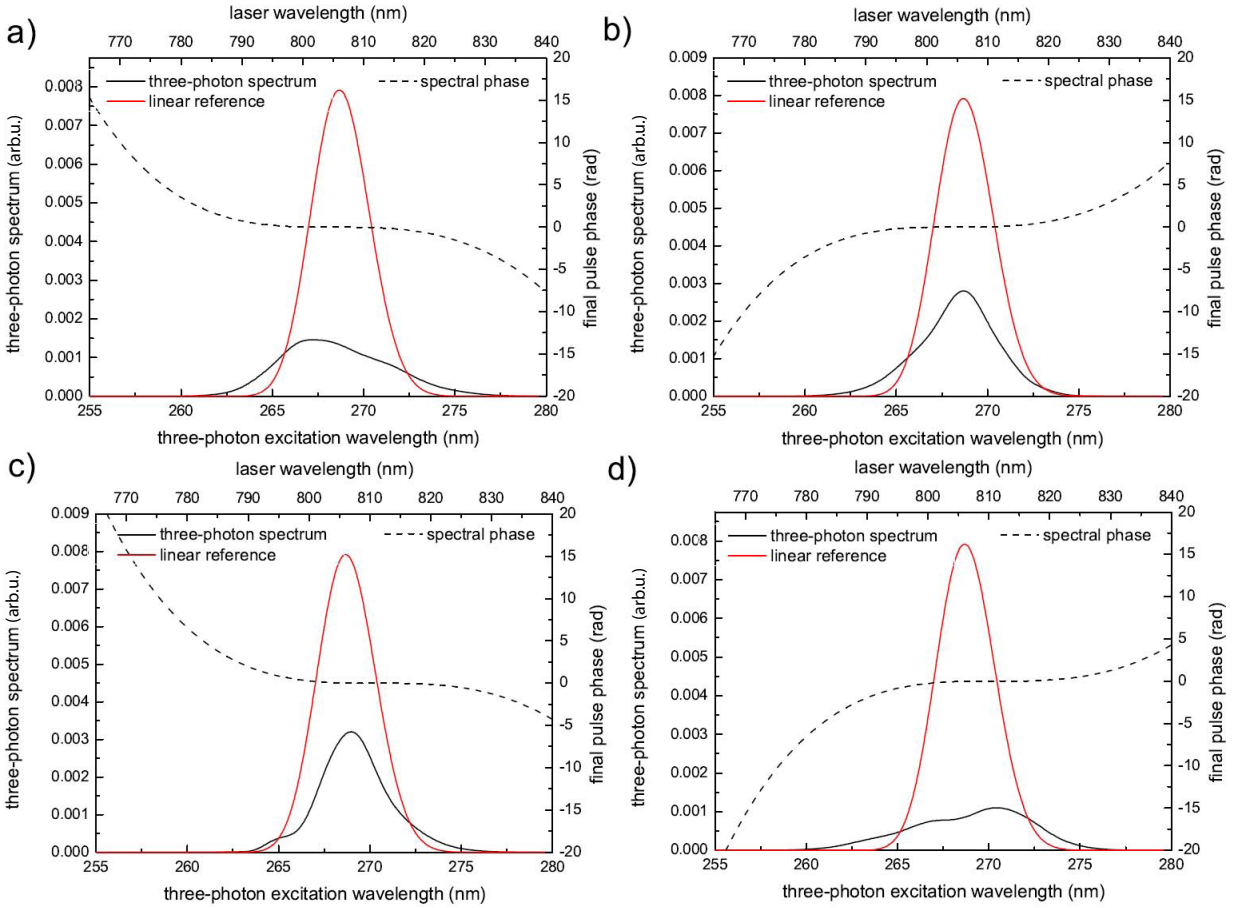

Figure 7.13: Simulations of the three-photon spectra after propagation of the pulse up to the focus. a) $+5 \times 10^4 fs^3$*, centre wavelength 805 nm, b)* $-5 \times 10^4 fs^3$*, centre wavelength 805 nm, c)* $+5 \times 10^4 fs^3$*, centre wavelength 811nm and d)* $-5 \times 10^4 fs^3$*, centre wavelength 811 nm. The difference of three-photon spectra for positive and negative phase coefficients is a result from self-phase modulation induced spectral changes.*

Another interesting effect was observed: Since pulses are precompensated to account for the dispersion of the cuvette and water up to the focus, pulses will be negatively chirped when propagating in the cuvette. On the way out pulses will be mainly positively chirped. We can consult fig. 7.11 for the effect of linear chirp on a chirped pulse. Although this simulation was carried out over the full length of the cuvette, the comparison still holds. Hence, pulses will experience spectral narrowing on the way towards the focal point and spectral broadening on the way out of the cuvette. This will result in an effectively reduced spectral width which would occur in all microscopy applications at these intensities.

It is worth to note that SPM cannot be used to create an overall frequency shift by itself. The frequency shift at each time induced by SPM can be written as:

$$\delta\omega(t) = -n_2\omega_0 \frac{L}{c} \frac{\partial}{\partial t} I(t), \tag{7.2.2}$$

where L is the length of the material. and $I(t)$ is the tempoal intensity of the laser pulse. When integrating the frequency shift $\delta\omega(t)$ from minus to plus infinity we find:

$$-n_2\omega_0 \frac{L}{c} \int_{-\infty}^{\infty} \frac{\partial I(t)}{\partial t} dt = -n_2\omega_0 \frac{L}{c} I(t)|_{-\infty}^{\infty} = 0. \tag{7.2.3}$$

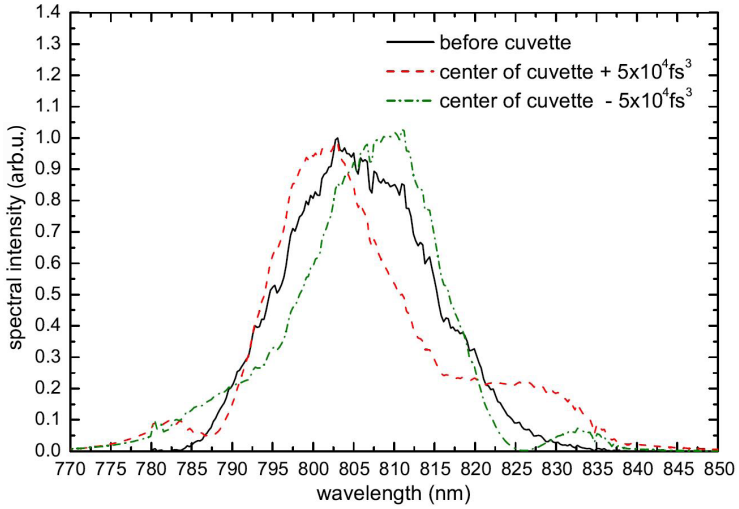

Figure 7.14: Simulation of the spectral changes due to SPM and self-steepening up to the focus position in the cuvette for a third-order phase of $\pm 5 \times 10^4 fs^3$ centred around 805nm. The simulation is initialized with a reference spectrum taken before the nonlinear medium (solid black line).

that indeed no overall frequency shift is possible. Asymmetric pulse shapes can nonetheless lead to asymmetric modulations of the pulse spectrum.

The fluence at the laser's focus reaches $76mJ/cm^2$. At this point a positive quadratically chirped pulse has a steep leading and a shallow trailing frank. As can be seen from eq. 7.2.2, a steep flank results in a strong shift while a shallow flank will create a broad band shifted only slightly. In combination with dispersion and self-steepening the induced spectral changes can be rather complex, thus simulations are best to look at the spectral changes as they occur in the focus.

7.2.3 Shaped Laser Pulses for Selective Three-Photon Excitation Utilizing Nonlinearities in a Cuvette

In the focus, where the laser fluence reaches values of $76mJ/cm^2$, the pulse that is shaped with a third-order phase has a steep leading flank and shallow trail or vice versa. In combination with the varying instantaneous frequency within the pulse a rather complex spectral change arises. Since this is unique for each shifted spectral phase, simulations will give the best insight into the expected spectral changes. This effect can be observed when looking at the simulated spectra in the focus of the cuvette.

Fig. 7.14 depicts an example of the nonlinear spectral changes of $1\,mm$ quartz and $5\,mm$ water for two differently shaped pulses. One clearly sees the spectral narrowing as well as the asymmetric shift resulting from the asymmetric pulse shape. Pulse-shape dependent spectral changes can be used in addition to methods described in the previous chapter on two-photon excitation to optimize selective excitation in high intensity applications.

In fig. 7.15 fluoresence intensity of Tryptophan in water was measured while shifting the point of antisymmetry for both plus and minus $5 \times 10^4 fs^3$. These two scans were then repeated for different power levels which were set via amplitude modulation with the pulse shaper. The separation of the maxima for positive and negative chirped pulses increases for rising intensities, as effects due to self-phase modulation become more and more prominent. A positive third-order phase which corresponds to a pulse with a steep leading flank seems to shift the scans maximum to longer wavelengths. This at first contradicts the results from fig. 7.14 where the spectral maximum

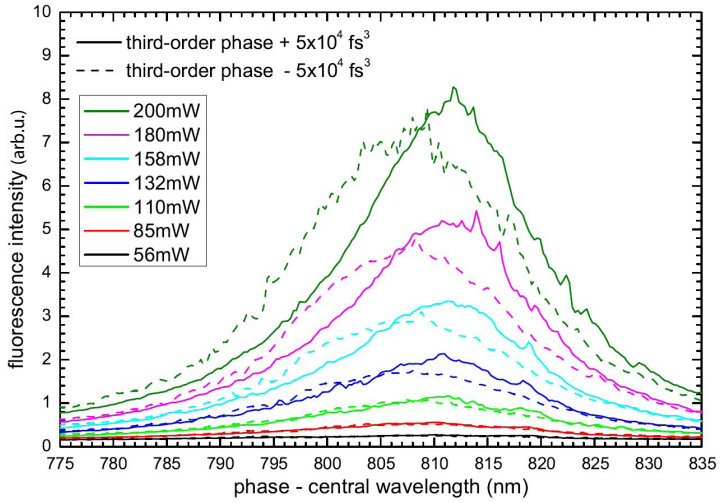

Figure 7.15: Measured Tryptophan fluorescence for a scan of the wavelength of antisymmetry for a third-order phase function at various pulse energies. At higher beam powers, a split between the curves for positively and negatively shaped pulses starts to emerge.

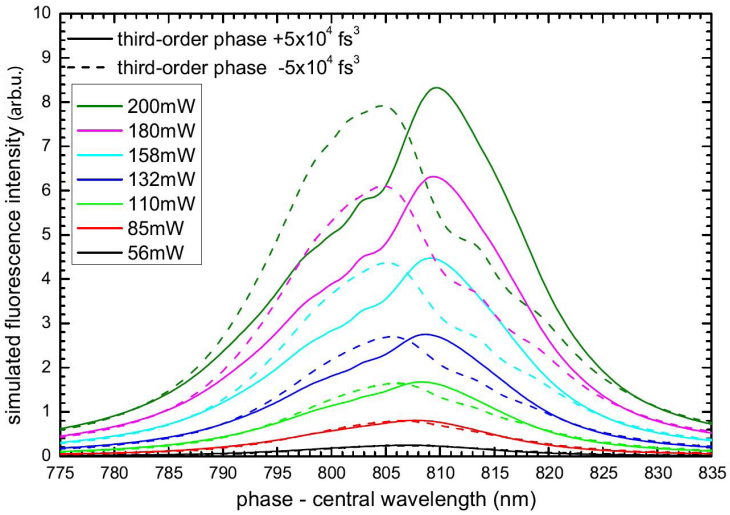

Figure 7.16: Simulation of Tryptophan fluorescence which included the intensity change during propagation due to the Gaussian beam focus, SPM self-steepening and dispersion. Simulations are based on literature values for GVD, TOD and n_2 while the simulation was initialized by a reference spectrum taken before the cuvette as well as measured values for the beam diameter and power. The simulation confirms the results from fig. 7.15: A split emerges for higher pulse energies confirming that SPM and self-steepening have a strong influence on multiphoton excitation in fluorescence setups.

is shifted to lower wavelengths. Important for the process of three-photon excitation is not the maximum but the band shifted to higher wavelengths, allowing for constructive interference of three-photons at higher wavelengths in the case of positive third-order phase shaped pulses. For intensities of $85\,mW$ and less this effect is nearly gone. From these measurements we can conclude that a positive third order phase that features a point of antisymmetry at higher wavelengths will be appropriate for excitation at longer wavelengths, while a negative third-order phase shifted to lower wavelengths should be used for shorter wavelength optimized excitation. Simulations match the measurement well (see fig. 7.16). The same separation for positive and negative phases can be observed. Here again nonlinear effects are negligible for scans below $85\,mW$. The simulation

is based on only literature values or measurements of the beam power, beam diameter and initial spectrum performed prior to the experiment. Since no three-photon absorption data for tryptophan was available, one photon absorption spectra were used to calculate the total fluorescence intensity from the three-photon spectrum [60]. This is a sensible simplification since both processes share some selection rules.

7.2.4 Conclusion

The path from last chapter's selective two-photon to selective three-photon excitation made clear that nonlinear spectral changes will have a great influence on multiphoton fluorescence excitation by shaped pulses. The good agreement between experiment and the simulation, which was based only on literature values, encourages that a correct model of the underlying processes can be used to effectively predict pulse shapes for optimal control of this excitation process. In microscopy applications, the optical setup might be different but intensities required for three-photon excitation stay the same. Three-photon excitation and self-phase modulation are inherently coupled since both are $\chi^{(3)}$ processes. Chapter 7.1 demonstrated how selective excitation can be achieved by phase shaped pulses after a hollow core fibre. As kagomé fibres open up intensity ranges which allow for three-photon excitation endoscopic applications come into reach. Here, the knowledge of the way nonlinear changes occur in the focus could be used to further increase fluorescence contrasts. Three-photon fluorescence excitation microscopy allows for depth scans, higher resolution and the use of autofluorescence of biological tissue as it was shown for Tryptophan in the experiments conducted here. From the work presented in this chapter, we can conclude that compensation or at least modelling of the nonlinear effects which occur during three-photon excitation processes can result in improved fluorescence or selectiveness in a wide range of applications.

7.3 Spectral Changes after Filamentation Controlled by Shaped Whitelight Pulses

7.3.1 Preliminary Work and Introduction

Ultrashort laser pulses are the method of choice when exploring very fast atomic or molecular processes. Particularly, few cycle whitelight laser-pulses generated by filamentation in gas or in hollow-core fibres are beneficial for measurements with high temporal resolution [92, 93]. These pulses, which can be as short as $5\,fs$, are employed to observe electronic wave packets [94] while specificly tailored pulse sequences were used to demonstrate that excitation pathways can be selected so that ionisation [7, 95], dissociation [6, 96], or fluorescence [97] can be controlled. Just recently, shaped whitelight laser pulses were firstly used to optimize the ionisation ratio of differently sized small Silver clusters [98]. These optimal pulse shapes are usually found in a closed loop optimization scheme. Filamentation in gases is in itself an intriguing process involving dispersion, multiple nonlinear and spatial effects, as well as ionisation dynamics. To allow for the necessary cancellation of self-focusing and plasma defocusing one requires either high powered lasers or extremely short pulses. Although a white-light supercontinuum is sometimes created using thin sapphire plates [42, 43], in the experimentes presented here a high powered Ti:Sa Laser system and a two-stage filamentation in air is employed to create the broadband spectrum. This method has the advantage of providing comparably high pulse energies. The ionisation process on the other hand depends strongly on the pulse's peak-power, wavelength and the gase's ionisation potential. Here, the widely used Keldysh parameter [99] can be employed to tell, whether ionisation follows mainly multi-photon ionisation (MPI) or tunnel-ionisation (TI). In filamentation experiments, spectral blue shifting [100], temporal pulse breaking [101] and filamentation over long distances [102] have been observed. Theoretical models which were developed to account for these effects recently allowed for the simulation of filamentation and pulse propagation and thereby helped to understand the complex dynamics resulting from the interplay of spatial and temporal effects. Filamentation is a highly nonlinear process and thereby relies even more strongly on the incoming pulse shape than the previously discussed three-photon excitation. Studies of the influence of basic linear chirp and the interplay of the temporal and spatial focus of the filament allowed to shift and control the onset of the filament in space [103]. In this chapter the influence of the pulse shape on the resulting spectra after filamentation in rare gases will be studied. The laser system with pulse shaping [104] unit allows to arbitrarily change the phase and amplitude of supercontinuum white-light laser pulses. Comparison of the obtained spectra from simulations and experiment of the pulse propagation after the filament will be used to understand the interplay of all relevant effects and give guidance on how to control spectral features after filamentation by carefully tuning the pulse parameters pre-filamentation. The pressure chamber used in this chapter was built during a cooperation with the experimental group of Prof. Jean-Pierre Wolf from the Université de Genève.

7.3.2 Filamentation Triggered by Ultrashort Whitelight Laser Pulses

Filamentation is a process in which a multitude of separate effects are involved. Their numerical description was discussed in chapter 4.6, while chapter 6.2 concentrated on the actual implementation of these properties in the simulation. Additionally, some simple examples for pulse propagation were shown when single effects were included or neglected during the simulation. We

will now discuss which effects are relevant for propagation in the regime set by the experimental conditions and which effects in turn should be neglected to achieve a reasonable simulation speed.

Generally, pulse propagation in a filament depends on the bound electron and plasma response of the propagation medium on the laser pulse. This response can be distinguished in a linear and nonlinear polarizability. The linear part of the bound electron response which is not dependent on the electrical field is responsible for dispersion. The nonlinear bound electron response will lead to effects like self-focussing, self-steepening and self-phase modulation which are governed by the so called nonlinear refractive index n_2. The nonlinear refractive index of Argon is smaller ($n_2 = 1.05 \times 10^{-19}\, cm^2/W$[105]) than that of Krypton ($n_2 = 2.5310^{-19} cm^2/W$[106, 107]). It was shown that the nonlinear refractive index, although intensity [108] and wavelength dependent [106], simply increases linearly with pressure [109]. When the laser beam reaches power-levels higher than the critical power (eq. 4.6.55) self-focussing overcomes diffraction leading to a beam collapse. The critical power is a function of n_2 and thus differs for Argon and Krypton. Here Argon requires a larger power for self-focussing ($0.804\, GW$, at $761\, nm$ and $9\, bar$) than Krypton ($0.318\, GW$, at $761\, nm$ and $9\, bar$). When the beam collapses, intensities get so high that ionisation by either tunnel or multiphoton ionisation will occur. The plasma generated acts as a defocussing element which quickly overcomes self-focussing. This can lead to repetitive focussing and defocussing of the beam over large distances as described in various publications [110, 111]. This is not possible under the experimental conditions here, where a strong focussing of the beam will ensure that only a single, relatively short filament will be created. During propagation, the pulse will ultimately loose energy due to the ionisation process.

Concerning the simulation, it is important to discuss the choice of the coordinate space. The propagation of pulses close to the focus was simulated using a 2D cylindrical coordinate space $E(r, z)$. For solving the NLSE a variant of the Split-Step Fourier method [28] was implemented. In addition, after each nonlinear step, a fast Hankel-transform is applied. Thereby, the spatial propagation for a small step in z-direction amounts to a simple phase added in k-space. This reduction of dimensionality was necessary to keep the required computing time in a feasible range. An off-axis focussing mirror was used in the experimental setup such that the focus was not distorted by the small angle required for separating the reflected, focussed beam from the incoming beam. The experimental conditions therefore did not favour any radial direction which was also verified by the radial symmetry of the beam after exiting the chamber. At far bigger beam intensities than these studied here, filament breakup could occur which would make a 3D description necessary [112].

As Sprangle et al. state in their paper [37] the complete evolution of pulses in filaments is governed by the source terms:

$$\mathbf{S} = \mathbf{S}_L + \mathbf{S}_{NL} + \mathbf{S}_{Raman} + \mathbf{S}_{plasma} + \mathbf{S}_{wake} + \mathbf{S}_{rel} + \mathbf{S}_{ion} \tag{7.3.1}$$

While the linear polarizability ($\mathbf{S}_L$), the optical Kerr-effect ($\mathbf{S}_{NL}$), Plasma effects ($\mathbf{S}_{plasma}$) and energy depletion due to ionisation ($\mathbf{S}_{ion}$) were included in the simulation, effects due to Raman stimulation, plasma wakefield interactions and relativistic corrections were neglected in accordance with the following considerations:

While Raman scattering will occur at the intensities and pulse lengths employed here, the response on the nonlinear refractive index by excitation of vibrational states will occur after a characteristic time for the Raman process $\approx \tau_r = 1/\omega_r$. It was found that this time for short pulses is in the order of $62.5\, fs$ [37] which is larger than most pulses studied in the experiments presented in this chapter. Secondly, effects on the propagation of the pulse due to the generation of plasma wakefields were dismissed. This effect acts as a perturbation to the plasma term described in eq.

4.6.58 and is proportional to a factor of $\delta n_e/n_e \approx 10^{-5}$ [37] which will thus have only a minor contribution to the propagation. Finally relativistic effects were neglected as they occur at intensities of $2c\epsilon_0 \left(\frac{m_e c\omega_0}{e}\right)^2$, when the electron mass increases significantly. For the central frequency of the whitelight spectrum this intensity is in the order of $10^{19}\, W/cm^2$ which is well beyond the peak intensities reached by transform-limited whitelight pulses studied here ($6.78 \times 10^{14}\, W/cm^2$). These simplifications were necessary to reduce the required computational time for the propagation of the laser pulse. The accuracy of the simulation method was tested by comparison with a different nonlinear pulse propagation implementation [113]. Spatial propagation of the beam without nonlinear effects was verified by the accuracy in recreating the expected Gaussian beam focus. Additionally, values for the plasma density and plasma column diameter were checked to match the order of magnitude stated in [114].

Depending on the laser-wavelength and intensity, different theories should be used to model the underlying ionisation process. While at very high intensities above threshold ionisation (ATI) could become relevant, at lower intensities and low frequencies tunnel ionisation should be assumed. Short wavelengths in contrast suggest multiphoton-ionisation as the dominant process. The widely accepted quantity to distinguish between different ionisation regimes is the Keldysh parameter [99]. It indicates whether the propagation takes place in a regime dominated by tunnel ($\gamma_K < 1/2$) or multiphoton ionisation ($\gamma_K > 1/2$) [41]. For transform-limited pulses at the experimental conditions at hand, the Keldysh parameter is $\gamma_K = 0.65$ with the ionisation energy of Argon ($15.76\, eV$) [115], or $\gamma_K = 0.62$ when the ionisation energy of Krypton ($14\, eV$) [116] is applied. Since these values for the Keldysh parameter are only as low for the peak intensity of a transform-limited pulse and mostly shaped pulses will be studied in the experiments presented, one can safely assume that, except for the propagation of TL-pulses, a reduced model regarding only MPI will be sufficient. The rate at which multiphoton ionisation occurs is equal to

$$W_{mp} = \frac{2\pi\omega_0}{(l-1)!}\left(\frac{I(r,z,\tau)}{I_{mp}}\right)^l, \tag{7.3.2}$$

where $I_{mp} = \hbar\omega^2/\sigma_{mp}$, while $\sigma_{mp} = 6.4 \times 10^{-18}\, cm^2$ is the multiphoton cross section which, for the simulation, was taken from [37]. This can be a highly nonlinear process, where $l = \lfloor U_{ion}/\hbar\omega \rfloor + 1$ equals the number of photons required for ionisation. The laser pulses used in this experiment are mainly so short, that electron-ion recombination and electron attachment processes will be neglected [37]. Using rate equations one can therefore obtain the number of free electrons by integration.

7.3.3 Experimental Results for Argon

Prior to the final setup used for the most part of the experiments, two different pressure chambers were used. One made from acrylic glass allowed to take pictures of the filament [fig. 7.17 b)] while the other had a side window from which side-spectra of the filament could be observed [fig.7.17 a)]. Both chambers employed a spherical focussing mirror with a focal length of $f = 30\, cm$, and PRISM was used to find an offset phase for compensation of the dispersion up to the filament. The filament spectra shows two significant features. Argon I recombination lines dominate the spectrum. In this graph red bars denote persistent Argon I and blue bars persistent Argon II lines. It seems that only single ionisation occurs. Additionally a significant plasma continuum spans from $350\, nm$ to $700\, nm$. The plasma temperature can be cautiously estimated by the maximum of the continuum which yields $5770\, K$. This is in line with results obtained by W.Liu et. al. [117] who measured the plasma temperature during filamentation in Argon to be $5800\, K$ by evaluating

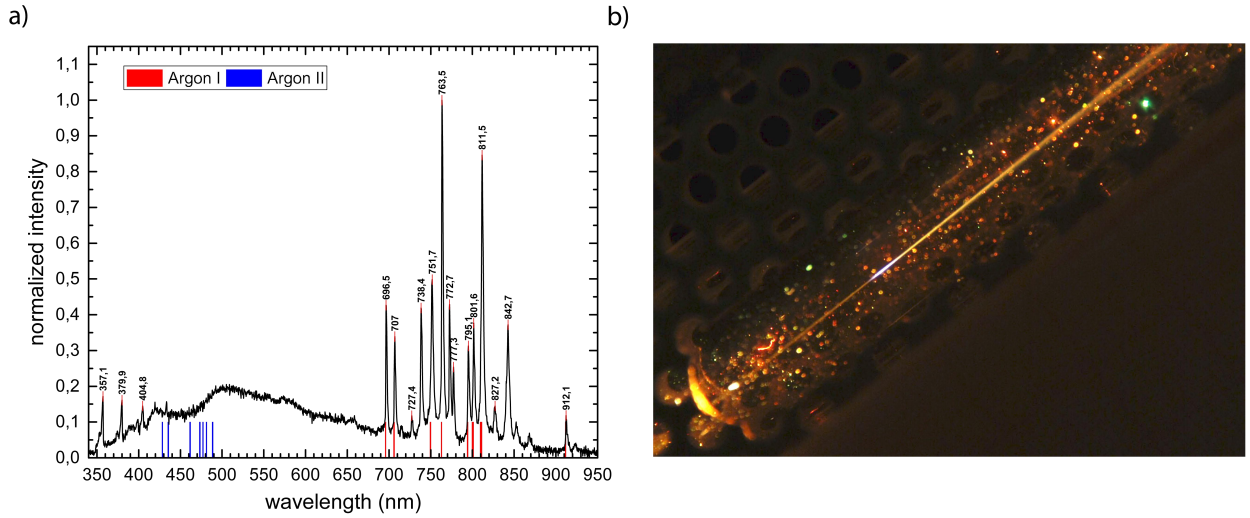

Figure 7.17: a) Side-spectrum of the filament for $9\,bar$ Argon. This spectrum was taken perpendicular to the beam path with an integration time of 2 seconds. The persistent lines of Argon I and Argon II are depicted in the spectrum. While fluorescence due to recombination of Argon I is present, no signs of double ionisation can be found in this spectrum. At these experimental conditions a broad continuum from the plasma can be observed. b) shows a filament created by a transform-limited whitelight laser pulse. The beam is entering from the bottom left. Both images are based on experiments under similar conditions in two different pressure chambers.

fluorescence line-widths. It has to be noted that these results were obtained at significantly different experimental conditions. In the final setup, pulses shaped by the SLM are guided into the chamber with a couple of beam steering mirrors. In the gas filled chamber, which was flushed several times to ensure neither air or Krypton would interfere with experiments, the beam is focussed by an off-axis focussing silver mirror with a focal length of $25\,cm$. The beam power was $50\,mW$, measured just before the chamber. This equates to pulse energies of $50\,\mu J$ and a peak power of $9.4\,GW$. After the chamber, the strongly modulated spectrum is diffused by a Teflon beam-block and then measured via a fibre spectrometer. [Fig. 7.18 (a) (red-dashed)] shows the spectrum obtained after the chamber, filled with $9\,bar$ Argon, for a precompensated pulse. The dashed-red line depicts the input spectrum for reference. Further broadening and a blue-shifting could be observed. Here, an offset phase found using the PRISM algorithm was used to create precompensated pulses with the pulse shaper. Pulses obtained this way should be correctly compensated so that the dispersion of the gas and the optical elements up to the filament are accounted for. When the spatial focus coincides with the temporal focussing of the laser pulse, the maximal peak intensity and ionisation rate is reached at the beginning of the filament, resulting in the largest acoustic shock wave. This signal was detected via a microphone placed as close as possible to the filament's position. In Fig. 7.18 the microphone signal is shown as it was measured with the help of a digital oscilloscope and a microphone amplifier circuit. It can be seen that the acoustic shock repeats itself at a frequency of $1\,kHz$ which coincides with the laser's repetition rate. The amplitude of this oscillation was used as nonlinear feedback for the compensation algorithm. A linear chirp scan [fig. 7.18] confirms that the phase offset indeed compensates the dispersion up to the filament correctly. From [fig. 7.18 c)] one can see that the microphone maximum appears at a small linear chirp of $10\,fs^2$. The algorithm which was used for finding the phase offset strongly modulates the spectral phase and uses a Fourier transform of the nonlinear signal to compute the pulse phase. This means that the spectral phase measurement is based on low intensity pulses which will hence experience a lower level of nonlinear effects than transform-limited pulses found close to zero chirp in Fig. 7.18

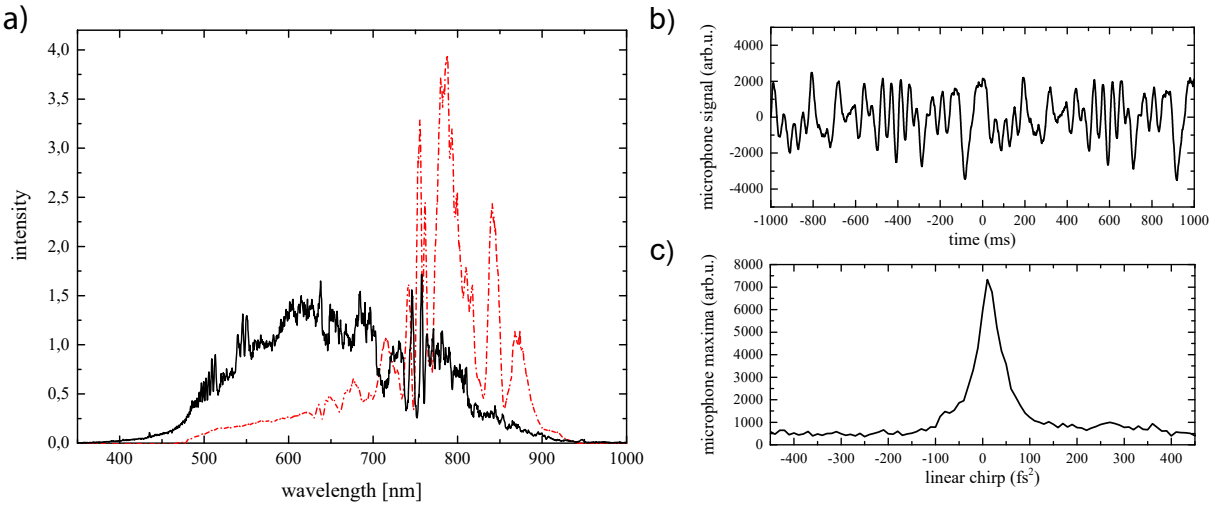

Figure 7.18: a) (red-dashed) Reference spectrum used as initialisation for the simulations. The spectrum was measured directly in front of the chamber filled with $9\,bar$ *Argon for a transform-limited pulse. (black-solid) shows the heavily modified spectrum for the same pulse after transmission through the Argon-filled chamber. b) Microphone signal as it is measured by an oscilloscope for a close to transform-limited pulse. The pattern repeats itself after* $1\,ms$ *which corresponds to the repetition rate of the laser. c) A linear chirp was added in addition to the compensation phase. For each pulse the amplitude of the microphone signal was plotted versus the linear chirp.*

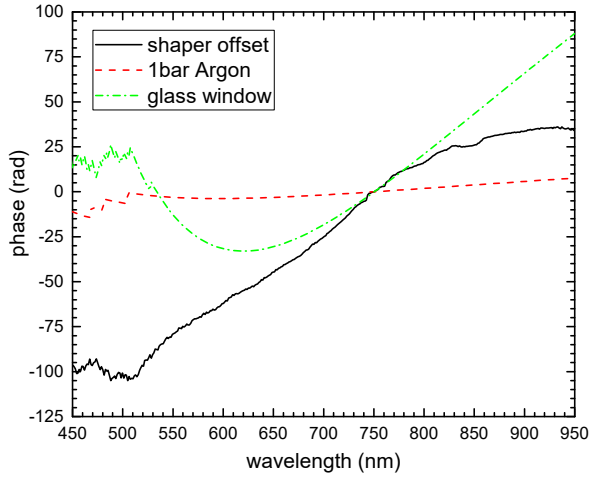

Figure 7.19: Phase offsets were determined at variable pressure and with and without an additional glass window in the beam's path. From the difference of these offsets the phase offsets which corresponds to 1bar of Argon and a single glass window was evaluated. While increasing the pressure in steps of 2bar the increase in compensation was equal for each step which suggests that nonlinearities did not have any influence on the PRISM offset.

(c). it can be concluded that this small shift of the microphone maxima appears to be related to a higher-order nonlinear change in dispersion.

For accurate simulation of linear effects concerning the propagation of pulses in the focal region it was necessary to determine the exact dispersion of the gas inside the chamber. Hence a series of phase optimizations were carried out at low intensities and at various gas pressures. Phase compensations were determined for 3, 7 and 9 bar of Argon pressure. After that a window was added to the beam line to measure the dispersive effect of the chamber-windows. The differences between the phase compensations found for 3 and 7 bar and for 7 and 9 bar were as equal

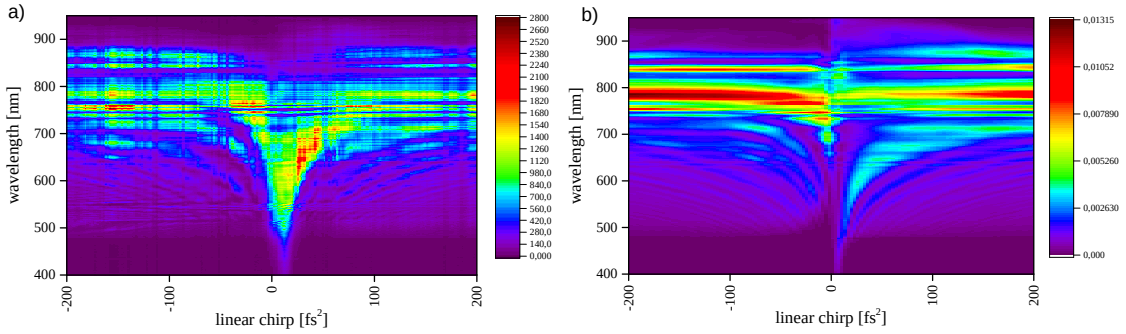

Figure 7.20: a) This figure shows spectra after the chamber (as vertical lines) as a function of the linear pulse-chirp. The dominating feature is the broadening of the spectra close to zero chirp, as well as modulations which occur in the low wavelength range for positive and negative chirps alike. b) shows simulations carried out including dispersion, self-phase-modulation, self-steepening and plasma effects via multiphoton ionisation. Close to zero chirp differences emerge which may arise from the lack of the model of the ionisation process at very high intensities. (see chapter 7.3.2)

as expected since the dispersion should increase linearly with the gase's pressure. The values obtained for the GVD and TOD ($610.5\,fs^2/m$, $326.8\,fs^3/m$) of Argon were later used in addition to the nonlinear refractive index ($n_2 = 1.08 \times 10^{-19}\,cm^2/W$) [105] when performing simulations of the pulse propagation. [Fig. 7.19] shows the phase compensation required up to the chamber (black), for one bar of Argon (dashed-red) and for the entrance glass window (dashed-green). Linear combination of these offsets made it possible to quickly adapt to altered experimental conditions and precompensate pulses accordingly. The first pulse parameters that will be examined are the linear and quadratic chirp. Therefore, spectra were measured while scanning the linear and quadratic chirp (b_2 and b_3) from $-200\,fs^2$ to $200\,fs^2$ and $-400\,fs^3$ to $400\,fs^3$, respectively. The central wavelength for the chirp expansion was chosen to be $761.22\,nm$, which equals the central wavelength of the input spectrum. Here, the central wavelength was defined by:

$$\lambda_0 = 2\pi c/\omega_0 = 2\pi c/\left[\frac{\int_{-\infty}^{\infty}\omega|E(\omega)|d\omega}{\int_{-\infty}^{\infty}|E(\omega)|d\omega}\right]. \tag{7.3.3}$$

[Fig.7.20] summarizes the measured a) and simulated b) spectra for linearly chirped pulses at the pressure of $9\,bar$ Argon. Intensities are shown in colour, linear chirp and wavelength on the x and y axes. Close to $0\,fs^2$ the spectrum experiences strong spectral broadening and a blue shift. Broadening is found to be strongest for lightly positive chirped pulses $\sim 10\,fs^2$ which is when the spatial and temporal focus coincide. The position of maximal spectral broadening may also arise from the earlier spatial focussing which arises from strong self-focussing when the pulse is transform limited. This shift favours pulses which are precompensated for this earlier point which can lead to the results seen in both simulation and measurement [Fig.7.20]. Simulation and experiment seem to differ primarily for close to transform-limited pulses. The reason for this small agreement could be the reduced model used for the ionization process. It seems that the simulation over-predicts absorbance due to multiphoton ionisation for very high pulse-intensities. This is to be expected as for these pulses a mix of multiphoton and tunnel ionization is predicted by the Keldysh parameter. The simulations allowed to verify that all modelled source-terms were responsible for the observed spectral features in the medium to low intensity regime. Therefore, only a combination of self-phase modulation, self-steepening and plasma effects leads to the measured spectra. As an overall trend, the linear chirp scan features a spectral shift to higher energies for

smaller absolute chirp values. Supplementary results that were obtained from the simulations can be found in the appendix [Fig. 1].

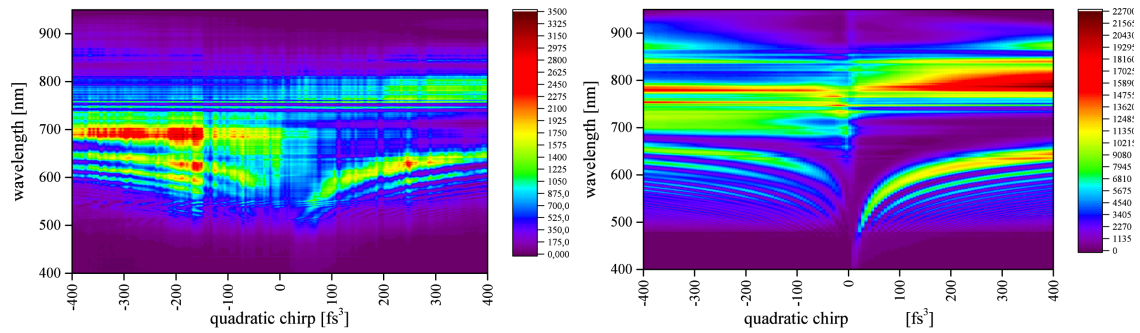

Figure 7.21: (left) shows spectra modulated by nonlinear effects and plasma interaction in the chamber. The x-axis denotes the quadratic chirp value in fs^3 of the pulses at the focus in the chamber. Strong spectral bands emerge which differ for positive and negative chirp values. (right) The simulation recreates the experimental results quite remarkably. An asymmetry between positive and negative chirp values, resulting from the asymmetry in pulse shapes is clearly visible.

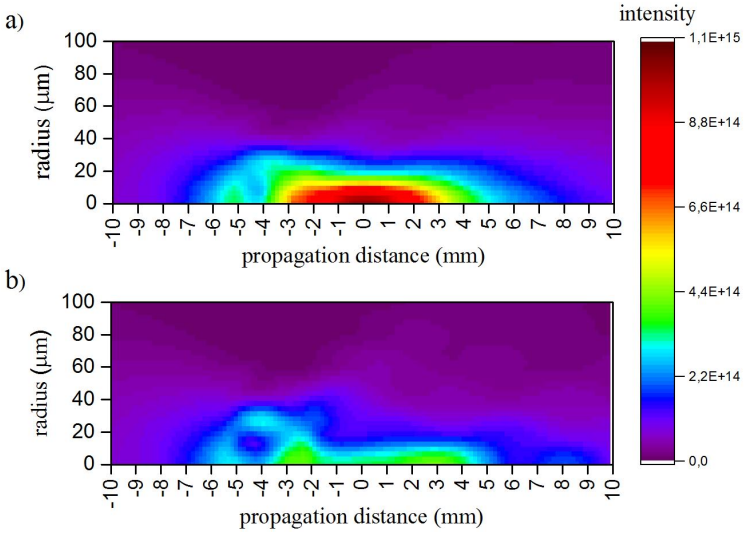

Figure 7.22: Simulated intensity profile of the laser focus for a pulse with quadratic chirp of (a) $-200fs^3$ and (b) $+200fs^3$. The pulses were precompensated to acquire the desired spectral phase at the centre of the simulation window. Both graphs use the same intensity scale. The positively chirped pulse experiences a stronger defocussing early on which results in an overall lower peak intensity.

The agreement between simulation and experiment is better in the case of the quadratic chirp scan which is dominated by two asymmetric spectral bands [Fig. 7.21]. They shift towards higher frequencies for lower absolute chirp values (thus shorter pulses). The differences in the spectra for positively and negatively chirped pulses arise from the temporal asymmetry of the pulses. For pulses with $b_3 > 0\,fs^3$ the laser pulse has a shallow leading and a steep trailing flank while for $b_3 < 0\,fs^3$ the Argon atoms experience a steep rise in electrical field strength followed by a long decline. The slope of intensity determines the frequency shift by self-phase modulation and the plasma interaction, which can be observed in [Fig. 7.21]. Here, in the case of positively chirped pulses, we see a narrow band shifted far towards higher frequencies and a broad spectral band

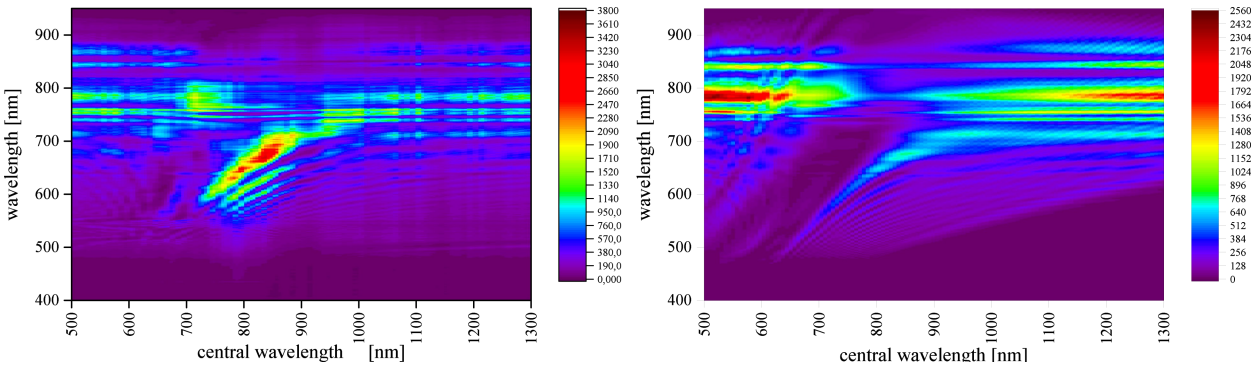

Figure 7.23: Experiment and simulation for wavelength-shifted third-order phase functions ($b_3 = 2 \times 10^2 fs^3$). Here, the x-axis denotes the wavelength around which the phase function is antisymmetric. (left) With a decreasing wavelength of antisymmetry a spectral band shifts accordingly to lower wavelengths. (right) The simulation depicts the same shifting band. Only the width and intensity in relation to the peak around 800nm are not exactly recreated.

shifted to lower frequencies. These effects diminish for higher pulse chirps since SPM and MPI are primarily dependent on the intensity.

[Fig. 7.22] showcases the simulated intensity distribution in the focal region for a positive and a negatively quadratically chirped pulse. As mentioned before, negatively quadratically chirped pulses exhibit a steep leading flank. This means that the bulk of ionisation occurs early on which seems to be able to counteract early self-focussing of the pulse. Simulations show, that negatively quadratically chirped pulses resemble Gaussian beam propagation, while positively chirped pulses are thus more prone to filamentation. It can be seen that in the filamentation regime, ($b_3 \geq 0\, fs^3$) maximal intensities are lower compared to negatively chirped pulses. Additional results obtained for the electron density and intensity profile are summarized in the appendix [Fig. 2]. Besides a shifting spectral band in [Fig. 7.21], a broad dip in the spectrum can be seen for positive quadratic chirps which broadens for pulses with lower quadratic chirp or higher peak intensities. This feature could be used to optimize spectral ratios of filament spectra when those are experimentally desired. In order to see whether these features could be controlled in an easy parametric way, the previously employed parametrization consisting of a quadratic chirp expanded around a selectable frequency ω_c was used.

$$\varphi(\omega) = \frac{b_3}{6}(\omega - \omega_c)^3 \tag{7.3.4}$$

This parametrization is an antisymmetric phase function which was already shown to be applicable to optimize second- and third-order processes around the wavelength of antisymmetry. The observed spectral changes in [Fig. 7.23] can be understood by taking a closer look at the saddle point of the third-order phase function. Around this point of antisymmetry (ω_c) the first derivative of the phase (the instantaneous frequency) $\partial\varphi(t)/\partial t$ becomes zero. This implies that, at the peak of intensity, frequency-components around ω_c are dominant. Frequency shifts generated by the plasma depend on the ionisation rate which in turn depends on the intensity as well as the instantaneous frequency. Therefore, the spectral maxima in the λ_c shift-scans can be seen as being partially moved in correspondence to these antisymmetry points. This explanation is supported by the similarity of the movement of the spectrum's center wavelength to the wavelength of the shifting spectral band. In [Fig. 7.24 a,b] selected spectra from the λ_c-scans are shown. [Fig. 7.24 b,d] depicts the corresponding simulation results. A larger third-order phase (c, d) appears to result in narrower spectral features. And the reduced peak intensity of these pulses invokes a smaller shift of the maxima, when compared to phase-shaped pulses with a $b_3 = 100 \times 10^2 fs^3$. Again simulation

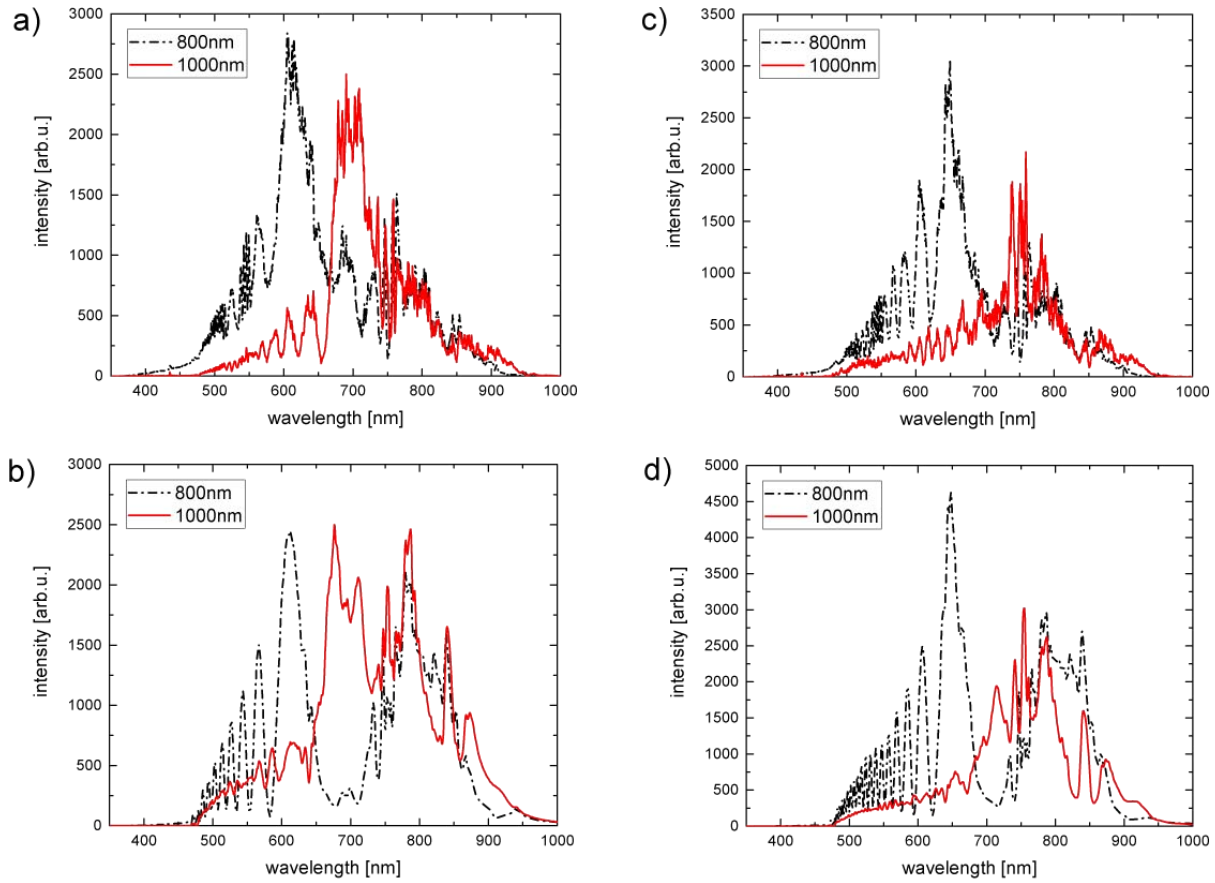

Figure 7.24: Measured spectra and corresponding simulations for selected quadratic chirp values and wavelengths of antisymmetry (see Fig.7.23). a) shows spectra for pulses of $100\,fs^3$ *and a* λ_c *of* $800\,nm$ *and* $1000\,nm$*. The simulation b) confirms the position of the shifted spectral band as well as the modulations seen for very short wavelengths. The graphs in c) are a further example for pulses of* $200\,fs^3$ *chirp. Here, sharper spectral features and shifts to longer wavelengths are visible. d) depicts the simulation for matching experimental conditions.*

and results agree well. Small differences can be observed in the ratio of intensity of the shifting spectral band and the $800\,nm$ peak. This might again be the result of neglecting photo-ionisation other than multiphoton ionisation which could be partially relevant for some pulse-shapes at the onset of the filament, before ionisation leads to energy loss. The spectra in [fig. 7.24 a), b)] show that the position of the maxima is reflected very well by the simulation. It can be seen that a shift of λ_c to lower wavelengths leads to a shift of the modulated peak to lower wavelengths. Pulses with large quadratic chirp possess a smaller rise in intensity on both leading and trailing flank. This yields a smaller shift of the spectral peak for pulses with $200fs^3$ [fig.7.24 c,d)] in comparison to the lower quadratic chirp of $100fs^3$ in [Fig.7.24 a,b] due to self-phase modulation as well as interaction with the plasma. In [Fig. 7.24 c,d)] we can observe that for $\lambda_c = 1000\,nm$ the resulting pulse generates only minor spectral modulations by self-phase modulation or ionisation. This threshold was again verified by the simulation. As a simple method for a controlled spectral modification one could chose the desired spectrum by adjusting the centre wavelength and one can select the spectral width by modifying the prefactor. However, a precise spectral control will require more complex pulse shaping.

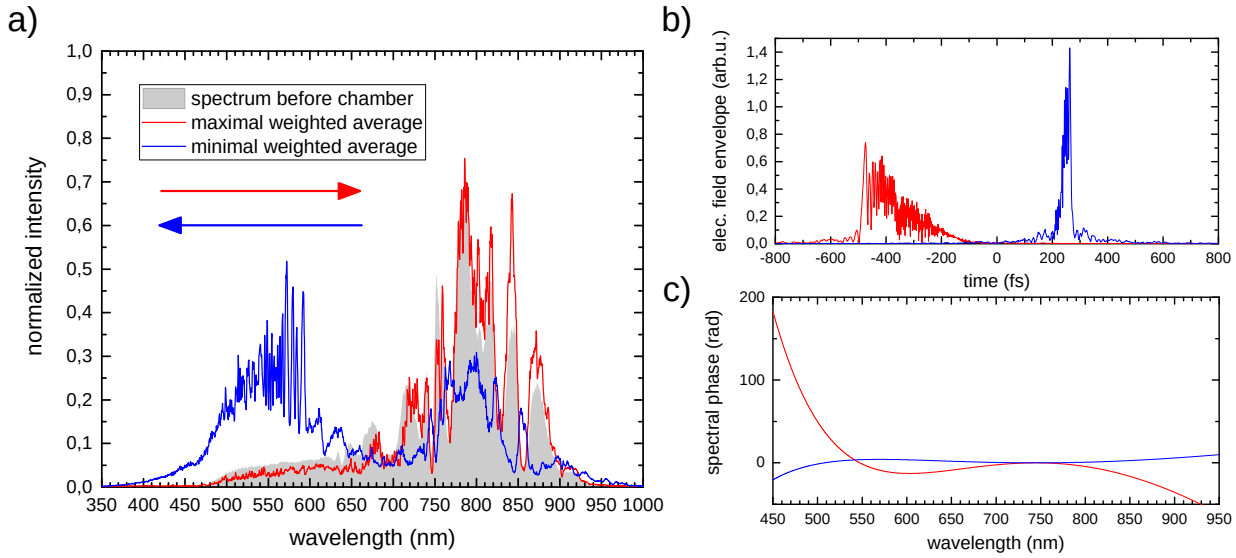

Figure 7.25: Optimization results for spectra with maximal and minimal average wavelength in Krypton. a) shows the spectra found by one of the optimization runs. The shift towards lower wavelengths is significantly larger than the result of the opposing optimization goal. b) depicts the temporal pulse shapes corresponding to both spectra, while c) shows the spectral phase found by the optimization algorithm.

7.3.4 Optimal Pulses for Creating Specific Spectra after Filamentation

After understanding the basic effects of parametric pulse chirps on the filament spectra a genetic algorithm was used to optimize a ratio of two arbitrary spectral bands. The parameter-set consists of a chirp expansion up to the third-order around a central wavelength λ_c. The central wavelength is also subject to optimization and might hint on the underlying optimization method. For optimizations, the genetic optimization, introduced in chapter 6.1 was used. One relevant property of a spectrum after filamentation is the weighted-average central wavelength ($\bar{\lambda}$) as defined in eq. 7.3.3. Optimizations were carried out for Argon and Krypton to find pulses either maximizing or minimizing this objective. It was to expect that a blue shift will be greatest for relatively short pulses and strong ionisation, while a red shift will be more difficult to achieve since SPM cannot by itself lead to an overall shift of the spectrum. The spectra obtained by one of the optimizations

central wavelength	λ_c	b_2	b_3	b_4
min	$1017.6\,nm$	$134.0\,fs^2$	$-146.4\,fs^3$	$37.4\,fs^4$
max	$400.0\,nm$	$383.4\,fs^2$	$-332.2\,fs^3$	$-564.6\,fs^4$

Table 7.4: Optimized parameters found by the evolutionary optimization for spectra with maximal and minimal average photon energy in Krypton.

on this objective for $9\,bar$ Krypton are summarized in [fig. 7.25]. In the leftmost graph it can be observed that pulses minimizing $\bar{\lambda}$ achieve a significant shift of the spectrum after filamentation even which is even greater than that seen for the transform-limited pulse. The optimization on the inverse objective seems to give no real advantage over the input spectrum. A red shift of $\bar{\lambda}$ seems to be impossible via phase shaping, at least in the boundaries of the optimized phase parametrization. As expected, relatively short pulses result in the largest shift of $\bar{\lambda}$ as can be seen in [Fig. 7.25 b)]. Another property of the pulse shapes is that both feature a steep flank, once on the leading and once on the trailing edge which might result from an optimization of the spectral changes due

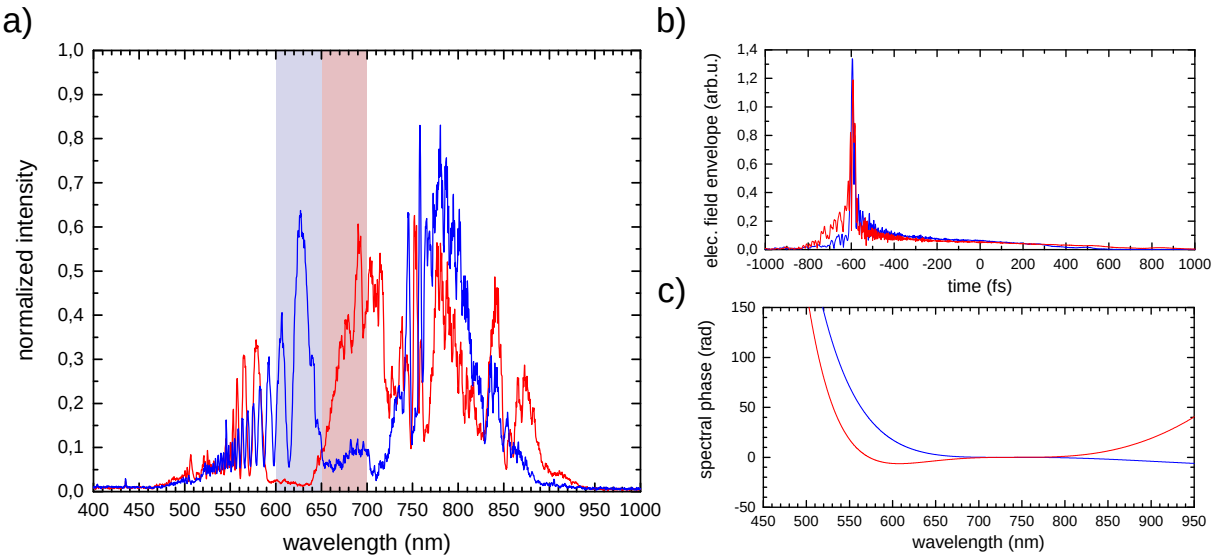

Figure 7.26: Optimization results for spectra with maximized or minimized intensity ratio between two spectral bands in Argon. a) The optimized spectra show that the algorithm found pulse shapes leading to distinct spectral features fulfilling the optimization goal in either direction. (blue) stands for the optimization trying to maximize the intensity in the blue area and minimize all intensity in the red area. (red) on the other hand optimizes the inverse ratio. b) The temporal pulse shapes seem very similar. c) depicts the different spectral phase functions found by the evolutionary algorithm during these optimizations.

to self-phase modulation, since a steep trailing edge (blue) will lead to a large positive frequency shift.

Parameters found by the optimization for a maximization or minimization of $\bar{\lambda}$ are summarized in table 7.4 where one can see that overall smaller chirps were found by the minimization optimization. A corresponding optimization carried out for Argon can be found in the Appendix [fig. 3, tab. 1].

In the previous chapter [fig. 7.24] indicated that quadratically chirped pulses would lead to the formation of a spectral band after filamentation which was controllable via the point of antisymmetry. In order to understand whether phase shaped pulses can be used to create tailored spectra after filamentation optimizations on a special manufactured fitness functions were carried out. For that, the spectral intensity in two wavelength ranges was integrated and divided. Multiple evolutionary optimizations were performed after which the optimization with the largest fitness was selected. Each generation consisted of 30 individuals including one survivor from each previous generation. [Fig. 7.26] shows the result of two optimizations either maximizing or minimizing

$(600-650)\,nm$	$(650-700)\,nm$	λ_c	b_2	b_3	b_4
min	max	$631.9\,nm$	$69.6\,fs^2$	$1152\,fs^3$	$4455\,fs^4$
max	min	$733.0\,nm$	$-2.1\,fs^2$	$386\,fs^3$	$1422\,fs^4$

Table 7.5: Results found by genetic optimization of the spectral areas given above. Both solutions differ strongly. Overall larger chirps are found when maximizing lower wavelengths.

the ratio of the integrated spectra between $600\,nm - 650\,nm$ and $650\,nm - 700\,nm$. When maximizing the spectral band for higher wavelengths the genetic optimization required 27 generations before it converged to an intensity ratio of approximately 11.7. The best optimization for the inverted fitness function found an intensity ratio of 4.1 after 33 generations, which corresponds to

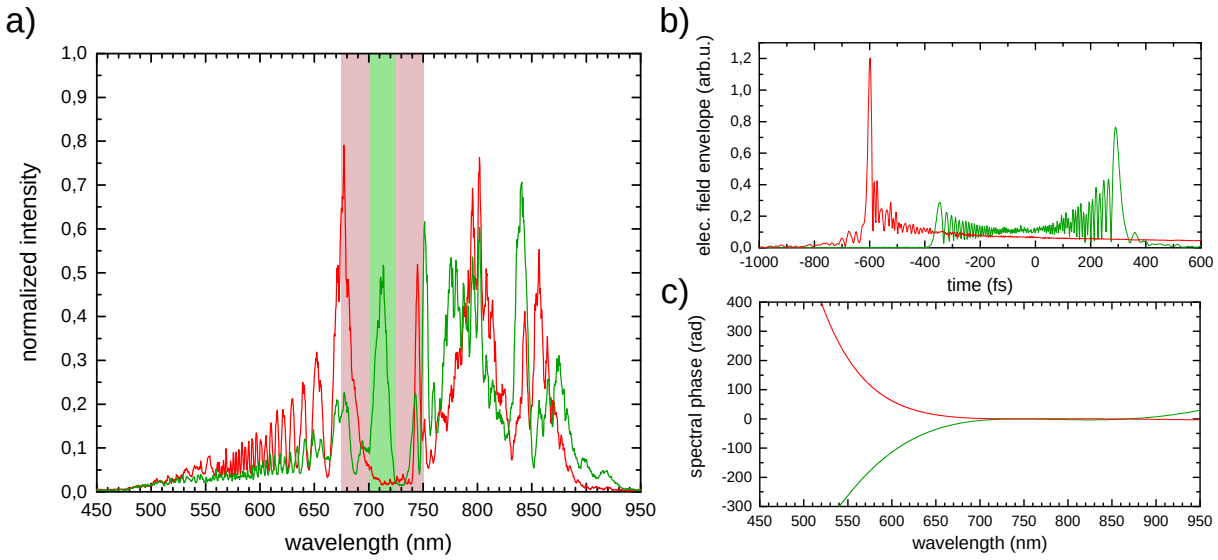

Figure 7.27: Optimization results for optimizations on more complex spectral features after filamentation in Argon. a) The green spectrum optimizes a central band from $700\,nm$ to $725\,nm$ and minimizes the spectral intensity in the red areas. The red spectrum minimizes the signal in the green and maximizes the spectrum in the red spectral areas. b) The corresponding temporal pulse profiles, which were calculated using the phase found by the optimization and the spectrum before the chamber, show features different from previous optimization results.c) depicts the phase functions resulting in the pulses in graph b).

an overall modulation of the ratio by a factor of about 48. From here on, optimizations factors will not be calculated since the choice of fitness function, is somewhat arbitrary. [Fig. 7.26 c)] shows the optimal phase functions (without the offset phase used for compensation) and [Fig. 7.26 b)] the calculated temporal pulse shapes at the onset of the filament which lead to the presented spectra. The spectral features may be explained by the wavelengths of the inflection points of the spectral phase which can be regarded as local antisymmetry points. The (red) phase function for maximizing $650 - 700\,nm$ [Fig. 7.26 c)] shows two inflection points whereas the (blue) phase possesses only one inflection point. This corresponds to spectral maxima as can be seen in [fig. 7.26 a)] which suggests that higher order phase terms will be required for more complex spectral control. Parameters found by these two optimizations are summarized in [tab. 7.5]. In a third optimization an even more complex fitness function was chosen to optimize filament intensity in a central band while minimizing intensity on both adjacent spectral areas. This could be used to increase the efficiency in selective excitation of two-photon versus three-photon processes by means other than the pulse length, hence three spectral areas were selected and the fitness function calculated as the ratio between the central area divided by the integrated spectra of both adjacent bands multiplied by $1/2$. Both, optimizations in Argon and Krypton were performed. In either gas the optimization was able to find pulses creating tailored spectra after filamentation matching the set optimization goals. [Fig.7.27] again combines results for two optimizations in Argon where in graph a) the both resulting spectra are shown. It should be noted that both spectra show a spike followed by a repeating pattern of smaller peaks towards shorter wavelengths. To understand the origin of this feature simulations were carried out for the pulse found by the optimization maximizing and minimizing the spectral band from $700\,nm$ to $725\,nm$ with respect to its surroundings. Using the whitelight spectrum which was measured before the chamber, the simulation recreated the spectra measured after optimization very accurately [see fig. 7.28 a)]. As in both, simulation and measurement the same spectral features emerge, we can try to understand the changes that occur in [Fig.7.27 a)] by analyzing the spectral evolution during the simulation. [Fig. 7.28 b)] shows

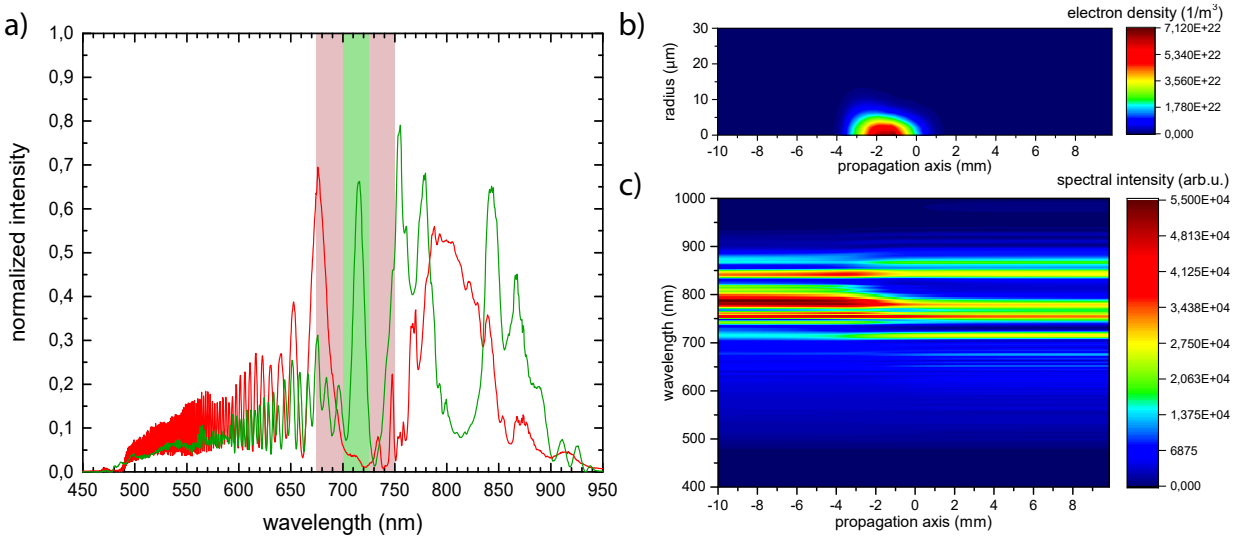

Figure 7.28: Simulations carried out for the optimizations on a central band in 9 bar Argon. a) Spectra resulting from the simulations when the phase found by the optimization is used as the input. The green line corresponds to the phase found maximizing the central band, while the red line depicts the simulation for a shaped pulse minimizing the central spectral area. b) The electron density identifies the area where plasma effects should be dominant. c) The spectrum during the simulation. Here, the x-axis denotes the progress of the simulation.

the simulated electron density and [Fig. 7.28 c)] the spectral evolution for the optimization which maximizes the central band. The localization of the spectral changes to the focus indicates that the spectral modulation is a consequence of the temporal phase induced by the creation of plasma. At these intensities self-phase modulation appears to play only a marginal role. SPM was still critical in this simulation since self-focussing in combination with plasma defocussing determine the peak intensity of the focus. As a test, SPM and self-steepening were disabled after the focus was reached. The simulated spectral change for a single step of the split step Fourier method at the focus confirmed that SPM and self-steepening only play a minor role when compared to the plasma term. Optimizations on this fitness function were carried out in Krypton as well. Results [fig. 7.29] seem similar to those in Argon. Again both simulations find pulses which fulfil the optimization goals. The interplay between all effects relevant for pulse propagation makes it difficult to further interpret pulses found by the evolutionary algorithm. Simulations confirm that only the combination of all processes will result in the spectra shown here. Despite these convoluted interactions it becomes clear that the pulse shape at the focus is the key to control the spectrum after filamentation. When comparing pulses obtained for the optimization in Argon and Krypton one difference stands out. Pulses optimized for a central band in Krypton appear to be longer than those found for Argon. This can be understood when taking the large nonlinear refractive index of Krypton into account. Hence, smaller peak intensities are found when compared to optimization results in Argon. Parameters found in both optimizations are summarized in the appendix [tab. 3]. These non-trivial results show how genetic algorithms can be used in connection with parametric pulse shaping to find optimized pulse shapes that result in a desired spectral shape after filamentation. Pulse shapes have an immense impact on the spectrum obtained from a filament and should therefore be examined more closely in this regard in the future. Pulse shaping and filamentation could become a versatile tool when looking for custom spectral shapes for a variety of applications. By means developed in this chapter ultrashort-whitelight pulses can be created which fit certain experimental requirements such that e.g. one-photon fluorescence at a certain wavelength

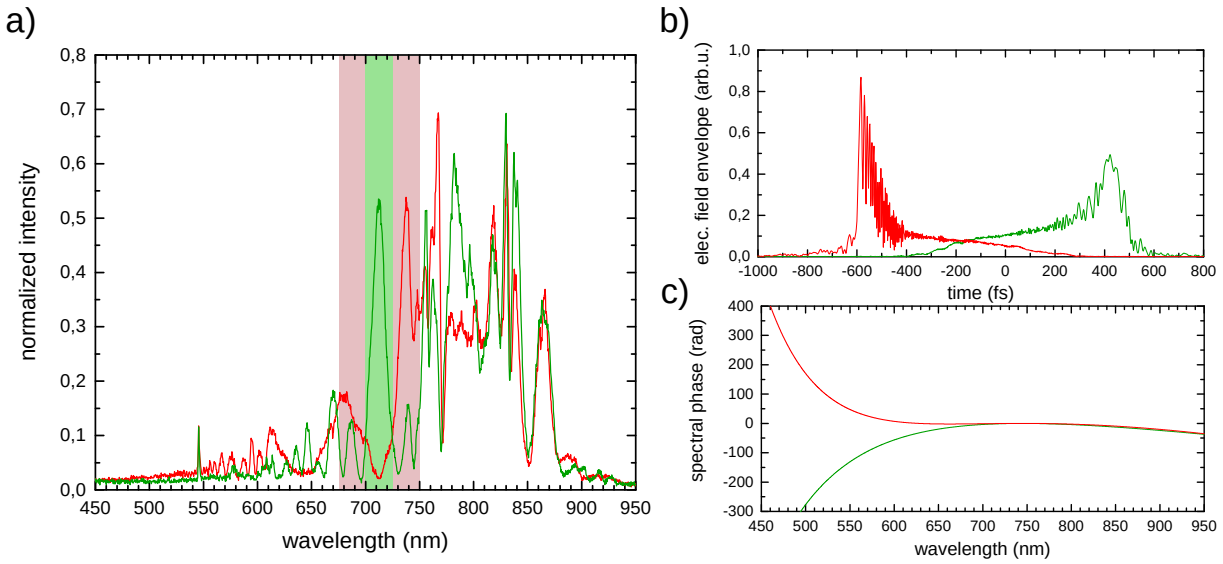

Figure 7.29: Optimization results for a maximized or minimized central spectral band in Krypton. a) The green spectrum is the result of the optimization which favours integrated fluorescence in the green and discourages intensity in the red regions. The red spectrum was again optimized using the inverse fitness function. b) Some differences can be spotted when the temporal pulse shapes found by the optimization are compared to the optimization in Argon. c) Phase functions leading to the temporal pulse shapes shown above.

can be minimized in multiphoton fluorescence experiments by creating tailored spectra which lack intensity at that wavelength.

7.3.5 Influence of Pulse Polarization on Filamentation

A yet unexplored parameter, which has an influence on the characteristics of filamentation is the polarization state of the beam. Polarization can under certain circumstances have an effect on the propagation of a pulse in nonlinear and ionising media. One of the effects could be cross-phase modulation which would account for the changing refractive index of the ordinary beam on the extraordinary beam and vice versa. This effect is mostly relevant in birefringent materials and thus would not occur in filamentation in atomic gases. A second mechanism would be polarization dependent ionisation which would have an influence on the absorption, temporal phase and thus on the spectrum after filamentation. In accordance with theoretical models filamentation is suppressed when the polarization is changed from linear to circular [118]. This is due to the reduced ionisation rate of circular or elliptically polarized light. On the other hand it was found that in certain cases circular polarized light can result in more efficient supercontinuum generation when the pulse energy is above the filamentation threshold [119]. These publications give rise to the assumption that linear polarized light will be more efficient in supercontinuum generation at the experimental conditions at hand. The effects of the polarization state on the filament-spectrum for shaped laser pulses have still to be examined. In a first test it was ensured that a linear polarized beam would result in a linear beam after filamentation by placing a polariser in various orientations after the pressure chamber. This showed that all light measured in forward direction resulted from coherent intra-pulse processes and no delayed fluorescence was detected in propagation direction. Hence no intensity was measured when the polariser was oriented orthogonal to the input polarization. In order to change the polarization state of the beam, the wire-grid polariser, previously used for amplitude modulation, was removed from the beam-line. This enabled the pulse shaper to

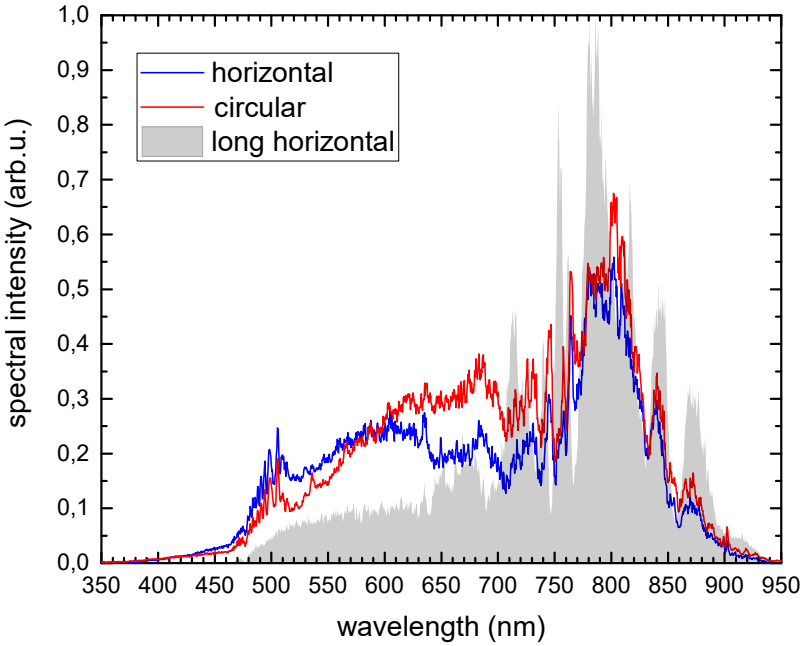

Figure 7.30: Infuence of polarization on the spectrum after filamentation in $9\,bar$ *Argon. The linear polarized beam (blue) results in a larger blue shift of the spectrum when compared with the ciruclar polarized beam (red). A strongly chirped pulse was used to measure a reference spectrum (grey) where no nonlinear effects or ionisations occur.*

select the ellipticity of each spectral component while the orientation of the polarization stayed fixed. The spectrum after filamentation for a transform-limited pulse is shown in [fig. 7.30]. The linear (horizontal) polarized beam results in a larger blue-shift of the spectrum after filamentation. This seems to match results from the mentioned publications that stronger ionisation will occur for linear polarized light. However, both polarizations show strong spectral broadening when compared to the input spectrum. As these results only confirm previous observations, it is time to look at the polarization dependence of filamentation induced by shaped pulses. Therefore a scan of a third-order phase's antisymmetry point was carried out, once with a circular and once with a linear (horizontal) beam polarization. Since peak intensities will clearly be reduced, one has to expect a reduction in the influence of plasma interaction. [Fig 7.31] confirms this assumption by comparing the spectra after filamentation for a third-order phase of $2 \times 10^2 fs^3$ centred at either $750\,nm$ and $800\,nm$. The black spectra represent the measurement for linear and the red spectra for circular polarization. In both graphs, interestingly, no blue-shifting can be observed as it was in the case of the TL pulse. Although, stronger modulations seem to occur for a linear input polarization. In the future, further experiments should be conducted to examine the influence of more complex polarization shaped pulses on filamentation. Recently, it was shown that plasma fluorescence shifts along the propagation axis when the polarization of the beam is changed from linear to circular [120]. And Rostami et. al. reported that elliptical polarized light can enhance supercontinuum generation in molecular gases [121]. Even the birefringence created by filamentation of a first pulse was shown to be influencing the polarization state of a second probe pulse in experiments conducted by Kosareva et. al. [122]. Thus, further studies conducted in this field, especially when applying polarization shaped laser pulses will contribute to the current understanding of polarization dependence of filamentation.

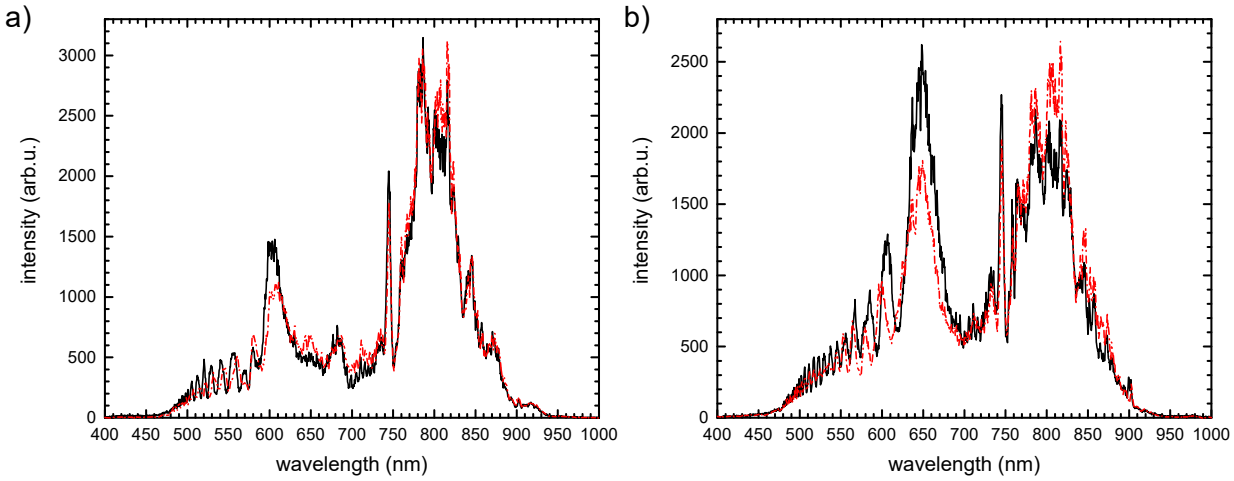

Figure 7.31: Influence of polarization on filamentation of phase shaped pulses.A third-order phase's ($2 \times 10^2\, fs^3$) antisymmetry point was shifted by wavelength. a) $\lambda_c = 750\,nm$ b) $\lambda_c = 800\,nm$. The black spectra correspond to a horizontal and the dashed-red spectra to a circular polarized beam.

7.3.6 Conclusion

In this chapter a model for the filamentation process was created and tested which included linear and nonlinear effects as well as multiphoton ionisation and plasma interactions. A cylindrical two-dimensional parametrization was selected as multiple filamentation will not occur at the beam power available to this laser system. Experiments and Simulation were very close, indicating that multiphoton ionisation is indeed the underlying ionisation process in this intensity regime. Using the simulation it was possible to further understand whether nonlinearities or plasma interaction lead to some of the spectral features observed for shaped pulse filamentation. PRISM was, for the first time, used in combination to a microphone signal to create precompensated pulses for filamentation at the focus position. This method of using the acoustic shock-wave for measuring the phase of a pulse at the start of filamentation could be used to enhance a multitude of applications. Conducted experiments showed that pulse shapes have a strong influence on the focus, the filament and thus the spectrum after filamentation. While self-phase modulation is a part in this process, it seems to mainly act as a focussing mechanism. Spectral changes (even at high pressures) seem to predominantly arise from plasma effects. These plasma interactions can be exploited to generate a spectral band after filamentation which shift parallel to a spectral phase's point of antisymmetry. This allowed for the control of certain spectral features after filamentation. Genetic optimizations were used to fine-tune phase parameters of a Taylor expansion up to the fourth order to match complex optimization goals. Finally, an introduction into the influence of polarization on the filamentation process was given which points towards a wide field of further studies that could be carried out using complex polarization shaped pulse sequences to assess their influence on filamentation.

Outlook 8

Methods, as well as the insight generated by this thesis can aid the development of multiphoton microscopes as they are used for biological or medical imaging. Pulse shaping systems become evermore accessible and will soon find their way into new applications. Although a thorough understanding of the mechanisms of pulse shaping was required up to now, parametric phase functions or pulse shapes can be implemented into pulse shaping systems to allow for easy control of relevant pulse parameters. Thereby, selective excitation of two-photon or three-photon transitions could be achieved by adding an easy to use pulse shaping device to existing microscopes. As the cooperation with the group of Prof. Karsten Heyne showed, the focus in a microscope can be even more optimized when a two-dimensional beam shaper is applied in addition to the temporal pulse shaping technique. Here, the combination of temporal pulse shaping with the ability to influence the spatial focus of one polarization of the beam could open up new measurement schemes. Temporal pulse shaping in STED microscopy can enhance the resolution and efficiency of this technique even more. Z-scans performed with optimized pulses for Tryptophan fluorescence could lead to 3-dimensional maps of the concentration of this amino acid in a biological sample. Another area where results of this thesis might be useful are endoscopic fluorescence experiments or photodynamic therapy. There is great potential for hollow-core photonic fibres being used in high intensity endoscopic applications which could enable the detection of certain fluorescence markers after a fibre, as well as induce photo-damage in the scope of a medical procedure. A combination of detection and phototoxicity by using small gold nanoparticles could even allow for spatially selective damage to pathological tissue. As endoscopes are used in conditions different from an optical table it is essential that the fibre's dispersion and nonlinearities are compensated for, even if the fibre is bent or twisted. Work published prior to this thesis by our group demonstrated how this can be achieved by using a back-reflected part of the pulse to measure changes in the fibres dispersion or birefringence in real-time. Experiments conducted during this thesis show that multiphoton fluorescence can be modelled so well that the influence of pulse shapes can be easily assessed prior to implementation which could help push advancements in this field.

Besides exploring further applications of shaped laser pulses in the area of medicine and microscopy, the opportunities of polarization-shaped laser pulses should be considered for supercontinuum generation by filamentation. Experiments confirmed the influence of polarization states on the ionisation efficiency during filamentation. Thus, a combined optimization, in which polarization states are optimized in addition to phase parameters could be used to exert even greater control of the supercontinuum obtained after filamentation. It was suggested [119] that some polarization effects on ionisation inverse when intensities increase beyond a certain threshold. It could be examined whether less efficient propagation is to blame for this effect or other mechanism are at play resulting in a reduced ionisation efficiency at these intensities. Furthermore, polarization, phase and amplitude shaping can be easily employed to create perpendicular polarized pulse sequences with variable delay. This is an opportunity to observe the filamentation process in extremely short timescales by using a first pulse as a pump and a second perpendicular polarized pulse as a probe pulse. Since both pulses are generated collinear, this method of pulse shaping is an ideal tool to study filamentation dynamics on timescales as short as $\sim 10\,fs$. Plasma generation, as well as cross-phase modulation would pose as the mechanisms connecting the propagation of both perpendicular polarized pulses and could shed more light on the intriguing process of filamentation as a whole.

Scientific Cooperations 9

During this thesis two cooperations led to important exchange of ideas and allowed me to be part in two very interesting studies.

9.1 Setup for Simultaneous Spatial and Temporal Pulse Shaping

While it was shown that phase, amplitude and polarization pulse shaping are valuable tools to improve applications where either adaptive dispersion control or special pulse shapes are required, it can only influence the temporal profile of a pulse. Especially optical systems used in modern multiphoton microscopes could be improved by additional spatial beam shaping. Spatial beam shaping is achieved via a reflective two-dimensional liquid crystal modulator which operates comparable to the SLM's used in this thesis. By influencing the phase along the beam's two dimensional profile, the focus after a lens can be controlled. This is due to the lens acting as a Fourier transform when operated in a 2-f scheme. Experiments conducted by the group of Prof. Dr. Karsten Heyne are set to answer whether a combination of both spatial and temporal pulse shaping can lead to improved fluorescence or even new experimental measurement schemes. My contribution to these experiments was to help set up the temporal pulse shaper and provide a basis for the software to spatially and temporally precompensate pulses for optimal fluorescence when used in combination with a two-photon microscope. These experiments will lead the way to improved multiphoton microscopes that will feature greater resolution as well as the ability to use phase shaped pulses for selective excitation as discussed in in chapter 7.1.

9.2 Kramers-Henneberger States

During a cooperation with the group of Prof. Jean-Pierre Wolf's Biophotonics Group at the Université de Genève, loosely bound states of neutral atoms which only exist during the influence of an oscillating electrical field of high intensity were investigated. These proposed Kramers-Henneberger states [123] could exist during filamentation when certain experimental conditions are met. Trapezoid shaped laser pulses were created with the help of the whitelight laser system featured in this thesis and a Fourier-transform iteration algorithm. These pulses which have a flat-top temporal intensity profile are used to observe resonances of these Kramers-Henneberger states in the laserspectrum after filamentation. Results from this experimental campaign are still under review. A publication featuring additional simulations performed by the group of Prof. Misha Ivanov at the MBI Berlin is in preparation.

Bibliography

[1] D. J. Tannor and S. A. Rice, "Control of selectivity of chemical reaction via control of wave packet evolution," *The Journal of chemical physics*, vol. 83, no. 10, pp. 5013–5018, 1985.

[2] P. Brumer and M. Shapiro, "Control of unimolecular reactions using coherent light," *Chemical physics letters*, vol. 126, no. 6, pp. 541–546, 1986.

[3] A. M. Weiner, J. P. Heritage, and E. Kirschner, "High-resolution femtosecond pulse shaping," *JOSA B*, vol. 5, no. 8, pp. 1563–1572, 1988.

[4] A. M. Weiner, D. E. Leaird, J. S. Patel, and J. R. Wullert, "Programmable femtosecond pulse shaping by use of a multielement liquid-crystal phase modulator," *Optics letters*, vol. 15, no. 6, pp. 326–328, 1990.

[5] R. S. Judson and H. Rabitz, "Teaching lasers to control molecules," *Physical Review Letters*, vol. 68, no. 10, p. 1500, 1992.

[6] A. Assion, T. Baumert, M. Bergt, T. Brixner, B. Kiefer, V. Seyfried, M. Strehle, and G. Gerber, "Control of chemical reactions by feedback-optimized phase-shaped femtosecond laser pulses," *Science*, vol. 282, no. 5390, pp. 919–922, 1998.

[7] A. Lindinger, C. Lupulescu, M. Plewicki, F. Vetter, A. Merli, S. M. Weber, and L. Wöste, "Isotope selective ionization by optimal control using shaped femtosecond laser pulses," *Physical review letters*, vol. 93, no. 3, p. 033001, 2004.

[8] D. Meshulach and Y. Silberberg, "Coherent quantum control of multiphoton transitions by shaped ultrashort optical pulses," *Phys. Rev. A*, vol. 60, no. 2, pp. 1287–1292, 1999.

[9] M. Durand, A. Houard, B. Prade, A. Mysyrowicz, A. Durécu, B. Moreau, D. Fleury, O. Vasseur, H. Borchert, K. Diener, *et al.*, "Kilometer range filamentation," *Optics express*, vol. 21, no. 22, pp. 26836–26845, 2013.

[10] J.-C. Diels and W. Rudolph, *Ultrashort laser pulse phenomena*. Academic press, 2006.

[11] R. C. Jones, "A new calculus for the treatment of optical systems i. description and discussion of the calculus," *JOSA*, vol. 31, no. 7, pp. 488–493, 1941.

[12] P. F. Moulton, "Spectroscopic and laser characteristics of ti:al2o3," *JOSA B*, vol. 3, no. 1, pp. 125–133, 1986.

[13] A. Patas, "Pulsformung für multiphotonische prozesse nach optischen fasern," diplomarbeit, Fachbereich Physik - Freie Universität Berlin, 2011.

[14] D. Strickland and G. Mourou, "Compression of amplified chirped optical pulses," *Optics communications*, vol. 56, no. 3, pp. 219–221, 1985.

[15] C. Rulliere *et al.*, *Femtosecond laser pulses*. Springer, 2005.

[16] W. S. Warren, H. Rabitz, and M. Dahleh, "Coherent control of quantum dynamics: the dream is alive," *Science*, vol. 259, no. 5101, pp. 1581–1589, 1993.

[17] P. Tournois, "Acousto-optic programmable dispersive filter for adaptive compensation of group delay time dispersion in laser systems," *Optics communications*, vol. 140, no. 4, pp. 245–249, 1997.

[18] M. Hacker, G. Stobrawa, R. Sauerbrey, T. Buckup, M. Motzkus, M. Wildenhain, and A. Gehner, "Micromirror slm for femtosecond pulse shaping in the ultraviolet," *Applied Physics B*, vol. 76, no. 6, pp. 711–714, 2003.

[19] S. M. Weber, F. Weise, M. Plewicki, and A. Lindinger, "Interferometric generation of parametrically shaped polarization pulses," *Applied optics*, vol. 46, no. 23, pp. 5987–5990, 2007.

[20] F. Weise and A. Lindinger, "Full control over the electric field using four liquid crystal arrays," *Optics letters*, vol. 34, no. 8, pp. 1258–1260, 2009.

[21] F. Weise and A. Lindinger, "Full parametric pulse shaping in phase, amplitude, and polarization using an effective four-array modulator," *Applied Physics B*, vol. 101, no. 1-2, pp. 79–91, 2010.

[22] F. Weise, *Parametric polarization pulse shaping methods and control of excitation dynamics in ultracold rubidium*. PhD thesis, FB Physik, Freie universität Berlin, 2010.

[23] T. Brixner, G. Krampert, T. Pfeifer, R. Selle, G. Gerber, M. Wollenhaupt, O. Graefe, C. Horn, D. Liese, and T. Baumert, "Quantum control by ultrafast polarization shaping," *Physical review letters*, vol. 92, no. 20, p. 208301, 2004.

[24] M. Plewicki, S. Weber, F. Weise, and A. Lindinger, "Independent control over the amplitude, phase, and polarization of femtosecond pulses," *Applied Physics B*, vol. 86, no. 2, pp. 259–263, 2007.

[25] T. Brixner and G. Gerber, "Femtosecond polarization pulse shaping," *Optics letters*, vol. 26, no. 8, pp. 557–559, 2001.

[26] S. Weber, A. Lindinger, F. Vetter, M. Plewicki, A. Merli, and L. Wöste, "Application of parametric time and frequency domain shaping," *The European Physical Journal D-Atomic, Molecular, Optical and Plasma Physics*, vol. 33, no. 1, pp. 39–42, 2005.

[27] M. Hacker, G. Stobrawa, and T. Feurer, "Iterative fourier transform algorithm for phase-only pulse shaping," *Optics Express*, vol. 9, no. 4, pp. 191–199, 2001.

[28] G. P. Agrawal, *Nonlinear Fiber Optics*. Academic Press, 2007.

[29] I. P. Kaminow, "Polarization in optical fibers," *IEEE Journal of Quantum Electronics*, vol. 17, pp. 15–22, 1981.

[30] C.-L. Chen, "Birefringence in single-mode fibers," *Foundations for Guided-Wave Optics*, pp. 275–308, 2007.

[31] X. Chen, M.-J. Li, N. Venkataraman, M. Gallagher, W. Wood, A. Crowley, J. Carberry, L. Zenteno, and K. Koch, "Highly birefringent hollow-core photonic bandgap fiber," *Optics Express*, vol. 12, no. 16, pp. 3888–3893, 2004.

[32] Y.-R. Shen, *Principles of nonlinear optics*. Wiley-Interscience, New York, NY, USA, 1984.

[33] R. W. Boyd, *Nonlinear Optics*. Academic Press, Jan. 2003.

[34] W. Kaiser and C. Garrett, "Two-photon excitation in ca f 2: Eu 2+," *Physical review letters*, vol. 7, no. 6, p. 229, 1961.

[35] W. Denk, J. H. Strickler, and W. W. Webb, "Two-photon laser scanning fluorescence microscopy," *Science*, vol. 248, pp. 73–76, Apr. 1990.

[36] M. Göppert-Mayer, "Über elementarakte mit zwei quantensprüngen," *Annalen der Physik*, vol. 401, no. 3, pp. 273–294, 1931.

[37] P. Sprangle, J. R. Peñano, and B. Hafizi, "Propagation of intense short laser pulses in the atmosphere," *Phys. Rev. E*, vol. 66, p. 046418, Oct. 2002.

[38] C. G. Morgan, "Laser-induced breakdown of gases," *Reports on Progress in Physics*, vol. 38, no. 5, p. 621, 1975.

[39] P. Gibbon, *Short pulse laser interactions with matter*. World Scientific Publishing Company, 2004.

[40] L. Keldysh, "Ionization in the field of a strong electromagnetic wave," *Zh. Eksperim. i Teor. Fiz.*, vol. 47, 1964.

[41] S. Chin, "From multiphoton to tunnel ionization," *Advances in Multiphoton Processes and Spectroscopy*, vol. 16, p. 249, 2004.

[42] T. Imran, G. Figueira, and D. Dumitras, "Efficient white-light continuum generation in transparent solid media using 250 fs, 1053 nm laser pulses," in *Aip Conference Proceedings*, vol. 1228, p. 370, 2010.

[43] C. Jarman, D. Schumacher, C. Modoran, N. Harmon, and Z. Yoscovits, "Supercontinuum generation in sapphire: A measurement of intensity," *REU Programm, The Ohio State University*, 2005.

[44] B. Mielnik and J. Plebański, "Combinatorial approach to baker-campbell-hausdorff exponents," in *Annales de l'IHP Physique théorique*, vol. 12, pp. 215–254, 1970.

[45] E. Hecht, *Optik*. McGraw-Hill, 1987.

[46] R. Cregan, B. Mangan, J. Knight, T. Birks, P. S. J. Russell, P. Roberts, and D. Allan, "Single-mode photonic band gap guidance of light in air," *science*, vol. 285, no. 5433, pp. 1537–1539, 1999.

[47] T. Birks, P. Roberts, P. S. J. Russell, D. Atkin, and T. Shepherd, "Full 2-d photonic bandgaps in silica/air structures," *Electronics letters*, vol. 31, no. 22, pp. 1941–1942, 1995.

[48] O. Heckl, C. Baer, C. Kränkel, S. Marchese, F. Schapper, M. Holler, T. Südmeyer, J. Robinson, J. Tisch, F. Couny, *et al.*, "High harmonic generation in a gas-filled hollow-core photonic crystal fiber," *Applied Physics B*, vol. 97, no. 2, pp. 369–373, 2009.

[49] P. Ghenuche, S. Rammler, N. Y. Joly, M. Scharrer, M. Frosz, J. Wenger, P. S. J. Russell, and H. Rigneault, "Kagome hollow-core photonic crystal fiber probe for raman spectroscopy," *Optics letters*, vol. 37, no. 21, pp. 4371–4373, 2012.

[50] F. Benabid, J. C. Knight, G. Antonopoulos, and P. S. J. Russell, "Stimulated raman scattering in hydrogen-filled hollow-core photonic crystal fiber," *Science*, vol. 298, no. 5592, pp. 399–402, 2002.

[51] P. S. J. Russell, P. Hölzer, W. Chang, A. Abdolvand, and J. Travers, "Hollow-core photonic crystal fibres for gas-based nonlinear optics," *Nat. Photonics*, vol. 8, no. 4, pp. 278–286, 2014.

[52] M. Eigen, *Ingo Rechenberg Evolutionsstrategie Optimierung technischer Systeme nach Prinzipien der biologishen Evolution*. mit einem Nachwort von Manfred Eigen, Friedrich Frommann Verlag, Struttgart-Bad Cannstatt, 1973.

[53] Coherent, "RegA9000/9050 Datasheet." `http://www.coherent.com/downloads/RegA_9000_9500_DS.pdf`. [Online; accessed 23.08.2016].

[54] Blaze Photonics, *Datenblatt zur Faser HC-800-01*.

[55] GLOphotonics, "PMC-PL-780-USP datasheet,."

[56] V. V. Lozovoy, I. Pastirk, and M. Dantus, "Multiphoton intrapulse interference. iv. ultrashort laser pulse spectral phase characterization and compensation," *Optics letters*, vol. 29, no. 7, pp. 775–777, 2004.

[57] M. Li, J. P. Nibarger, C. Guo, and G. N. Gibson, "Dispersion-free transient-grating frequency-resolved optical gating," *Applied optics*, vol. 38, no. 24, pp. 5250–5253, 1999.

[58] B. E. Schmidt, W. Unrau, A. Mirabal, S. Li, M. Krenz, L. Wöste, and T. Siebert, "Poor man's source for sub 7 fs: a simple route to ultrashort laser pulses and their full characterization," *Optics express*, vol. 16, no. 23, pp. 18910–18921, 2008.

[59] PubChem, "2D structure deposited in or computed by PubChem." `https://pubchem.ncbi.nlm.nih.gov`. [Online; accessed 22.08.2016].

[60] "PhotochemCAD Online Database." `http://omlc.org/spectra/PhotochemCAD/index.html`. [Online; accessed 22.08.2016].

[61] C. Xu and W. W. Webb, "Measurement of two-photon excitation cross sections of molecular fluorophores with data from 690 to 1050 nm,"

[62] R. S. Moog, D. D. Kim, J. J. Oberle, and S. G. Ostrowski, "Solvent effects on electronic transitions of highly dipolar dyes: a comparison of three approaches," *The Journal of Physical Chemistry A*, vol. 108, no. 42, pp. 9294–9301, 2004.

[63] F. P. Hagemann, *Supercontinuum Pulse Shaping for the Optimal Control of Photo-Induced Processes*. PhD thesis, Freie Universität Berlin, 2016.

[64] T.-w. Wu, J. Tang, B. Hajj, and M. Cui, "Phase resolved interferometric spectral modulation (PRISM) for ultrafast pulse measurement and compression," *Optics Express*, vol. 19, p. 12961, July 2011.

[65] B. J. Pearson, J. L. White, T. C. Weinacht, and P. H. Bucksbaum, "Coherent control using adaptive learning algorithms," *Phys. Rev. A*, vol. 63, p. 063412, May 2001.

[66] M. Molga and C. Smutnicki, "Test functions for optimization needs,"

[67] A. Patas, G. Achazi, N. Hermes, M. Pawłowska, and A. Lindinger, "Contrast optimization of two-photon processes after a microstructured hollow-core fiber demonstrated for dye molecules," *Appl. Phys. B*, vol. 112, pp. 579–586, Apr. 2013.

[68] J. Otto, A. Patas, J. Althoff, and A. Lindinger, "Fluorescence anisotropy excitation by polarization-shaped laser pulses after transmission through a kagome fiber," *Applied Physics B*, vol. 122, no. 8, pp. 1–7, 2016.

[69] R. Heintzmann and G. Ficz, "Breaking the resolution limit in light microscopy," *Briefings in Functional Genomics and Proteomics*, vol. 5, pp. 289–301, Dec. 2006.

[70] F. Helmchen and W. Denk, "Deep tissue two-photon microscopy," *Nature Methods*, vol. 2, pp. 932–940, Dec. 2005.

[71] D. Kobat, N. G. Horton, and C. Xu, "In vivo two-photon microscopy to 1.6-mm depth in mouse cortex," *J. Biomed. Opt*, vol. 16, no. 10, pp. 106014–106014–4, 2011.

[72] R. S. Pillai, C. Boudoux, G. Labroille, N. Olivier, I. Veilleux, E. Farge, M. Joffre, and E. Beaurepaire, "Multiplexed two-photon microscopy ofdynamic biological samples with shapedbroadband pulses," *Opt. Express*, vol. 17, pp. 12741–12752, July 2009.

[73] J. M. Dela Cruz, V. V. Lozovoy, and M. Dantus, "Coherent control improves biomedical imaging with ultrashort shaped pulses," *Journal of Photochemistry and Photobiology A: Chemistry*, vol. 180, pp. 307–313, June 2006.

[74] J. P. Ogilvie, D. Debarre, X. Solinas, J.-L. Martin, E. Beaurepaire, and M. Joffre, "Use of coherent control for selective two-photon fluorescence microscopy in live organisms," *Opt. Express*, vol. 14, pp. 759–766, Jan. 2006.

[75] I. Pastirk, J. Dela Cruz, K. Walowicz, V. Lozovoy, and M. Dantus, "Selective two-photon microscopy with shaped femtosecond pulses," *Opt. Express*, vol. 11, pp. 1695–1701, July 2003.

[76] M. Pawłowska, A. Patas, G. Achazi, and A. Lindinger, "Parametrically shaped femtosecond pulses in the nonlinear regime obtained by reverse propagation in an optical fiber," *Optics Letters*, vol. 37, p. 2709, July 2012.

[77] G. Achazi, A. Patas, F. Weise, M. Pawłowska, and A. Lindinger, "Reconstruction of polarization-shaped laser pulses after a hollow-core fiber using backreflection," *Appl. Opt.*, vol. 50, pp. 915–923, Feb. 2011.

[78] K. Deb, "Multi-objective Genetic Algorithms: Problem Difficulties and Construction of Test Problems," *Evolutionary Computation*, vol. 7, pp. 205–230, Sept. 1999.

[79] C. M. Fonseca and P. J. Fleming, "An Overview of Evolutionary Algorithms in Multiobjective Optimization," *Evolutionary Computation*, vol. 3, pp. 1–16, Mar. 1995.

[80] Y. Barad, H. Eisenberg, M. Horowitz, and Y. Silberberg, "Nonlinear scanning laser microscopy by third harmonic generation," *Applied Physics Letters*, vol. 70, no. 8, pp. 922–924, 1997.

[81] N. G. Horton, K. Wang, D. Kobat, C. G. Clark, F. W. Wise, C. B. Schaffer, and C. Xu, "In vivo three-photon microscopy of subcortical structures within an intact mouse brain," *Nat Photon*, vol. 7, pp. 205–209, Mar. 2013.

[82] C. Xu, W. Zipfel, J. B. Shear, R. M. Williams, and W. W. Webb, "Multiphoton fluorescence excitation: new spectral windows for biological nonlinear microscopy," *PNAS*, vol. 93, pp. 10763–10768, Oct. 1996.

[83] S. Schenkl, F. v. Mourik, N. Friedman, M. Sheves, R. Schlesinger, S. Haacke, and M. Chergui, "Insights into excited-state and isomerization dynamics of bacteriorhodopsin from ultrafast transient UV absorption," *PNAS*, vol. 103, pp. 4101–4106, Mar. 2006.

[84] D. Sharma, J. Léonard, and S. Haacke, "Ultrafast excited-state dynamics of tryptophan in water observed by transient absorption spectroscopy," *Chemical Physics Letters*, vol. 489, pp. 99–102, Apr. 2010.

[85] J. Chen, H. Kawano, Y. Nabekawa, H. Mizuno, A. Miyawaki, T. Tanabe, F. Kannari, and K. Midorikawa, "Selective excitation between two-photon and three-photon fluorescence with engineered cost functions," *Optics Express*, vol. 12, no. 15, p. 3408, 2004.

[86] A. Patas, G. Achazi, C. Winta, and A. Lindinger, "Influence of nonlinear effects on the three-photon excitation of L-Tryptophan in water using phase-shaped pulses," *Journal of the Optical Society of America B*, vol. 31, p. 2208, Sept. 2014.

[87] Volume Precision Glass, Inc., "Schott Filter Glass." `http://www.vpglass.com/filter_glass.php`. [Online; accessed 14.09.2016].

[88] Newport AG, "The Effect of Dispersion on Ultrashort Pulses." `http://www.newport.com/the-e%20ect-of-dispersion-on-%20ultrashort-pulses/602091/1033/content.aspx`. [Online; accessed 26.04.2016].

[89] A. Couairon, L. Sudrie, M. Franco, B. Prade, and A. Mysyrowicz, "Filamentation and damage in fused silica induced by tightly focused femtosecond laser pulses," *Phys. Rev. B*, vol. 71, p. 125435, Mar. 2005.

[90] P. Devi, V. V. Lozovoy, and M. Dantus, "Measurement of group velocity dispersion of solvents using 2-cycle femtosecond pulses: Experiment and theory," *AIP Advances*, vol. 1, p. 032166, Sept. 2011.

[91] Z. W. Wilkes, S. Varma, Y.-H. Chen, H. M. Milchberg, T. G. Jones, and A. Ting, "Direct measurements of the nonlinear index of refraction of water at 815 and 407 nm using single-shot supercontinuum spectral interferometry," *Applied Physics Letters*, vol. 94, p. 211102, May 2009.

[92] W. J. Wadsworth, A. Ortigosa-Blanch, J. C. Knight, T. A. Birks, T.-P. M. Man, and P. S. J. Russell, "Supercontinuum generation in photonic crystal fibers and optical fiber tapers: a novel light source," *Journal of the Optical Society of America B*, vol. 19, p. 2148, Sept. 2002.

[93] A. M. Zheltikov, "Let there be white light: supercontinuum generation by ultrashort laser pulses," *Physics-Uspekhi*, vol. 49, no. 6, pp. 605–628, 2006.

[94] H. Li, B. Mignolet, G. Wachter, S. Skruszewicz, S. Zherebtsov, F. Süßmann, A. Kessel, S. Trushin, N. G. Kling, M. Kübel, B. Ahn, D. Kim, I. Ben-Itzhak, C. Cocke, T. Fennel, J. Tiggesbäumker, K.-H. Meiwes-Broer, C. Lemell, J. Burgdörfer, R. Levine, F. Remacle, and M. Kling, "Coherent Electronic Wave Packet Motion in C60 Controlled by the Waveform and Polarization of Few-Cycle Laser Fields," *Phys. Rev. Lett.*, vol. 114, p. 123004, Mar. 2015.

[95] M. Wollenhaupt, A. Assion, D. Liese, C. Sarpe-Tudoran, T. Baumert, S. Zamith, M. Bouchene, B. Girard, A. Flettner, U. Weichmann, *et al.*, "Interferences of ultrashort free electron wave packets," *Physical review letters*, vol. 89, no. 17, p. 173001, 2002.

[96] M. F. Kling, C. Siedschlag, A. J. Verhoef, J. I. Khan, M. Schultze, T. Uphues, Y. Ni, M. Uiberacker, M. Drescher, F. Krausz, and M. J. J. Vrakking, "Control of Electron Localization in Molecular Dissociation," *Science*, vol. 312, pp. 246–248, Apr. 2006.

[97] M. Roth, L. Guyon, J. Roslund, V. Boutou, F. Courvoisier, J.-P. Wolf, and H. Rabitz, "Quantum control of tightly competitive product channels," *Physical review letters*, vol. 102, no. 25, p. 253001, 2009.

[98] F. Hagemann, F. Schwaneberg, C. Stanca-Kaposta, and L. Wöste, "White-Light Optimal Control of Photoinduced Processes," *J. Phys. Chem. C*, vol. 119, pp. 10925–10934, May 2015.

[99] L. Keldysh *et al.*, "Ionization in the field of a strong electromagnetic wave," *Sov. Phys. JETP*, vol. 20, no. 5, pp. 1307–1314, 1965.

[100] S. P. Le Blanc, S. C. Rae, K. Burnett, and R. Sauerbrey, "Spectral blue shifting of a femtosecond laser pulse propagating through a high-pressure gas," *Journal of the Optical Society of America B*, vol. 10, p. 1801, Oct. 1993.

[101] C. Bree, A. Demircan, S. Skupin, L. Berge, and G. Steinmeyer, "Plasma induced pulse breaking in filamentary self-compression," *Laser physics*, vol. 20, no. 5, pp. 1107–1113, 2010.

[102] M. Durand, A. Houard, B. Prade, A. Mysyrowicz, A. Durécu, B. Moreau, D. Fleury, O. Vasseur, H. Borchert, K. Diener, R. Schmitt, F. Théberge, M. Chateauneuf, J.-F. Daigle, and J. Dubois, "Kilometer range filamentation," *Optics Express*, vol. 21, p. 26836, Nov. 2013.

[103] J. Kasparian, M. Rodriguez, G. Méjean, J. Yu, E. Salmon, H. Wille, R. Bourayou, S. Frey, Y.-B. André, A. Mysyrowicz, R. Sauerbrey, J.-P. Wolf, and L. Wöste, "White-Light Filaments for Atmospheric Analysis," *Science*, vol. 301, pp. 61–64, July 2003.

[104] F. Hagemann, O. Gause, L. Wöste, and T. Siebert, "Supercontinuum pulse shaping in the few-cycle regime," *Opt. Express*, vol. 21, pp. 5536–5549, Mar 2013.

[105] D. Wang, Y. Leng, and Z. Xu, "Measurement of nonlinear refractive index coefficient of inert gases with hollow-core fiber," *Appl. Phys. B*, vol. 111, pp. 447–452, Feb. 2013.

[106] C. Bree, A. Demircan, and G. Steinmeyer, "Method for computing the nonlinear refractive index via keldysh theory," *IEEE Journal of Quantum Electronics*, vol. 46, no. 4, pp. 433–437, 2010.

[107] D. P. Shelton and J. E. Rice, "Measurements and calculations of the hyperpolarizabilities of atoms and small molecules in the gas phase," *Chemical Reviews*, vol. 94, no. 1, pp. 3–29, 1994.

[108] V. Loriot, E. Hertz, O. Faucher, and B. Lavorel, "Measurement of high order kerr refractive index of major air components: erratum," *Optics Express*, vol. 18, no. 3, pp. 3011–3012, 2010.

[109] Á. Börzsönyi, Z. Heiner, A. Kovács, M. Kalashnikov, and K. Osvay, "Measurement of pressure dependent nonlinear refractive index of inert gases," *Optics express*, vol. 18, no. 25, pp. 25847–25854, 2010.

[110] M. Mlejnek, E. M. Wright, and J. V. Moloney, "Dynamic spatial replenishment of femtosecond pulses propagating in air," *Optics Letters*, vol. 23, no. 5, pp. 382–384, 1998.

[111] A. Talebpour, S. Petit, and S. Chin, "Re-focusing during the propagation of a focused femtosecond ti: Sapphire laser pulse in air," *Optics Communications*, vol. 171, no. 4, pp. 285–290, 1999.

[112] L. Bergé, S. Skupin, F. Lederer, G. Méjean, J. Yu, J. Kasparian, E. Salmon, J. P. Wolf, M. Rodriguez, L. Wöste, R. Bourayou, and R. Sauerbrey, "Multiple Filamentation of Terawatt Laser Pulses in Air," *Phys. Rev. Lett.*, vol. 92, p. 225002, June 2004.

[113] B. Schmidt, M. Hacker, G. Stobrawa, and T. Feurer, "Lab2-a virtual femtosecond laser lab," *http://www. lab2. de.*, 2001.

[114] F. Théberge, W. Liu, P. T. Simard, A. Becker, and S. L. Chin, "Plasma density inside a femtosecond laser filament in air: Strong dependence on external focusing," *Physical Review E*, vol. 74, no. 3, p. 036406, 2006.

[115] I. Velchev, W. Hogervorst, and W. Ubachs, "Precision VUV spectroscopy of Ar I at 105 nm," *J. Phys. B: At. Mol. Opt. Phys.*, vol. 32, no. 17, p. L511, 1999.

[116] F. Brandi, W. Hogervorst, and W. Ubachs, "High-resolution vacuum-ultraviolet and ultraviolet photoionization spectroscopy of krypton," *Journal of Physics B: Atomic, Molecular and Optical Physics*, vol. 35, no. 4, p. 1071, 2002.

[117] W. Liu, J. Bernhardt, F. Théberge, S. Chin, M. Châteauneuf, and J. Dubois, "Spectroscopic characterization of femtosecond laser filament in argon gas," *Journal of Applied Physics*, vol. 102, no. 3, p. 033111, 2007.

[118] A. S. Sandhu, S. Banerjee, and D. Goswami, "Suppression of supercontinuum generation with circularly polarized light," *Optics communications*, vol. 181, no. 1, pp. 101–107, 2000.

[119] H. Yang, J. Zhang, Q. Zhang, Z. Hao, Y. Li, Z. Zheng, Z. Wang, Q. Dong, X. Lu, Z. Wei, *et al.*, "Polarization-dependent supercontinuum generation from light filaments in air," *Optics letters*, vol. 30, no. 5, pp. 534–536, 2005.

[120] Y. Shi, A. Chen, Y. Jiang, S. Li, and M. Jin, "Influence of laser polarization on plasma fluorescence emission during the femtosecond filamentation in air," *Optics Communications*, vol. 367, pp. 174–180, 2016.

[121] S. Rostami, M. Chini, K. Lim, J. P. Palastro, M. Durand, J.-C. Diels, L. Arissian, M. Baudelet, and M. Richardson, "Dramatic enhancement of supercontinuum generation in elliptically-polarized laser filaments," *Scientific reports*, vol. 6, 2016.

[122] O. Kosareva, N. Panov, V. Makarov, I. Perezhogin, C. Marceau, Y. Chen, S. Yuan, T. Wang, H. Zeng, A. Savel'ev, *et al.*, "Polarization rotation due to femtosecond filamentation in an atomic gas," *Optics letters*, vol. 35, no. 17, pp. 2904–2906, 2010.

[123] W. C. Henneberger, "Perturbation method for atoms in intense light beams," *Physical Review Letters*, vol. 21, no. 12, p. 838, 1968.

Appendix

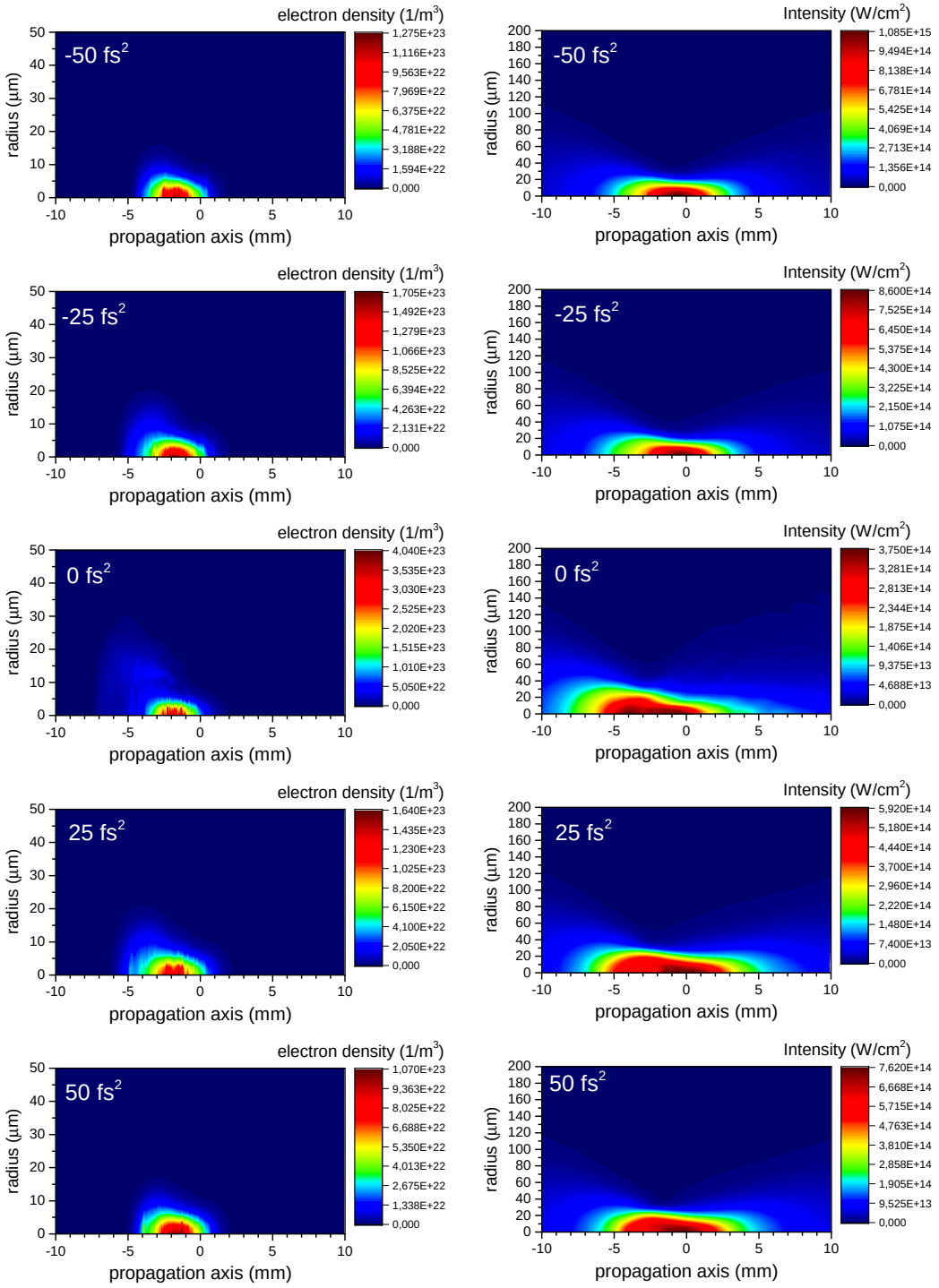

Figure 1: (left column) electron density distribution plotted against the radial and propagation coordinate for linearly chirped pulses in $9\,bar$ *Argon. (right column) Corresponding Intensity in the focal region which is affected by plasma defocussing.*

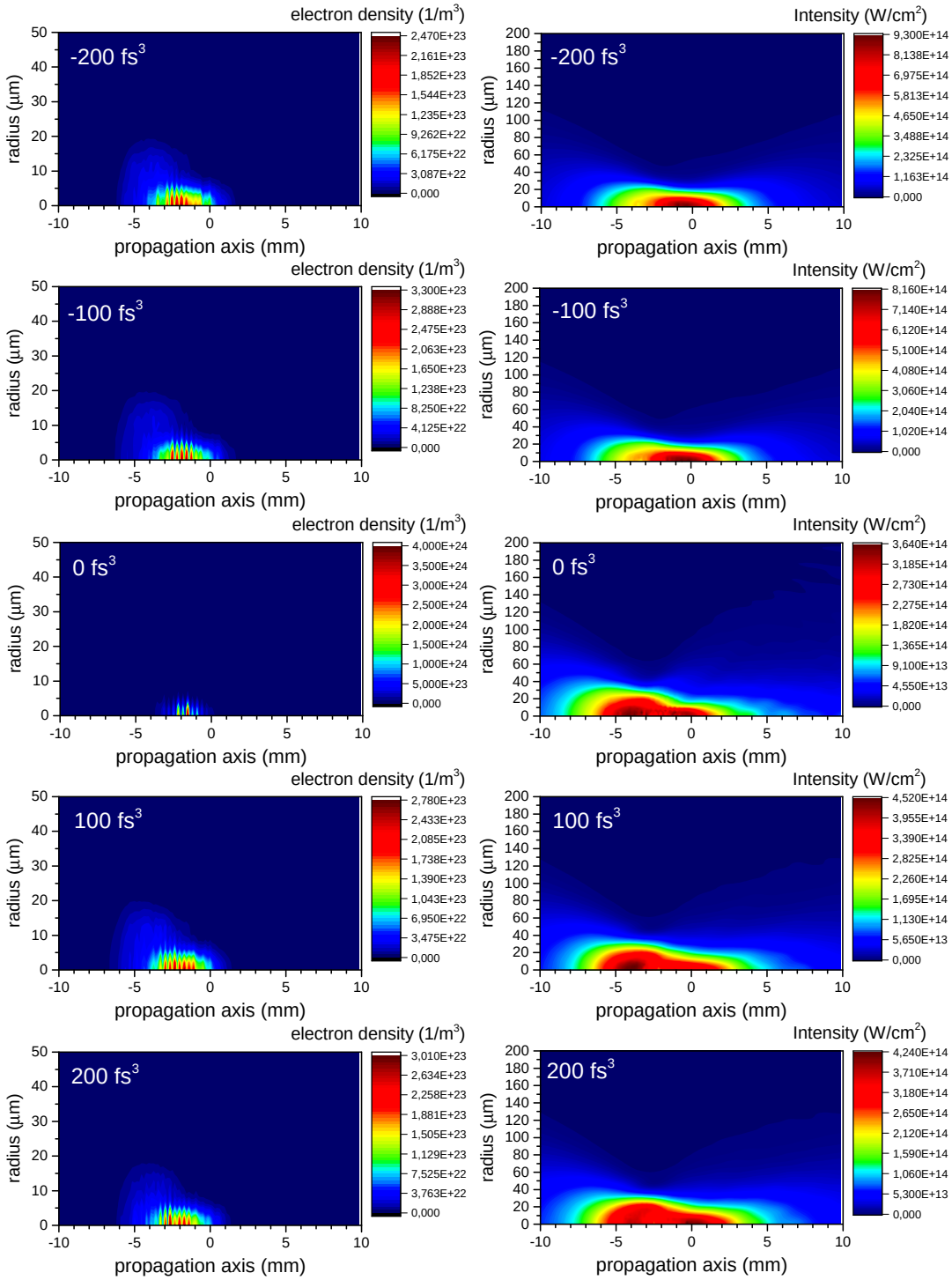

Figure 2: (left column) electron density distribution plotted against the radial and propagation coordinate for quadratically chirped pulses in $9\,bar$ Argon. (right column) Corresponding intensity in the focal region which is affected by plasma defocussing and the asymmetric pulse shape.

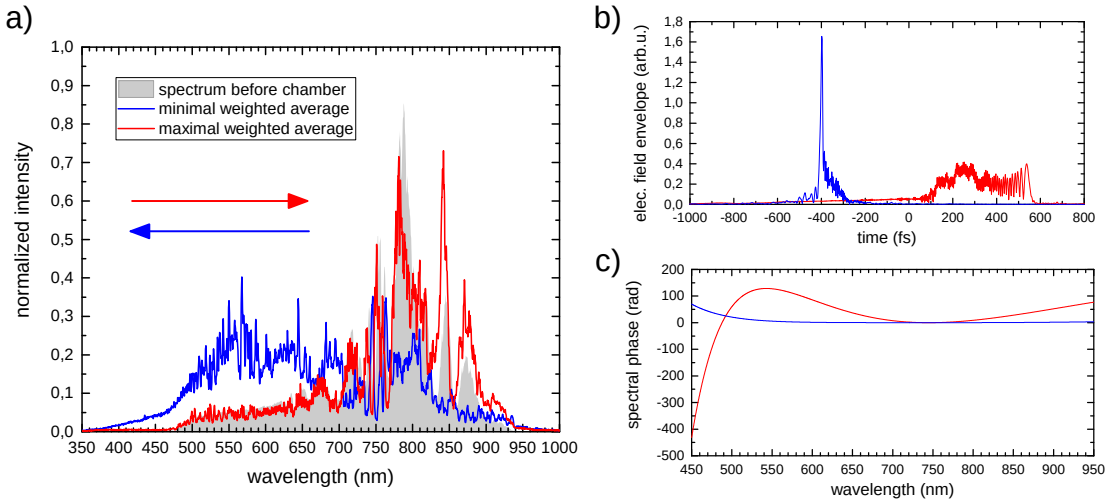

Figure 3: a) The blue and red lines depict the changes to the spectrum after filamentation in Argon for pulses optimized for either a maximal (red) or minimal (blue) average photon energy. b) Pulses found by the genetic optimization algorithm. c) Phases which give rise to the pulse shapes seen in figure b).

central wavelength	λ_c	b_2	b_3	b_4
min	$793.3\,nm$	$17.6\,fs^2$	$-87.1\,fs^3$	$290.8\,fs^4$
max	$961.7\,nm$	$29.0\,fs^2$	$2068\,fs^3$	$-3772\,fs^4$

Table 1: Optimization results corresponding to the data in fig.3

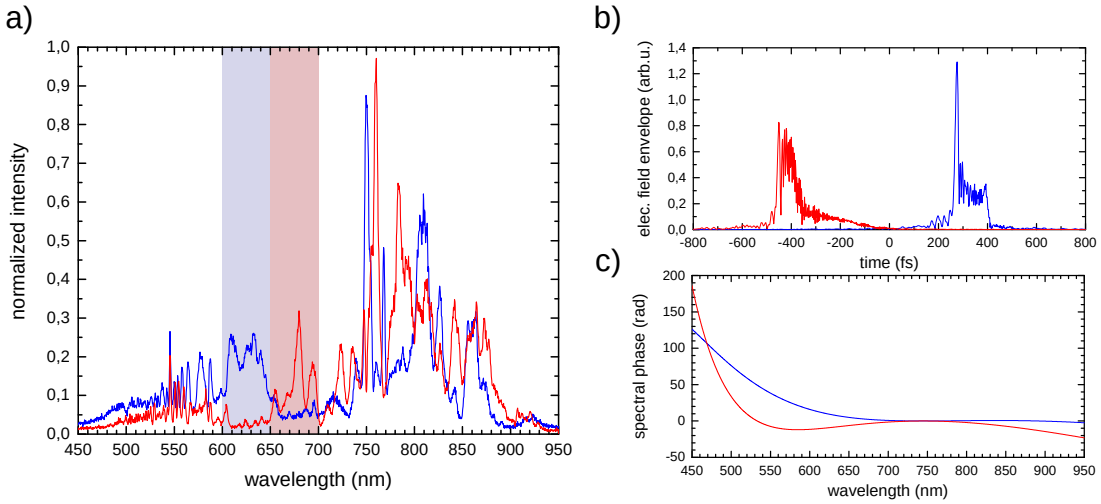

Figure 4: a) The blue line shows the nonlinear distorted spectrum found for pulses which optimize the signal in the sepctral range from ($600\,nm$ to $650\,nm$) while minimizing the intensity in the range from ($650\,nm$ to $700\,nm$) in Krypton. The red line corresponds to the spectrum found when optimizing the inverse ratio. b) Depicts the optimal pulses, while c) shows the phases found by the evolutionary algorithm.

$(600-650)\,nm$	$(650-700)\,nm$	λ_c	b_2	b_3	b_4
min	max	$887.3\,nm$	$-190.5\,fs^2$	$-861\,fs^3$	$-3879\,fs^4$
max	min	$1185.7\,nm$	$-151.4\,fs^2$	$2474\,fs^3$	$-4446\,fs^4$

Table 2: Optimization results corresponding to the data in fig.4

	$(700-725)\,nm$	λ_c	b_2	b_3	b_4
Krypton	min	$1087.0\,nm$	$-555.7\,fs^2$	$400\,fs^3$	$380.4\,fs^4$
Krypton	max	$1131.2\,nm$	$266.1\,fs^2$	$137\,fs^3$	$-315\,fs^4$
Argon	max	$774.1\,nm$	$-81.7\,fs^2$	$-2627\,fs^3$	$4631\,fs^4$
Argon	min	$817.8\,nm$	$-59.0\,fs^2$	$251.9\,fs^3$	$2780\,fs^4$

Table 3: Parameters found for optimizations on a maximal or minimal spectral band in 9 bar Krypton

List of Figures

List of Tables

List of Publications

- A. Patas, G. Achazi, C. Winta, and A. Lindinger, "Influence of nonlinear effects on the three-photon excitation of L-Tryptophan in water using phase-shaped pulses," *Journal of the Optical Society of America B*, vol. 31, p. 2208, Sept. 2014.

- A. Patas, G. Achazi, N. Hermes, M. Pawłowska, and A. Lindinger, "Contrast optimization of two-photon processes after a microstructured hollow-core fiber demonstrated for dye molecules," *Appl. Phys. B*, vol. 112, pp. 579–586, Apr. 2013.

- J. Otto, A. Patas, J. Althoff, and A. Lindinger, "Fluorescence anisotropy excitation by polarization-shaped laser pulses after transmission through a kagome fiber," *Applied Physics B*, vol. 122, no. 8, pp. 1–7, 2016.

- M. B. Hild, A. Dufour, G. Achazi, A. Patas, P. Scheier, and A. Lindinger, "Selection of ionization paths of k 2 on superfluid helium droplets by wave packet interference," *Chemical Physics Letters*, 2016.

- G. Achazi, A. Patas, and A. Lindinger, "Phase sensitive pulse shaping for molecule selective three-photon excitation," *Eur. Phys. J. D*, vol. 68, pp. 1–4, Nov. 2014.

- G. Achazi, N. Hermes, A. Patas, D. Tolksdorf, and A. Lindinger, "Polarization-shaped laser pulses for improved fluorescence anisotropy contrast," *Eur. Phys. J. D*, vol. 67, pp. 1–5, Aug. 2013.

- M. Pawłowska, G. Achazi, N. Rahmat, A. Patas, and A. Lindinger, "Selective excitation with shaped pulses transported through a fiber using reverse propagation," *Phys. Rev. A*, vol. 86, p. 013834, July 2012.

- M. Pawłowska, A. Patas, G. Achazi, and A. Lindinger, "Parametrically shaped femtosecond pulses in the nonlinear regime obtained by reverse propagation in an optical fiber," *Optics Letters*, vol. 37, p. 2709, July 2012.

- M. Pawłowska, A. Patas, G. Achazi, N. Rahmat, F. Weise, and A. Lindinger, "Shaped pulses transported through an optical fiber in the nonlinear regime for selective excitation of two-photon transitions," *Journal of the Optical Society of America B*, vol. 29, p. 833, Apr. 2012.

- G. Achazi, A. Patas, F. Weise, M. Pawłowska, and A. Lindinger, "Reconstruction of polarization-shaped laser pulses after a hollow-core fiber using backreflection," *Appl. Opt.*, vol. 50, pp. 915–923, Feb. 2011.

- M. Pawlowska, A. Patas, G. Achazi, N. Rahmat, and A. Lindinger, "Transporting shaped pulses through an optical fiber in the nonlinear regime for selective excitation of two-photon transitions," in *Lasers and Electro-Optics Europe (CLEO EUROPE/EQEC), 2011 Conference on and 12th European Quantum Electronics Conference*, pp. 1–1, IEEE, 2011.

- A. Lindinger, G. Achazi, M. Pawłowska, and A. Patas, "Verfahren zur mehrphotonenanregung nach einem optischen Übertragungssystem," 2012. DE102011121559, Patent beim Deutschen Patent- und Markenamt.

Danksagung

Ich möchte mich zuallerst bei Prof. Ludger Wöste für die Möglichkeit bedanken in seiner Arbeitsgruppe meine Promotion schreiben zu dürfen. Er hatte zu jedem Zeitpunkt ein offenes Ohr und immer einen Vorschlag parat. Besonders seine genialen, kleinen Experimente waren immer eine wilkommene Abwechslung. Ich danke Albrecht Lindinger für seine Anleitung. Von ihm konnte ich viel über die wissenschaftliche Praxis lernen. In vielen Diskussionen entwickelten sich so neue Ideen die mich in meiner Arbeit und persönlich weiter brachten. Ebenfalls möchte ich mich bei meinen Kollegen bedanken: Monika Pawlowska betreute mich wärend meiner Diplomarbeit und führte mich in die Laborpraxis und besonders die Justage eines Oszillators ein. Mit Georg Achazi habe ich viele Tage und Nächte im Labor verbracht, die besonders durch angeregte Diskussionen oder auch durch untermalende Musik so viel unterhaltsammer waren. Mit Franz Hagemann und Matthieu Lallane habe ich sehr viele lustige Mittage im Gruppenraum verbracht. Außerdem bedanke ich mich bei Frau Odeh, die durch ihre herzliche Art und Geburtstagskarten das Zentrum der Gruppe dargestellt hat. Schließlich möchte ich mich bei meiner Familie und meiner Freundin bedanken die mich, besonders in den letzten Monaten ausgehalten und immer unterstützt haben.

Selbstständigkeitserklärung

Hiermit versichere ich die vorliegende Dissertation eigenständig und ohne unerlaubte Hilfestellung angefertigt zu haben.
Es wurden ausschließlich die angegebenen Quellen und Hilfen in Anspruch genommen.
Ein Promotionsverfahren zu einem früheren Zeitpunkt an einer anderen Hochschule, oder an einem anderen Fachbereich wurde nicht beantragt. Die hier vorgelegte Arbeit wurde auch nicht in einem führeren Verfahren eingereicht.

Berlin, den

Alexander Tobias Arnold Patas